

TECHNISCHE UNIVERSITÄT BERLIN

Laboratory for Flow Instabilities and Dynamics
Institute of Fluid Dynamics and Technical Acoustics
Prof. Dr.-Ing. Kilian Oberleithner

Master's Thesis

Development of a Fluidic Actuator with Independent Frequency and Amplitude Modulation for Control of a Precessing Vortex Core

Amrit Adhikari

Berlin, 10.03.2020

Email:	amrit.adhikari@campus.tu-berlin.de
Matriculation Number:	341912
Course:	Aerospace Engineering
TU Supervisor:	Prof. Dr.-Ing. Kilian Oberleithner MSc. Finn Lückoff
FDX Supervisor:	Dr.-Ing. Katharina Göckeler

Statutory Declaration / Eidesstattliche Erklärung

I hereby declare that I authored this thesis independently, without forbidden help of others and using only the listed sources and materials.

It is affirmed in lieu of oath that this work is completed independently.

Hiermit erkläre ich, dass ich die vorliegende Arbeit selbstständig und eigenhändig sowie ohne unerlaubte fremde Hilfe und ausschließlich unter Verwendung der aufgeführten Quellen und Hilfsmittel angefertigt habe.

Berlin, 10.03.2020 / Berlin, den 10.03.2020

.....
Amrit Adhikari

Acknowledgement

This thesis is dedicated in remembrance of Prof. Dr. Walter Gebhard, without whose direct and indirect support my study in Germany would not have been possible. I wish the same courage, with which he touched many hearts in his lifetime. I thank him and wish him to rest in peace.

I would like to express my sincere gratitude to Finn Lückoff, M.Sc. and Dr.-Ing. Katharina Göckeler as my supervisors for their continuous advice, guidance and encouragement during the writing of this thesis. Without their guidance and persistent help it would not have been possible to complete this thesis. I sincerely thank them for providing necessary insights and materials.

I am incredibly thankful to the principal of the faculty, Prof. Dr.-Ing. Kilian Oberleithner, for providing the opportunity to work on this thesis and allowing me to conduct the experiments in the faculty. I am thankful for his constructive suggestions in the writing of this thesis.

I am also thankful and appreciative of Thorge Schweitzer for brainstorming with me and for his insightful suggestions. Similarly, my sincere thanks to Bastian Blümel for performing flow simulations, Daniel Barkwoski for his assistance in the setup of the pressure measurement, Bhavraj Thethy for helping me with the Schlieren imaging and Sascha Martinke for helping me with the hot-wire measurement setup. A sincere thank you also goes to Christian Franz and Dr. Jens Wintering for helping me with the queries regarding the construction. I am also thankful to the HFI and FDX for providing a pleasant environment to work.

I take this opportunity to express my deepest gratitude to my family members for the unconditional love and support they have provided me throughout my life: to my beloved mother, father, brother Ananta, sister-in-law Sabina and my lovely sister Prajita. I welcome my nephew, Aswin, to the family. His innocent smile provided me immense joy during few stressing times while writing this thesis. I am also incredibly thankful and appreciative to my personal supporter, Franziska Modler, for her love, consolation and motivation.

I am highly indebted to my cousin Dr. Dipak Raj Pahari and the family for their support and love throughout my stay in Germany. I am blessed to have another family in Germany and I am very thankful to the family Pahari for their love and affection towards me. A special thanks also goes to my *Oma*, Rosita Alex, to whom I am always thankful, especially for her unconditional love and for making my initial days in Germany very comfortable.

I would also like to thank my cousins Narayan Pahari, Danda Raj Pahari and Milan Pahari, whose continuous encouragement and support made it possible to pursue my studies and to write this thesis.

My sense of appreciation also goes to my fellow colleagues and friends for their moral support and encouragement: Nishan, Uttam, Ananta, Ritu, Maximillian, Niroj, Sameer and all the people who motivated and supported me to complete my thesis.

Abstract

Swirl-stabilized combustion is widely used in recent years in gas turbines because of its excellent mixing and good flame stability. It makes use of the swirl motion for the fuel-air mixing and the inner recirculation zone as a result of vortex breakdown to keep the flame stable. This eliminates the necessity of a bluff body usually placed in the combustion chamber for the flame stabilization. However, swirl-stabilized combustors are prone to various combustion instabilities, like a helical coherent structure called precessing vortex core (PVC). Recent studies show its influence on the flame stability and dynamics, mixing properties, reduction of NO_x emission as well as interaction with thermoacoustic instabilities. So, an active control of the PVC is vital to take advantage of the PVC by inducing or suppressing it.

A self-excited oscillation with a certain natural frequency when excited periodically by an external actuation with a different frequency, however with enough amplitude, responds by adjusting its oscillation towards that of the excitation. This phenomenon has already been implemented for the control of the PVC in various studies. Using the same core idea, it should be possible to control the PVC by introducing pulsation to the flow at the region of high receptivity with the frequency near to the natural frequency of the PVC. Of the various methods used for generating pulsation, a fluidic actuator is selected in this work because of its robustness to a harsh environment, lack of moving parts, small size as well as the possibility of generating a wide range of frequency and amplitude.

The goal of this work is to design a fluidic actuator, which can generate a pulsating flow with frequencies near to the natural frequency of the PVC. The important characteristics of the actuator should be the possibility of an independent modulation of the frequency and the amplitude. In addition to that, it should produce an external oscillation with a wide range of frequency, with a minimum of $\pm 10\%$ of the PVC frequency, and amplitude with independent modulation. The flow through the actuator should be negligible compared to the main flow of the swirl-stabilized combustor. Furthermore, the actuator should be integrated in a centerbody with limited space.

With the preset goals, a fluidic actuator is designed combining a fluidic oscillator and an amplifier in a master-slave arrangement. It consists of two inlets for the mass flow in the oscillator and the amplifier for independent modulation of the frequency and the amplitude respectively. The flow alternates between the two outlets creating a pulsating effect, that can be subjected to the control of the PVC. Following the 2D design of the fluidic actuator, 2D simulations of the flow are performed and analysed. The simulation results demonstrate the required functionality. Following that, the actuator is integrated in the 3D centerbody and the

working performance is validated by means of velocity measurement using a hot-wire measurement technique. The analysis of the velocity measurement demonstrates a desired switching characteristics, thus generating a required pulsation for the actuation. Moreover, an independent adjustment of the frequency and the amplitude of the oscillation is possible. Furthermore, the frequency can be adjusted just by tuning a small mass flow in the oscillator and the amplitude can be varied mainly through the amplifier mass flow. Based on the acquired data, the operating range of the actuator is marked. To further validate the results of the velocity measurement, visualization of the outlet flow is performed using a Schlieren imaging technique. With very promising results, the actuator is subjected to the actual actuation of the PVC in an isothermal flow of a generic swirl-stabilized combustor. The analysis shows three distinct reactions: lock-in, damping and shifting. The lock-in is characterized by the synchronization of the PVC frequency to that of the actuation. Similarly, the damping is characterized by the synchronization of the frequency, however, the amplitude is significantly reduced. In case of the shifting, the frequency is shifted to or away from the actuation frequency. For an increasing distance of the actuation from the PVC frequency, an increasing amplitude of the actuation is needed for lock-in. A reaction diagram summarising the reaction of the PVC (lock-in, damping or shifting) for different actuation frequencies and amplitudes has demonstrated a distinct V-form enclosing the lock-in region. The designed actuator has demonstrated the possibility of the lock-in up to $\approx \pm 8$ % of the PVC frequency with the stable maximum possible actuation amplitude.

Zusammenfassung

Die drallstabilisierte Verbrennung wird in den letzten Jahren in Gasturbinen wegen ihrer hervorragenden Mischungseigenschaften sowie guten Flammenstabilität im Zusammenhang mit Lean-premixed Verbrennung vielfach eingesetzt. Sie nutzt die innere Rezirkulationszone infolge des Wirbelaufplatzens, um die Flamme zu stabilisieren. Dadurch wird die Notwendigkeit von stumpfen Körpern vermieden, die normalerweise zur Flammenstabilisierung in der Brennkammer platziert werden. Allerdings sind drallstabilisierte Brennkammern für verschiedene Verbrennungsinstabilitäten anfällig, wie z.B. eine helikale, kohärente Struktur, die als präzidierender Wirbelkern (PVC) bezeichnet wird. Neuere Untersuchungen zeigen die Einflüsse der PVC auf die Flammenstabilität und -dynamik, die Mischung, die Reduktion der NO_x Emission sowie die Wechselwirkung mit thermoakustischen Instabilitäten. Daher ist eine aktive Kontrolle des PVC sehr wichtig, um die Vorteile des PVC durch Induktion oder Unterdrückung zu nutzen.

Durch aktive Strömungskontrolle mit einer periodischen Anregung, kann die Eigenfrequenz des PVC hin zur Anregungsfrequenz angepasst werden. Dieses Phänomen wurde bereits in verschiedenen Studien für die Kontrolle des PVC umgesetzt. Mit der gleichen Kernidee sollte es möglich sein, den PVC durch die Einführung von Pulsationen im Bereich hoher Rezeptivität mit einer Frequenz nahe der Eigenfrequenz des PVC zu kontrollieren. Von den verschiedenen Methoden zur Erzeugung der Pulsation wird in dieser Arbeit ein fluidische Aktuator ausgewählt. Die Vorteile eines solchen Aktuators sind: Robustheit gegenüber extremen Umgebungsbedingungen, der fehlenden beweglichen Teilen, seiner geringen Größe sowie der Möglichkeit, einen großen Frequenz- und Amplitudenbereich zu erzeugen.

Das Ziel dieser Arbeit ist einen Aktuator zu entwickeln, der eine globale hydrodynamische Oszillation in einer drallstabilisierten Brennkammer, den PVC, effektiv kontrollieren kann. Die wichtigen Eigenschaften des Aktuators soll die Möglichkeit einer unabhängigen Modulation von Frequenz und Amplitude sein. Darüber hinaus soll der Aktuator eine externe Oszillation mit einem breiteren Frequenzbereich von mindestens $\pm 10\%$ der PVC-Frequenz erzeugen und einer breiteren Amplitudenspektrum unabhängig von der PVC-Frequenz erzeugen. Der Durchfluss durch den Aktuator sollte gegenüber dem Hauptstrom der drallstabilisierten Brennkammer vernachlässigbar sein. Außerdem sollte der Aktuator mit begrenzten Abmessungen in den Zentralkörper integriert werden.

Mit den vorgegebenen Zielen wird ein fluidischer Aktuator entworfen, der einen fluidischen Oszillator und Verstärker in einer Master-Slave-Anordnung kombiniert. Er besteht aus zwei Eingängen für den Massenstrom im Oszillator und einem Verstärker zur unabhängigen Modulation von Frequenz und Amplitude. Der Durchfluss

wechselt zwischen den beiden Ausgängen und erzeugt einen pulsierenden Effekt, der für die Kontrolle des PVC genutzt werden kann. Nach der 2D-Konstruktion des Aktuators werden 2D-Simulationen durchgeführt und analysiert. Anschließend wurde der Aktuator in den 3D-Zentralkörper integriert und die Funktionalität mittels Geschwindigkeitsmessung mit Hilfe von Hitzdrahtmesstechnik validiert. Die Analyse der Geschwindigkeitsmessung ergab ein gutes Schaltverhalten und damit die gewünschte Oszillation für die Aktuation. Eine unabhängige Einstellung der Frequenz und Amplitude der Oszillation war möglich. Darüber hinaus konnte die Frequenz allein durch Zuleitung eines kleinen Massenstrom im Oszillator und die Amplitude hauptsächlich durch den Massenstrom des Verstärkers variiert werden. Aufbauend auf den gemessenen Daten wird der Arbeitsbereich des Aktuators markiert. Zur weiteren Validierung der Ergebnisse der Geschwindigkeitsmessung wird die Strömungsvisualisierung der Auslaufströmung mit Hilfe der Schlierentechnik durchgeführt.

Mit viel versprechenden Ergebnissen wird der Aktuator in einer generischen drallstabilisierten Brennkammer für die Aktuation von PVC eingesetzt. Die Analyse zeigte drei unterschiedliche Reaktionen: Lock-in, Dämpfung und Frequenz-Verschiebung. Lock-in ist dadurch gekennzeichnet, dass die Frequenz des PVCs mit der Frequenz der Anregung synchronisiert wird, wobei die Amplitude nach der Anregung noch annähernd konstant zur Amplitude des PVCs vor der Anregung bleibt. Ebenso ist die Dämpfung durch die Synchronisation der Frequenz gekennzeichnet, die Amplitude wird jedoch deutlich reduziert. Im Falle einer Frequenz-Verschiebung wird die Frequenz zu oder von der Aktuationsfrequenz verschoben. Ein Diagramm, das die Reaktion von PVCs (Lock-in, Dämpfung oder Frequenz-Verschiebung) für verschiedene Aktuationsfrequenzen und -amplituden zusammenfasst, zeigt eine deutliche V-Form, die den Lock-in-Bereich einschließt. Der entworfene Aktuator ist in der Lage Lock-in bis zu $\approx \pm 8\%$ der PVC-Frequenz zu erreichen.

Contents

List of Figures	III
List of Tables	V
Nomenclature	VII
1 Introduction	1
2 Theoretical Background	3
2.1 Swirl Flows	3
2.2 Vortex Breakdown	4
2.3 Precessing Vortex Core	5
2.4 Actuation of PVC	6
2.5 Fluidics	7
2.5.1 Feedback Type Fluidic Oscillator	7
2.5.2 Fluidic Amplifier	8
2.6 Master-Slave Concept	13
3 Mathematical Background	15
3.1 Root-Mean Square Value	15
3.2 Fourier Transformation	15
3.3 Spatial Fourier Mode Decomposition	16
3.4 Power Spectral Density	16
4 Fluidic Actuator Design	17
4.1 Design of the Oscillator	17
4.2 Design of the Amplifier	19
4.3 Design of the Fluidic Actuator	20
4.4 Flow Simulation	21
4.5 Variation of Fluidic Actuator Designs	25
4.6 Design of the Centerbody	28
4.7 Manufacturing of the Actuator	29
5 Experiment	33
5.1 Hot Wire Measurement	33
5.1.1 Calibration	33
5.1.2 Measurement	36
5.1.3 Results	39

5.2	Comparison to the Simulation Results	44
5.3	Visualization of the Flow	46
5.4	Differential Pressure Measurement	47
5.4.1	Experimental Setup	47
5.4.2	Measurement	50
5.4.3	Results	53
6	Summary	61
7	Conclusion	65
	Bibliography	67

List of Figures

2.1	Visualization of a phase averaged velocity field incorporating a PVC	5
2.2	Geometry of a feedback type fluidic oscillator	8
2.3	Wall interaction bistable amplifier	9
2.4	Wall attachment	10
2.5	Velocity field in an amplifier	11
2.6	Extreme designs of the fluidic amplifier	12
2.7	Master-slave concept	14
4.1	Design process of the fluidic actuator	18
4.2	Construction diagram of the fluidic actuator	20
4.3	Nomenclature scheme used for different designs of the actuator	21
4.4	Oscillation cycle of the actuator	22
4.5	Velocity component at the outlet of the fluidic actuator	23
4.6	Linearity of the frequency	24
4.7	Comparison of the velocity for different mass flow	25
4.8	Different versions of the fluidic actuator	26
4.9	Comparison of the flow in the different fluidic actuator designs	28
4.10	Design of the centerbody	30
4.11	Computer tomography of the centerbody	31
4.12	Internal geometry of the centerbody	32
5.1	Calibration setup	34
5.2	Calibration curve	36
5.3	Hot wire measurement setup	37
5.4	Stability of the measured signal	41
5.5	Dependency of the frequency on the variation of the oscillator flow	42
5.6	Constant frequency for varying total mass flow	43
5.7	Variation of the frequency for a constant total mass flow	44
5.8	Operational range of the used fluidic actuator	45
5.9	Schlieren imaging setup	47
5.10	Schlieren images	48
5.11	Setup for the pressure measurement	49
5.12	Frequency range of the PVC	51
5.13	Time signals and spectra of the signals	53
5.14	Spectra with and without averaging	55
5.15	Different reactions of the PVC to the actuation	56
5.16	Phase angle	57

5.17 Synchronization diagram	58
5.18 Summary of the reaction of the PVC at 136.78 <i>Hz</i>	59
5.19 Summary of the reaction of the PVC at 119.23 Hz	59

List of Tables

4.1	Variation of the oscillator and the amplifier flow	24
5.1	Operational range of the actuator	41
5.2	Relative difference in peak velocity	45
5.3	Comparison of the hot-wire measurement to the simulation	46

Nomenclature

Latin Symbols

Symbol	Unit	Description
\dot{D}	[Nm]	Axial flux of azimuthal momentum
$\partial p / \partial r$	[N/m ³]	Pressure gradient in radial direction
$\partial p / \partial x$	[N/m ³]	Pressure gradient in axial direction
E_{RMS}	[-]	Root-mean square value
f	[Hz]	Frequency
f_c	[N]	Centrifugal force
\dot{I}	[Nm]	Axial flux of axial momentum
m	[-]	Azimuthal mode
N	[-]	Length of a vector
p_k	[Pa]	Pressure signal of the k^{th} sensor
\hat{p}_m	[-]	Fourier coefficient
P_{xx}	[-]	Periodogramm
PSD	[-]	Power spectral density
r	[m]	Radius
R	[m]	Characteristic radius
t	[s]	Time
T	[s]	Length of time interval
U_θ	[m/s]	Azimuthal velocity
v	[m/s]	Velocity
x_1, x_2, x_N	[-]	Discrete samples
x, y, z	[m]	Cartesian coordinates
X	[-]	Discrete Fourier Transformation of x
X_r	[-]	Coefficient of Fourier transformation
\hat{X}	[-]	Fourier coefficient of X
\tilde{X}_T	[-]	Fourier transformation of $x(t)$

Greek Symbols

Symbol	Unit	Description
α	[-]	Overheating factor
ω	[1/s]	Angular frequency
ρ	[kg/m ³]	Density

Key Figures

Symbol	Definition	Description
c_μ	$2 \cdot \frac{H}{t} \cdot \left(\frac{v'}{u_\infty}\right)^2$	Impuls coefficient
S	[-]	Swirl number

Index

Index	Description
m	Mode number
PVC	Condition for activated main mass flow
PVC&A	Condition for activated main mass flow and actuator mass flow

Abbreviations

Abbreviations	Description
A/D	Analog/Digital
CAD	Computer-Aided Design
COM	Component Object Model
CT	Computer Tomography
CTA	Constant Temperature Anemometry
CTRZ	Central Toroidal Recirculation Zone
DNS	Direct Numerical Simulation
FDX	Fluid Dynamix GmbH
FFT	Fast Fourier Transformation
HDL	Harry Diamond Laboratories
HFI	Herman-Föttinger-Institut
LED	Light Emitting Diode
LES	Large Eddy Simulation
NO_x	Oxides of Nitrogen
OsciAmp	Oscillator and Amplifier combination
RANS	Raynolds-averaged Navier-Stokes
RMS	Root Mean Square
PSD	Power Spectral Density
PIV	Particle Image Velocimetry
PVC	Precessing Vortex Core
TU	Technische Universität
US	United States
V1, V2, V3, V4	Name given to different versions of OsciAmp
Z2	Name given to the oscillator model from the preceeding study
2D	2-Dimensional
3D	3-Dimensional

1 Introduction

Swirl-stabilized combustion is widely used in recent years in gas turbines, internal combustion engines, power station burners, process and refinery burners because of excellent mixing and good flame stability [1]. This is a result of the formation of a central re-circulation zone due to vortex breakdown [2]. In addition to that, the direct contact to the combustor surface by the high-temperature flame is disrupted by the shear flow leaving the burner. This increases the life expectancy of the equipment. Moreover, when operated under lean conditions, swirl-stabilized combustors have high potential for low emissions. Despite those positive advantages, swirl-stabilized combustors are prone to various combustion instabilities [2].

Combustion instabilities are very complicated phenomenon, which are intensely researched and significant amount of literature is published. Yet, the mechanism resulting in the instability of gas turbines is not completely understood. It is characterized by oscillations of one or more natural acoustic modes of the combustor exhibiting a large amplitude. The unsteady heat release from the combustion coupling with the natural acoustic modes of the combustor results in a self-excited oscillation, which can attain very high energetic levels. Since, flames are very sensitive even to small perturbations, the combustion chamber is prone to pressure fluctuations. These combustion driven pressure fluctuations can lead to structural damage and failure. Many of the first rocket launches including Ariane 1 experienced such combustion oscillations resulting in complete destruction [3].

This work however only focuses on the isothermal flow of a swirl-stabilized combustor and instability associated to it. In this flow, a strong helical coherent structure known as Precessing Vortex Core (PVC) occurs. It is a self excited oscillation generally found in swirling flows. It is always found at non-reacting conditions and at reacting conditions after the transition from V-shaped to detached M-shaped flames in a swirl-stabilized combustor [4]. Various studies [5–8] used linear hydrodynamic stability theory to determine the origin and nature of this instability. Few studies on its impact on the flame stability and dynamics [4], fuel and air mixing properties [9] and interaction with the thermoacoustic instabilities [10–12] are performed. Yet, its influence on the combustion performance is not fully covered. Moreover, the possibility of the PVC for the reduction of NO_x emission and other combustion instabilities motivates for further studies.

An active control system, which can induce or suppress the PVC, is essential to study the combustion mechanism and interactions with and without the PVC. It has been found that a self-excited hydrodynamic oscillator with a certain natural frequency, when excited periodically by an external excitement with a different frequency, however with enough amplitude, responds by adjusting its oscillation towards that

1 Introduction

of the excitation [13, 14]. This synchronized condition is known as lock-in and was first discovered by Huygens in 1673 in a pendulum clock [13]. However, for phase lock-in, the hydrodynamic system synchronizes not only the frequency but also the phase. Various works [15–22] studied the phenomenon of lock-in in numerous forced self-excited flows. Based on this phenomenon, Lückoff *et al.* [23, 24] designed various actuators and successfully implemented an open and closed loop control of the PVC. For the actuation, oscillating air exiting through four outlets placed in the centerbody in the mixing tube at the region of high receptivity of the PVC is used. The oscillating air is generated by four circumferentially arranged loudspeakers. Although, this form of actuation using loudspeakers for the generation of the oscillation serves its purpose in the laboratory for studies, the actual implementation into the combustion chamber at harsh environment is highly demanding.

For the industrial acceptance, Barkwoski [25] used a different approach of actuation using fluidic actuator. The fluidic actuator designed by FDX Fluid Dynamix GmbH can generate oscillations without moving parts and can be integrated into the centerbody of the swirl-stabilized combustion chamber. This makes the actuation concept robust and saves weight as well as space. The fluidic oscillator used as an actuator in the study demonstrated the proof-of-concept. However, the frequency of the oscillator is proportional to the supplied mass flow through it. At the same time, the amplitude of the actuation is also proportional to the mass flow through the oscillator. This means, for smaller frequency the amplitude of the actuation is also smaller and for higher frequency the amplitude is also higher. This limits the scope of actuation.

This work is therefore focused on the development of a new type of fluidic actuator with independent modulation of the frequency and amplitude. The actuator is designed based on a master-slave concept such that, a fluidic oscillator provides frequency information at the control ports of a fluidic amplifier, which is supplied with additional mass flow. With this arrangement, the combination of mass flow in the oscillator and amplifier should be able to independently control the frequency and amplitude of the actuation. This study intends to deliver the proof-of-concept of the used fluidic actuator for the control of the PVC in an isothermal flow of a swirl-stabilized combustion chamber.

For the mentioned purpose, a wide literature research on the fluidics and concept of master-slave arrangement is performed. From the collected information, an actuator, integrated in the centerbody of the swirl-stabilized combustion chamber, is designed and constructed in a commercial software *SolidWorks* for 3D printing. Before physical construction, 2D flow simulations were performed for functionality tests. The 2D models are further optimised and finally integrated in a 3D centerbody. The 3D printed centerbody model is validated using hot-wire velocity measurements and the visualization of the flow out of the centerbody using Schlieren technique. Finally, a differential pressure measuring technique is implemented for the possibility to control the PVC in a generic isothermal flow of a swirl-stabilized combustion chamber. The measured data is then assessed, analysed and presented in this work.

2 Theoretical Background

This section introduces the theory behind the present study. It provides an overview of the topic beginning with introduction to swirl flows and the process of vortex breakdown. Then, the actual problem of this work is encountered: the precessing vortex core (PVC). After familiarization of this hydrodynamic instability, a thorough study of the control mechanism is presented. It involves the applied fluidics and the concept of master-slave.

2.1 Swirl Flows

A Swirl flow is characterised by a spiraling motion resulting from the azimuthal velocity component of the flow. It can be achieved by the use of swirl generators, swirl vanes or by direct tangential entry into the chamber. Various practical applications of swirl flows include Ranque-Hilsch tubes, vortex amplifiers and reactors, agricultural spraying equipments, heat exchangers, jet pumps, different kinds of engines, turbines and boilers etc. Modern combustion chambers use swirl flows to enhance the combustion process. The degree of swirl imparted on the flow has an impact on the jet growth and entrainment in general. Moreover, in reacting flows, it influences the flame size, shape, dynamics, stability and combustion performance. The degree of swirl in the flow is characterised by a non-dimensional swirl number (S) represented by the ratio of axial flux of azimuthal momentum (\dot{D}) and a product of axial flux of axial momentum (\dot{I}) and a characteristic radius (R). [1, 26]

$$S = \frac{\dot{D}}{R \dot{I}} \quad (2.1)$$

As the degree of swirl increases, the jet growth, entrainment and decay are enhanced gradually. At low swirl numbers ($S < \approx 0.4$), there is only a slight axial pressure gradients because of swirl motion, which is not enough to cause axial recirculation. However, at high swirl numbers ($S > \approx 0.6$), where strong radial and axial pressure gradients occur resulting in a vortex breakdown induced central toroidal recirculation zone (CTRZ) [1]. Further increase in swirl number moves the recirculation zone towards the centerbody and converses with the wake recirculation zone [27]. The CTRZ recirculates the hot products and acts as a heat reservoir, thereby stabilizing the flame. Moreover, the flame length is reduced as low as one-fifth that of zero swirl as a result of enhanced mixing [28]. However, the study conducted by Tangirala et al. [28] on the effect of swirl and heat release on the flow structures and flame properties in a non-premixed swirl burner showed improved mixing and flame stability

up to a swirl number of approximately 1. Reduced turbulence level and flame stability are observed for further increase in the swirl number.

2.2 Vortex Breakdown

A Vortex breakdown is a phenomenon usually found in swirling jets, where the ratio of the azimuthal to the axial momentum exceeds a certain threshold resulting in an abrupt widening of the vortex core into a new stable coherent structure [29]. Although extensive study has been performed on this phenomenon, no universal definition is found. Many researchers explain the term as an existence of rapid deceleration of axial flow, resulting in a stagnation point and further to a reversed axial flow [26].

Several types of vortex breakdown have been pointed out in different literature. They have been observed on delta wings at high incidence angles and in axis-symmetric swirling flows in tubes. The first identification of vortex breakdown was done by Peckham and Atkinson (1957) [30] in vortices generated over the leading-edge swept wings and the first to describe the axis-symmetric and spiral type of vortex bursts were Lambourne and Bryer (1962) [31]. Later on Sarpkaya (1971) [32] identified three different types of vortex breakdown: single helical, double helical and axial-symmetric in a diverging cylindrical tube. Faler and Leibovich (1978) [33] described six different types of vortex breakdown from the flow visualization studies and laser Doppler anemometer measurements. They have excluded the double helical vortex breakdown, as proposed by Sarpkaya, because of the absence of stagnation of axial flow. Similarly, at low Reynolds number Billant et al. (1988) [29] also measured four different types of vortex breakdown with a new conical-shaped vortex breakdown.

Axial-symmetric and spiral vortex breakdown are predominantly found in swirling flows in combustion chambers. Gupta et al. (1984) [1], Tangirala et al. (1987) [28] and Huang et al. (2009) [26] associate vortex breakdown to the formation of CTRZ. The formation of CTRZ is explained based on the conservation of momentum in the radial direction for laminar inviscid flow as:

$$\frac{\partial p}{\partial r} \sim f_c \sim \frac{\rho U_\theta^2}{r}, \quad (2.2)$$

where, $\partial p/\partial r$ is the pressure gradient in radial direction, f_c represents centrifugal force, ρ the density, U_θ the azimuthal velocity and r the radius. The centrifugal force generated from the azimuthal flow produces a radial pressure gradient with lowest pressure on the centerline. With the expansion of flow and decay of azimuthal velocity for increasing axial distance, the pressure is recovered. This results in an increase of pressure on the centerline, creating a positive pressure gradient $\partial p/\partial x$. This forces the centerline flow against the main flow direction. With enough swirl strength, recirculation zone is formed with axis symmetric stagnation points. Accompanied by this axial movement, vortex breakdown starts immediately.

2.3 Precessing Vortex Core

As described in the previous sections, swirl-stabilized modern gas turbine combustors use vortex breakdown and the formation of the central toroidal recirculation zone (CTRZ) for flame stabilization and enhanced burning of the unburned reactants. The CTRZ is usually, however not always, accompanied by the occurrence of coherent flow structures like the precessing vortex core (PVC) [4]. The PVC is a three-dimensional unsteady asymmetric global hydrodynamic instability usually found in inner shear layer. It is characterized by a periodical off-axis precessing motion of a central vortex core at a certain frequency [2, 26]. The PVC is usually manifested in isothermal swirling jets. In reacting flows, however, the existence of PVC is dependent on the density stratification and hence on the flame shape [4, 34, 35].

Figure 2.1 shows the 3D visualization of phase-averaged velocity field at Reynolds

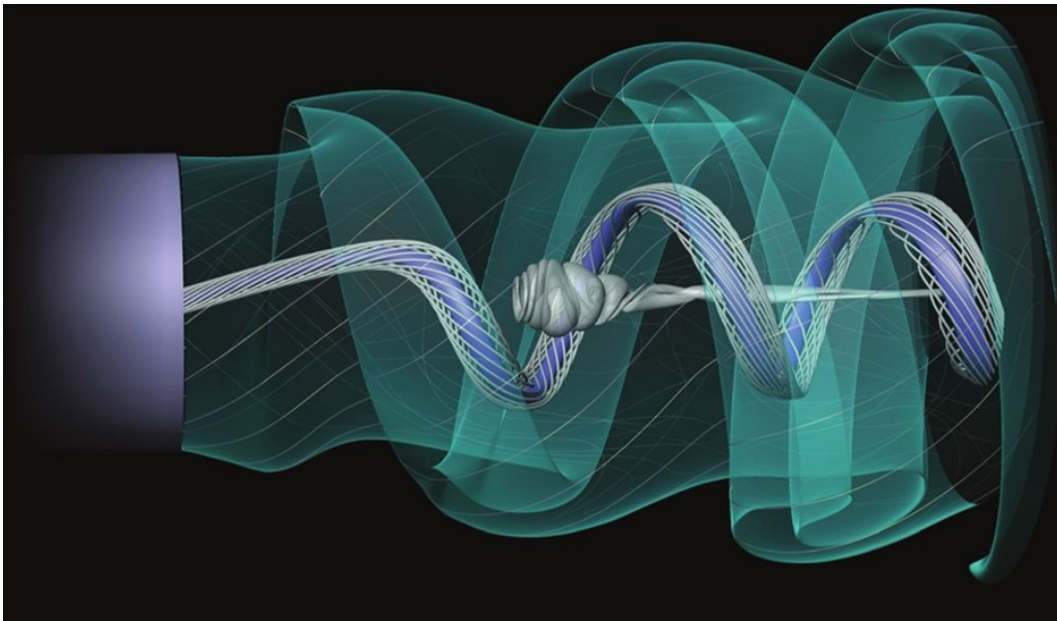


Figure 2.1: Visualization of a phase averaged velocity field incorporating a PVC. The central streak-lines and bluish streak-surface originating from the nozzle center represent the PVC. The semi-transparent gray pathline-surface at the center features the internal recirculation zone. The semi-transparent greenish streak-surface represents the spiral vortices induced by helical waves [36].

number of $Re = 20,000$ incorporating a PVC [36]. It is reconstructed from uncorrelated 2D particle image velocimetry (PIV) snapshots. The diagram shows three flow features. The central streak-lines and bluish streak-surface originating from the nozzle center represent the PVC. The semi-transparent gray pathline-surface at the center features the central recirculation zone. The semi-transparent greenish

2 Theoretical Background

streak-surface represents the spiral vortices induced by the helical waves. Various studies show advantageous aspects of the PVC in turbulent swirl flames in gas turbines. DNS [37] and LES [38] calculations have shown increased fuel-air mixing as a result of the PVC for non-reacting conditions. At reacting conditions, the PVC enhances not only the mixing of fuel and air but also in the mixing of burned and unburned gases [9]. However, the PVC can also induce local disruption, quenching or even extinction of the flame [39]. Furthermore, literature [10, 40] suggest the interaction of the PVC with thermoacoustic oscillations of the flame. Yet, its influence on the combustion performance still needs a wide range of study. Moreover, the possibility of the PVC for the reduction of NO_x emission and combustion instabilities motivates for further studies.

2.4 Actuation of PVC

An active control, which can induce or suppress the PVC, is vital to study the combustion mechanisms and interactions with and without the PVC. The PVC can be seen as a self-excited oscillator. It has been found that a self-excited hydrodynamic oscillator with a certain natural frequency, when excited periodically by an external actuation with a different frequency, however with enough amplitude, responds by adjusting its oscillation towards that of the actuation [13, 14]. At a certain critical amplitude value of actuation the oscillator oscillates stably in phase with the actuation frequency. This synchronized condition is known as lock-in and was first discovered by Huygens in 1673 in a pendulum clock [13]. Various works [15–22] studied the phenomenon of lock-in in numerous forced self-excited flows. Based on this phenomenon, Lückoff et.al. [23, 24] designed various actuators and successfully implemented an open and closed loop control of the PVC. For the actuation, oscillating air exiting through four outlets placed in the centerbody of the swirl-tube at the region of high receptivity of the PVC is used. The oscillating air is generated by four circumferentially arranged loudspeakers. Although, this form of actuation using loudspeakers for the generation of oscillation serves its purpose in the laboratory, the actual implementation in the combustion chamber at a harsh environment is very demanding.

For the industrial acceptance, Barkwoski [25] used a different approach of actuation using a fluidic actuator. The fluidic actuator can generate oscillation without moving parts and can be integrated into the centerbody of the swirl-stabilized combustion chamber. This makes the actuation concept robust and saves weight as well as space. The fluidic oscillator used as an actuator in the study demonstrated the proof-of-concept. However, the frequency of the oscillator is proportional to the supplied mass flow through it. At the same time, the amplitude of the actuation is also proportional to the mass flow through the oscillator. This means, for smaller frequency the amplitude of the actuation is also smaller and for higher frequency the amplitude is also higher. This limits the scope of the actuation, so this study focuses on the development of a new design of fluidic oscillator with an independent

adjustment of the frequency and the amplitude.

2.5 Fluidics

The fluidic technology is based on the use of interacting streams of pressurized fluid for various control, sensory as well as computing functions. Because of no mechanical moving parts, fluidic components are extremely reliable, robust to severe environments, cost efficient and have a long durability. Moreover, the geometrical structure of a fluidic object is simple and yet allows to vary various parameters. Although, the speed of operation is not as fast as electronics, it is considerably faster than conventional pneumatic/hydraulic systems. They are also usually small in size and light. Since the discovery of fluidics in 1959 by a group of scientists at the U.S. Army Harry Diamond Laboratories (HDL), application of fluidics has been realised in aerospace and automation industries as well as medicine and personal use items [41]. Feedback and vortex interaction [42] as well as jet interaction [43] type of fluidic devices have been patented. In essence, a fluidic oscillator consists of two parts: an amplifier that uses the Coanda effect and at least one feedback channel [44]. In the present work, two types of fluidic components: fluidic oscillator with feedback and bistable fluidic amplifier are used in a master and slave arrangement. They are discussed in the following sections.

2.5.1 Feedback Type Fluidic Oscillator

Fluidic oscillators are a group of fluidic components that can produce an oscillating or pulsating beam of fluid by making use of special geometries and fluid mechanical effects. A feedback type fluidic oscillator has a fluidic circuit consisting of a power jet input nozzle, two feedback loops and an exit aperture. This forms two island like structures within the cavity. A general geometry of a feedback type fluidic oscillator is shown in Figure 2.2. A power jet enters the cavity of the circuit through the input nozzle. At first, the jet expands to fill the throat and the feedback channels. Then on the cavity enclosed by the two island like structures, on either side of the jet, two counter rotating vortices are formed. With the increase in the intensity of the jet, one vortex becomes dominant, which causes the power jet to deflect against the opposite wall. The rear end of the island like structure directs the jet towards the opposite side of the exit aperture. However, because of the Coanda effect, at the downstream end of the island like structure, a small part of the jet attaches on the wall causing some of the fluid to enter the feedback channel. The fluid in the feedback channel carries pressure waves back to the control port, which forces the power jet to detach from the wall of the island structure and switch to the opposite wall. This process repeats resulting in an oscillatory fluid motion at the exit. [45]

In the present study, a fluidic oscillator is used for the generation of frequency for the actuation of the PVC. Without any moving parts, it controls the frequency of the controlling flow by generating a pulsating flow. Because of no moving parts, the fluidic oscillator are very robust and can be used in extreme conditions. Apart

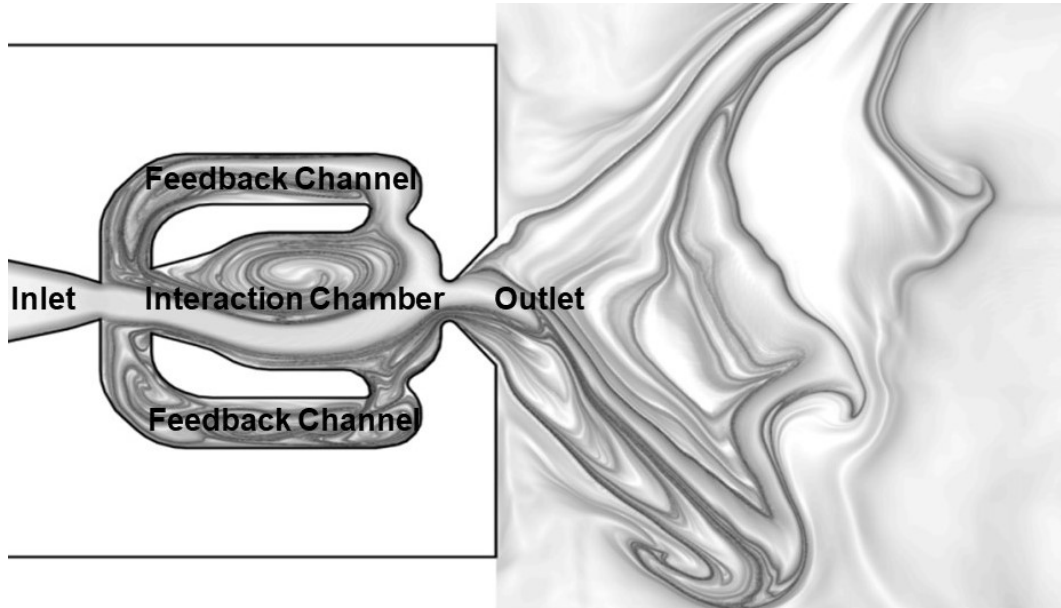


Figure 2.2: Geometry of a feedback type fluidic oscillator. It incorporates inlet, central interaction chamber, two feedback channels and an outlet [46].

from that, the oscillator can be constructed relatively small, have a wide range of frequency and can be integrated into the centerbody of the used experimental model.

2.5.2 Fluidic Amplifier

In the present work, a wall interaction bistable amplifier is used. Similar to most of the fluidic amplifiers, it includes at least four basic functional parts: a supply port, one or more control ports, one or more output ports and an interaction region [41]. A basic wall interaction bistable amplifier design is shown in figure 2.3. It illustrates different components of the bistable amplifier with significant widths and angles. The main flow (power jet) enters the interaction region through the power nozzle. Similarly, the two control ports supply the control flow to the power jet. Both the supply and the control ports open to the interaction zone, which is constrained by two adjacent side walls. The side walls are inclined at a certain angle (wall angle) and separated at the base with a certain setback distance. Further downstream, a splitter splits the channel into two outlets, with a certain angle (splitter angle), which is not always equal to the wall angle. The outlet channels have receiving ends (receiver) towards the interaction zone at a certain distance from the power nozzle (splitter distance).

Figure 2.4 demonstrates the flow mechanism in the wall interaction bistable amplifiers at the initial state of the entry of the power jet in the interaction zone up to the wall attachment. The power jet is submerged in the interaction zone, where

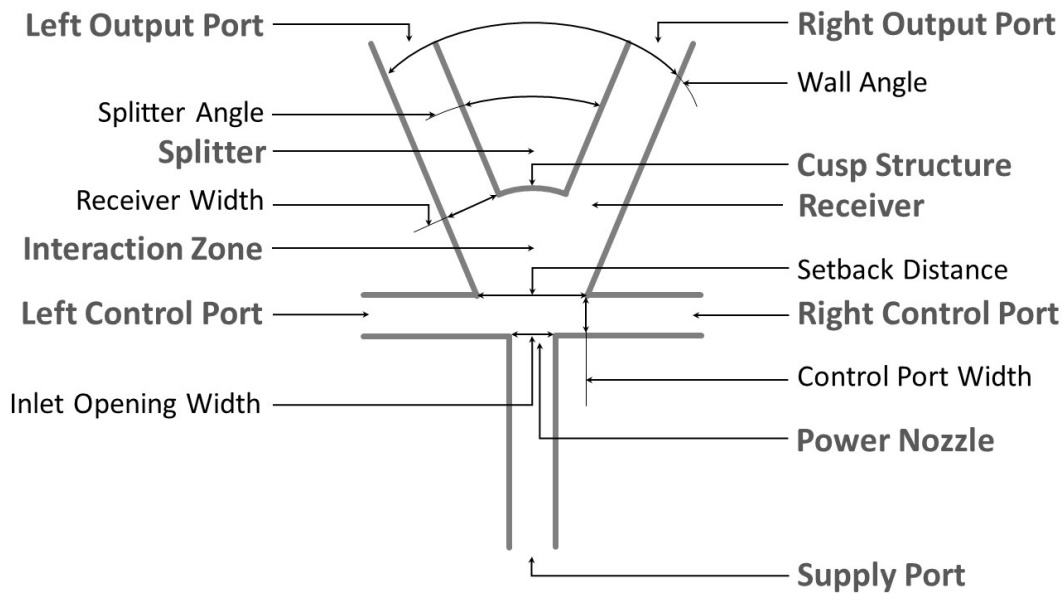
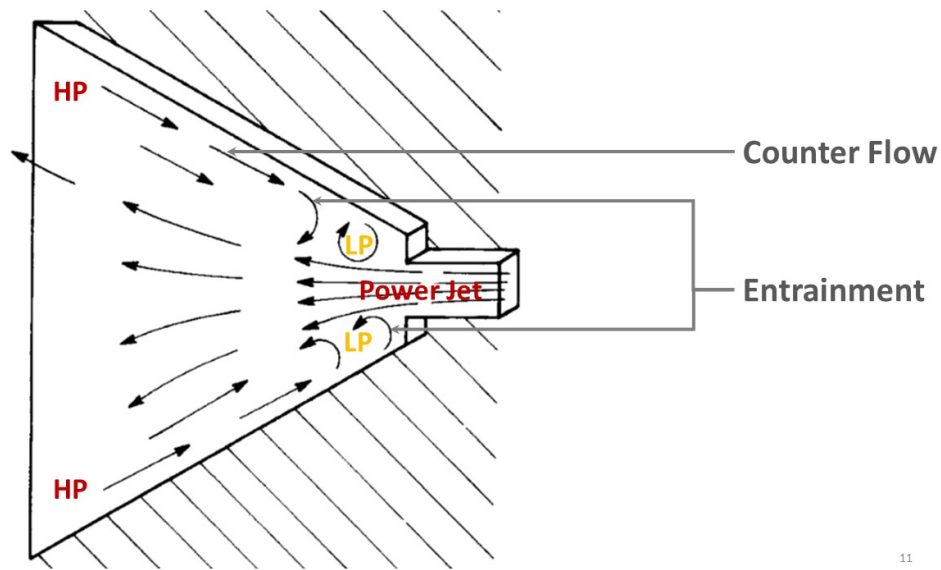


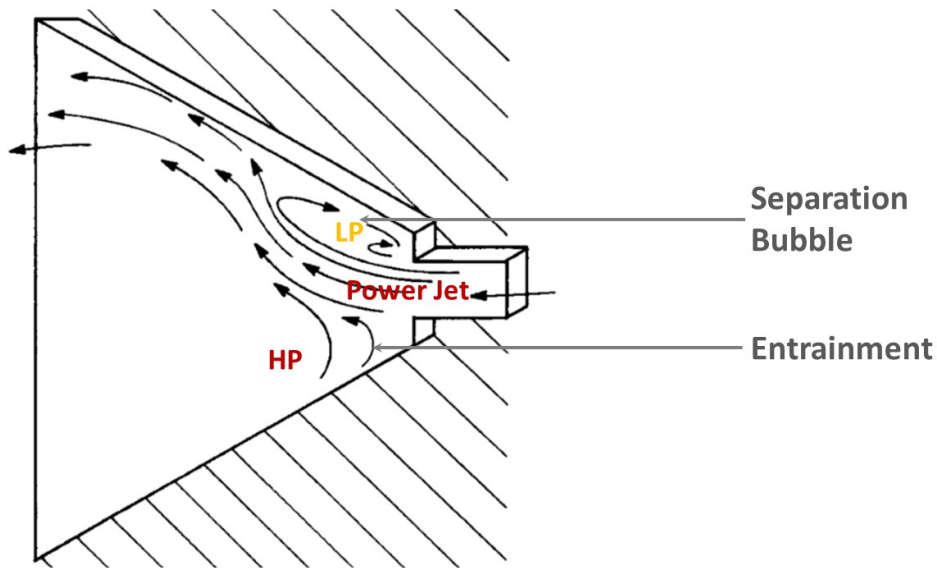
Figure 2.3: A simple wall interaction bistable amplifier design showing different components of an amplifier with relevant widths and angles.

entrainment of fluid occurs at the borders of the jet and carried away through the output ports. The removal of the surrounding fluid through entrainment causes the pressure between the power jet and the adjacent walls to decrease, as shown in the Figure 2.4a. If the pressure is slightly lower towards either of the adjacent walls than the other side, the jet deflects towards that wall. In the figure, the pressure on the top of the power jet is slightly lower than the opposite side. This reduces the proximity of the power jet to that wall and thus decreases the amount of entrainment resulting in the reduction of the pressure. To attain an equilibrium, the higher pressure on the opposite side, where the area for entrainment is comparatively higher (see Figure 2.4b), forces the power jet to lean further towards the other side. This in turn reduces the amount of entrainment because of the reduced area for counter flow, which results in corresponding reduction of pressure. An equilibrium is then attained with the stream attaching on the wall and a recirculating vortex in the low pressure separation region forming a separation bubble, as shown in Figure 2.4b. The detachment of the power jet from the wall will only occur if sufficient flow is allowed to enter the separation bubble to equalize the entrainment characteristics. With enough control flow (not shown in the figure), the stream can be forced to attach on the other wall. [48, 49]

Figure 2.5 shows the internal velocity field at different stages of switching in a wall attachment bistable amplifier, similar to the amplifier used in the present study. It is extracted from the flow simulations performed by Bobusch [50]. The different colors indicate magnitude of the velocity in axial direction and the streamlines indicate the direction of the flow. In the Figure 2.5a none of the control ports is open. The power



(a) Initial flow



(b) Attachment

Figure 2.4: Initial flow of the power jet in the interaction zone and wall attachment. It shows the occurrence of the pressure difference due to the entrainment, the leaning of the jet towards the wall and finally, the wall attachment. [47]

jet attaches on the upper wall and passes undisturbed through the outlet channel. A very small separation bubble is observed at the base of the wall. This however grows

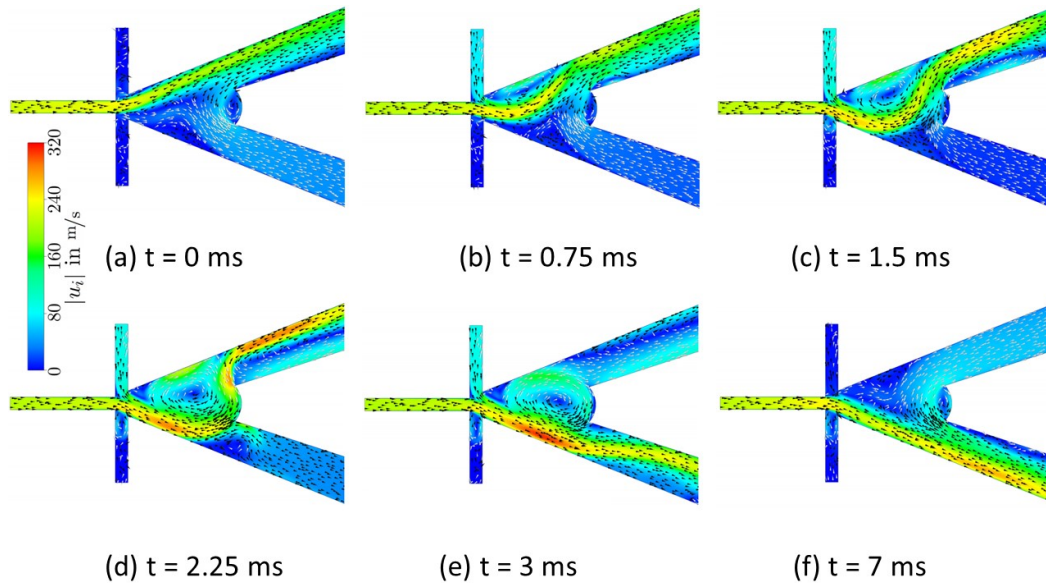


Figure 2.5: Velocity field in an amplifier at different stages of switching, starting at the opening of the control flow. The black arrows represent the flow from left to right and the white arrows from right to left. [50]

in size, as the control port is opened, as can be seen in Figure 2.5b&c. With the growing separation bubble, the flow deflects towards the opposite wall. The cusped structure induces the formation of a vortex in the interaction zone, which further pushes the power jet towards the opposite wall, as observed in Figure 2.5d&e until the flow is completely switched to the opposite output port.

The design of a wall attachment amplifier is a complex process because there is a considerable interaction of various design and operation parameters. During the design of an amplifier some important aspects have to be considered. The design of an amplifier shall be varied by combining the properties of two extreme designs, a low gain but stable system and a high gain system that however tends to oscillate, to have desirable characteristics [48]. These two extreme designs are presented in Figure 2.6. It shows different widths and distances as a factor of the power nozzle width for the two extreme designs. Before proceeding to the design of an amplifier for this work, the significance of different geometrical aspects is studied.

The shape and position of the adjacent walls play a prominent role in energy recovery (the amount of energy remaining in the outlet flow), required amount of control flow to switch the main flow and the susceptibility of the flow to oscillate. For high energy recovery, the receiver of the outlet should be placed closer to the power nozzle, i.e., the splitter distance should be smaller [48]. Similarly, Reilly and Moynihan [51] suggest that large control port areas and small setback distances increase the slope of the jet deflection. It is important that, for a stable outlet flow, the receiver must be located after the re-attachment point of the power jet to collect the flow.

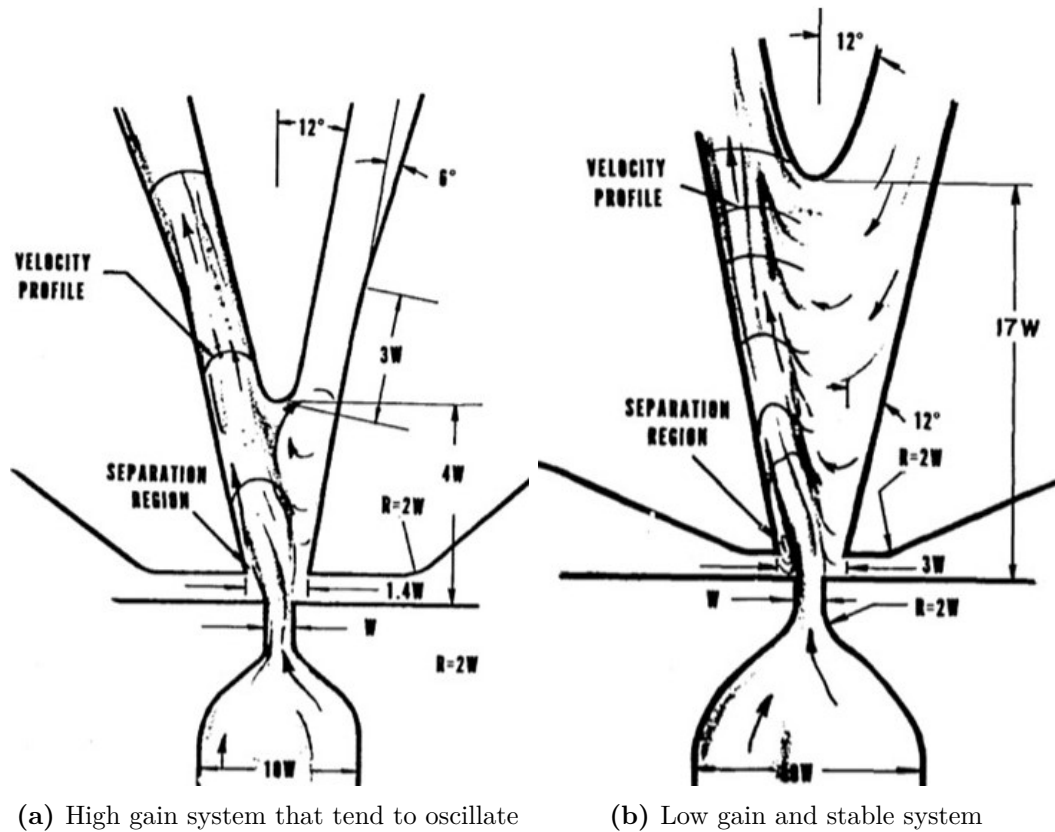


Figure 2.6: Extreme designs of the fluidic amplifier. [48]

The distance of the re-attachment point from the power nozzle can be reduced by selecting a small wall angle and setback distance. For a small wall angle and setback distance, the separation bubble is also small, hence, the location of the re-attachment point is also closer to the power nozzle. Similarly, the velocity of the jet is reduced with an increasing distance of the jet downstream from the power nozzle, so the pressure recovery associated with the decreased velocity in the receiver is also lower. Therefore, in order to have a high pressure recovery, wall angles as well as setback distance and receiver distance from the power nozzle have to be small [52].

However, for high flow gain a large wall angle is desirable. The flow gain is characterized as the ratio of the outlet mass flow to the control flow [49]. But the length of the separation bubble and the corresponding re-attachment point increases with larger wall angle and hence the splitter has to be placed further downstream for a stable outlet flow. This however causes loss in pressure recovery in the outlet receiver, as discussed earlier.

As previously mentioned, for a certain wall angle the power jet attaches on the wall at a certain distance from the power nozzle. This distance increases due to the deflection caused by the impulse of the control flow, as if the wall angle is increased.

This effective wall angle is also increased by the restriction of the flow caused by small setback distance. The small setback distance results in pressure rise in the control port at the edge between the side wall and the control port, which further increases the deflection. Therefore, the effective wall angle has to be considered while designing the amplifier. Increasing the setback also increases the bubble length by increasing the re-attachment point of the power jet. [52]

In case of the constricted receiver, i.e., the cross-section of the receiver is small to accommodate the flow coming from the interaction zone, the total pressure rises in the receiver because of the blockage. Some of the excess flow passes across the splitter and some of it reverses back into the separation bubble, where the pressure is low. To incorporate the increased counter flow, the length of the bubble increases, similar in case of increased control flow into the bubble. This might cause in switching of the jet. This effect can be overcome by lengthening the wall, which however reduces the flow gain. If the receiver is constricted and the splitter is pointed, the excess flow will pass down the other output channel. However, if a cusped shape is used the flow will reverse back into the jet and the pressure on the outside of the bubble increases. This results in compressing of the separation bubble and preventing it from lengthening [49].

The width of the output receiver is also another important parameter. If the width is large, a large amount of flow passes out through the channel under no-load condition. This however results in decrease of dynamic pressure because a large portion of the fluid has low velocity. On the contrary, if the receiver is narrow, the pressure recovery is high, the flow at the outlet has high velocity, however, the output flow is decreased because large portion of the flow is circled back to the interaction zone and might as well pass through the inactive outlet port. Foster and Parker [52] suggest that the outlet size be about the same or slightly less than the size of the supply port.

2.6 Master-Slave Concept

The Master-Slave concept in fluidics is a two-stage layout to generate a desirable frequency in an oscillator stage, whose output switches a large mass flow downstream of an amplifier stage. In this context, the oscillator acts as a master giving frequency commands and the amplifier as slave obeys and switches accordingly. Although, the working principle seems simple, the practical realization of this concept is very demanding and hence its industrial implementation has not been found. The independent realization of the oscillator and amplifier is already challenging, the additional task of matching the properties between them is even more difficult. This difficulty arises basically from large number of inlets and outlets consisting of different conditions, i.e., pressure and flow rate, which have to be matched simultaneously. It has to be noted that, the conditions of one port, for instance pressure at the outlets, affect that of every remaining port. The influence of those conditions of one port to that of the other ports is not linear. This complicates the matching of the oscillator and the amplifier. [44]

2 Theoretical Background

Figure 2.7 shows the schematic representation of the master-slave oscillator (left)

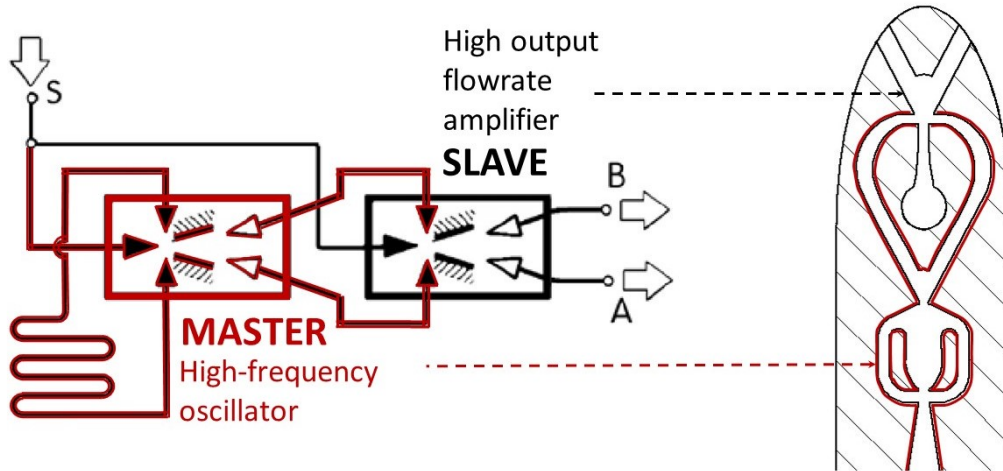


Figure 2.7: Schematic representation of the master-slave concept (left) [44] and its implementation (right). The red demarcated illustrations represent the master and the black represent the slave.

and its implementation for the present work (right). The red demarcated illustration in the schematic representation shows the master. It consists of an input and two outputs. The serpentine structure with two arrowheads is the feedback loop. The outputs of the master end up in the slave, which is illustrated in black color. They impart the information from the master to the slave structure. The slave also has an input and two outputs. The input is subjected to the information coming from the master. The output then switches between A and B. This schematic representation is implemented in the right figure. The red demarcated component is the oscillator (master) and the black component is the amplifier (slave).

The problem associated with the coupling of frequency and amplitude could be mitigated using a bistable fluidic amplifier in combination with a fluidic oscillator in master and slave arrangement, as mentioned earlier. The fluidic oscillator used in the preceding study [25] is combined with the fluidic amplifier to control the frequency and amplitude independently. In this combination, the fluidic oscillator delivers a control flow, which gives the frequency information to the main flow. The amount of the flow can therefore be adjusted as required. In this way, the amplitude and frequency of the control flow for the actuation of the PVC can be adjusted independently.

3 Mathematical Background

The used mathematical methods for the evaluation of the measured and simulated data are briefly discussed in this chapter.

3.1 Root-Mean Square Value

The root-mean square (RMS) value of a time signal $(x(t))$ over a range of $[0, T]$ is calculated as the square root of the average of squared value given by:

$$E_{RMS} = \sqrt{\frac{1}{T} \int_0^T (x(t))^2 dt}. \quad (3.1)$$

For N discrete samples $[x_1, x_2, \dots, x_N]$, the RMS value is calculated as:

$$E_{RMS} = \sqrt{\frac{x_1^2 + x_2^2 + \dots + x_N^2}{N}}. \quad (3.2)$$

In the evaluation of the velocity measurements obtained from the simulation and hot wire measurements, RMS value is used in this work as a measure of the mean amplitude. It is desired to weigh the peaks more than the minimums of the oscillation signals measured using hot wire measurement, so RMS values are calculated instead of the simple mean values. The minimum of the velocity signal measured using hot wire technique is prone to errors, which is further detailed in Section 5.1.3 (*Constant Total Mass Flow*).

3.2 Fourier Transformation

For a non periodic and non time-limited signal $x(t)$, the frequency contents in the signal can be calculated by the Fourier transformation as:

$$X(f) = \int_{-\infty}^{\infty} (x(t)e^{-i2\pi ft} dt), \quad (3.3)$$

where, f represents the continuously varying frequency, t represents time and i represents the imaginary number. However, for a N time discrete signal with discrete samples $[x_0, x_1, \dots, x_{N-1}]$, the coefficients of the Fourier transformation (X_r) can be

3 Mathematical Background

calculated as:

$$X_r = \frac{1}{N} \sum_{l=0}^{N-1} x_l \omega_N^{rl}, \quad (3.4)$$

where, $r = 0, 1, \dots, N - 1$ and $\omega_N = e^{-i2\pi/N}$ [53]. In this work, the Matlab function *fft()* is used to assess the peak frequency and amplitude of the FFT of the simulated time signals.

3.3 Spatial Fourier Mode Decomposition

The pressure signals measured from four circumferentially arranged sensors are decomposed into Fourier modes. The spatial Fourier mode decomposition in azimuthal direction for the m_{th} azimuthal mode can be estimated as:

$$\hat{p}_m(t) = \sum_{k=1}^4 p_k(t) e^{i2\pi m \frac{k}{4}}, \quad (3.5)$$

where, p_k represents the pressure signal of the k^{th} sensor and m represents the azimuthal wavenumber. With the four equidistantly placed and circumferentially arranged sensors, azimuthal modes of $m = [0, 1, 2]$ can be determined. The estimated Fourier coefficient $\hat{p}_m(t)$ is a function of time and complex in nature. For azimuthal number of unity $m = 1$, the Fourier mode $\hat{p}_1(t)$ represents the PVC in its instantaneous amplitude and phase. [24]

3.4 Power Spectral Density

Based on the energy content per frequency band, power spectral density is estimated for the quantitative evaluation of the pressure signals. The power spectral density is estimated as:

$$PSD(\omega) = \lim_{T \rightarrow \infty} \frac{1}{T} |\tilde{X}_T(\omega)|^2, \quad (3.6)$$

where, \tilde{X}_T is the Fourier transformation of $x(t)$ and T is the length of the time interval. For finitely large time intervals, the power spectral density can be estimated as:

$$P_{xx}(\omega) = \frac{1}{T} |\tilde{X}_T(\omega)|^2. \quad (3.7)$$

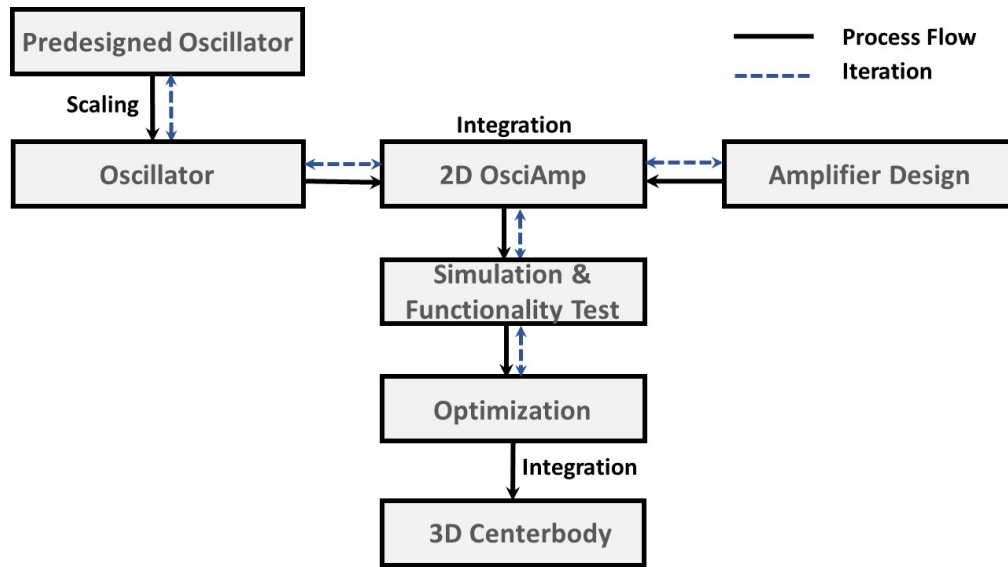
The power spectral density obtained by Welch-averaging of the Fourier decomposed pressure signal over the different time windows is used in this work for the analysis. The averaging is necessary to reduce the noise of an imperfect and finite signal. The choice of window type and size is detailed in section 5.4.3 (*Results of the Differential Pressure Measurement*).

4 Fluidic Actuator Design

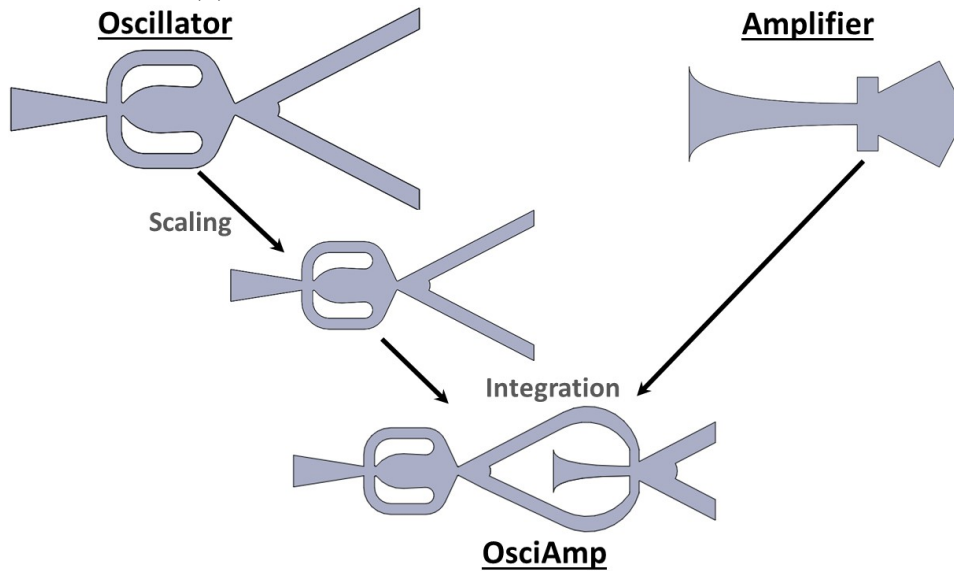
The positive aspects of the fluidic actuator for the control of the PVC in the swirl-stabilized combustion chamber and the required knowledge of the fundamental theoretical aspects follow the design and manufacturing of the fluidic actuator. Figure 4.1 demonstrates the design process used for the construction of the fluidic actuator. A feedback type of oscillator used in a preceding study [25] at the TU Berlin is scaled down, such that the total mass flow after the integration of the amplifier remains in the same range as that of the original oscillator. The scaling down is also necessary to contain the oscillator and amplifier combination in the centerbody with fixed dimensions. Simultaneously, a wall interaction bistable amplifier is designed using a reference geometry, provided by the company FDX Fluid Dynamics GmbH, and the knowledge gathered from various literature. The output ports of the oscillator are connected to the control ports of the amplifier. The resulting construction is named OsciAmp. The flow in the obtained 2D OsciAmp is then simulated for the desired functionality tests. The analysis include pressure distribution, flow and switching characteristics, desired frequency and velocity at the output and the possibility of the independent adjustment of the frequency and the amplitude. The design process comprises a number of iterations until the design goals are reached. The final 2D design of the OsciAmp is then integrated in a 3D design of the centerbody.

4.1 Design of the Oscillator

The feedback type of oscillator used in the preceding study [25] is also used in this work. In the study, Barkwoski used a fluidic oscillator designed by FDX Fluid Dynamix GmbH and integrated into a centerbody designed by Lückoff *et al.* [23]. Oscillators without and with various types of splitters were subjected to the actuation of the PVC. The positions of the outlets in the centerbody were also varied. Of all the designed oscillators, the oscillator selected for this study demonstrated best actuation characteristics. A mass flow of 0.83 kg/h was used at the design point. This mass flow was determined in relation to the impulse coefficient of lock-in amplitude of $C_\mu = 0.155$ for a Reynolds number of 16,000 from the preceding study performed by Lückoff *et al.* [23]. The oscillator design is scaled down in this study, such that the total mass flow after the integration of the amplifier remains in the same range as that of the original oscillator. Moreover, the scaling down is also necessary to contain the oscillator and amplifier combination in the centerbody with a limited space. It is scaled down by a factor of 0.72 in the 2D model and 0.81 in the height. Minor changes in the splitter geometry are carried out in the optimization process, which are discussed in the section 4.6 (*Design of Centerbody*).



(a) Schematic representation of the design process



(b) 2D design of the OsciAmp

Figure 4.1: Design process of the fluidic actuator. The upper diagram shows the schematic representation of the design process of the 3D centerbody. The black arrows show the direction of the process flow and the blue arrows the iteration. The lower diagram shows the design process of the OsciAmp. It illustrates the scaling down of the predesigned oscillator and the design of the amplifier, which are integrated to form a 2D design of the OsciAmp.

4.2 Design of the Amplifier

A bistable wall attachment type of amplifier is designed in this study. The geometry of the used amplifier is derived from the study of Tesař *et al.* [54] and from the design of Bobusch [50]. It is designed as a compromise between the two extreme designs, a low gain but a stable system and a high gain system that however tends to oscillate, as illustrated in Figure 2.6 in section 2.5.2 (*Fluidic Amplifier*). In addition to that, the design challenge includes the limited space within the centerbody and a high splitter angle required for the actuation. A splitter angle of 55° is necessary for the actuation of the PVC at the point of high receptivity, namely between the corner recirculation zone and central recirculation zone. This high wall angle increases the flow gain but also increases the length of the separation bubble and hence the splitter has to be placed further downstream causing loss in pressure recovery. As discussed in section 2.5.2 (*Fluidic Amplifier*), it is preferable that the location of the output receiver to collect the flow be placed after the re-attachment point of the separation bubble. At the same time, for high energy recovery the desired receiving openings of the outlets should be placed closer to the power nozzle as possible. Five times the input port width, i.e., 10 mm distance is thought to be adequate by the author.

In case of the constricted receiver, i.e., the cross-section of the receiver is small to accommodate the flow coming from the interaction zone, the total pressure rises in the receiver because of the blockage. Some of the excess flow passes across the splitter and some of it reverses back into the separation bubble (see Figure 2.4), where the pressure is low. To incorporate the increased counter flow, the length of the bubble increases, similar in case of increased control flow into the bubble. This might cause in switching of the jet. This effect can be overcome by lengthening the wall, which is however not possible in the present case because of the limited space. This problem is mitigated by using a cusp-shaped splitter. Because of its concave structure, the flow is circled back into the jet and the pressure on the outside of the separation bubble increases. This results in compressing of the bubble and preventing it from lengthening. At the same time, the undesired excess flow towards the inactive outlet port is also prevented. Foster and Parker [52] suggest that the outlet size be about the same or slightly less than the size of the supply port. Since, a large width of the control port (2 mm) is used in the designed amplifier, which is equal to the width of the supply port, a 3.9 mm width of the outlet receiver is used. This width should be sufficient to collect the power jet including the control flow without drastic increase of the pressure at the receiver.

Since, for a small setback distance the separation bubble is also small, one could orient for smaller setback distances. However, it should be considered not to constrict the power flow. Moreover, in the present case, where the outlet position and the angle of the wall is fixed, the only remaining possibility to reduce the setback distance would be by elongating the side walls in upstream direction. This however is not possible due to the limited space. So, a setback distance of 4 mm: twice the width of the power nozzle is used. To decrease the pressure required for the switching, the control port width is selected relatively higher compared to that of the design

4 Fluidic Actuator Design

of Tesár *et al.* [54]. The increased width is also necessary to incorporate the wider outlet arms of the oscillator. The control ports have a width of 2 mm same as that of the power nozzle.

4.3 Design of the Fluidic Actuator

The fluidic actuator used in this study is a combination of oscillator and amplifier. Figure 4.2 shows the first version V1 of the designed actuator with relevant dimensions. The output ports of the oscillator are connected to the control ports of the amplifier. The oscillator and amplifier are positioned as close as possible to use the limited space as well as reduce the length of the channels connecting them. The output ports of oscillator with 2.9 mm diameter at an angle of 52.7° and gradually converge to 2 mm control ports of the amplifier.

The design of the fluidic actuator follows the simulation of the flow. Other design changes required after the simulation for the optimization are covered in the section 4.5 (*Variation of Fluidic Actuator Designs*).

Figure 4.3 illustrates the nomenclature scheme for the clarity of the nomenclature of different actuator designs used in this work. The names in each box are used individually or as a combination to denote the respective entity.

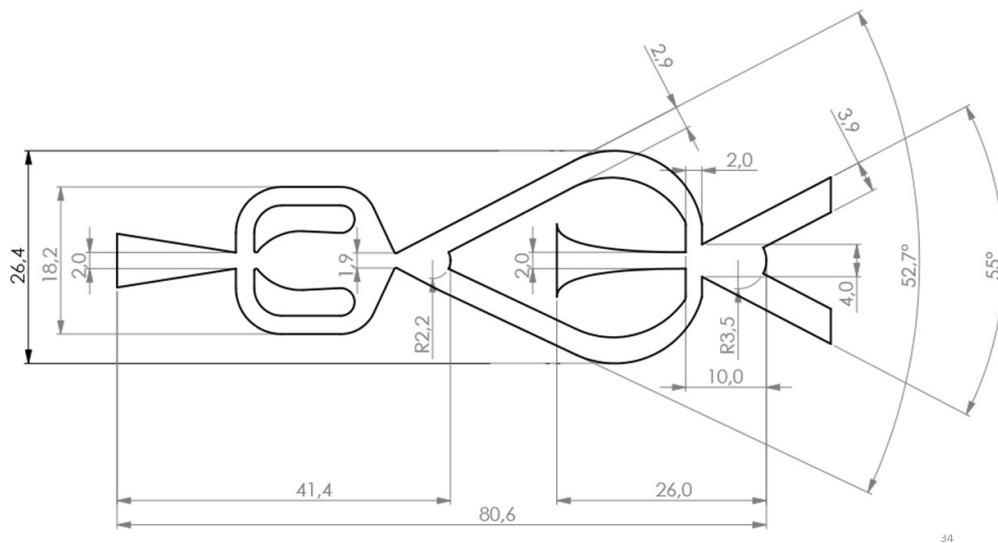


Figure 4.2: Construction diagram of the fluidic actuator (V1) showing relevant dimensions.

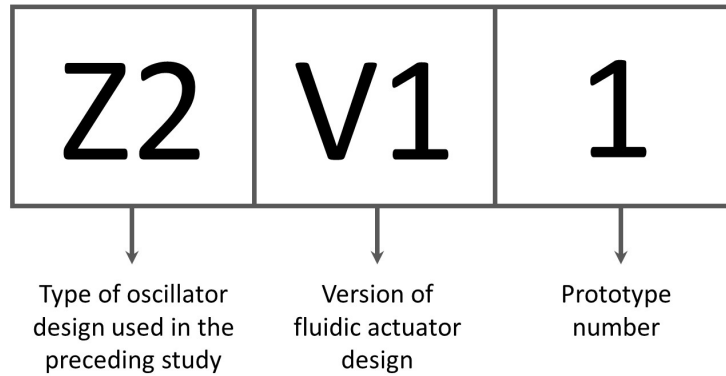


Figure 4.3: Nomenclature scheme used for different designs of the actuator.

4.4 Flow Simulation

After the actuator as a combination of oscillator and amplifier is designed in the commercial software SolidWorks, a 2D simulation of the flow within the actuator is performed using the commercial simulation program Ansys. The simulation is performed in assistance of FDX FluidDynamix GmbH and the result is provided to the author. Reynolds-averaged Navier-Stokes (RANS) equation is solved for incompressible air. The received data is assessed to evaluate the functionality of the components. In the first round of the simulation, a total mass flow of 1.8 kg/h is used: 0.9 kg/h through each of the inlets of the oscillator and the amplifier. Figure 4.4 shows one oscillation cycle of the actuator (Z2.V1) obtained from the simulation of the flow inside the actuator. The stream lines show the flow field and the colored contours show the absolute pressure distribution. In the initial stage, as shown in the Figure 4.4a, the bottom control port of the amplifier is supplied by the oscillator, which pushes the flow through the amplifier inlet port towards the opposite side, switching the actuator to the top outlet. Gradually, the flow through the oscillator is switched to the opposite control port, which causes the formation of a separation bubble, as shown in Figure 4.4b. The separation bubble grows in size and pushes the power jet of the amplifier towards the opposite outlet port, as seen in Figures 4.4c & 4.4d.

To check the functionality of the actuator, the time signal of the x-component of the velocity u at the middle of the exit of the outlet port is plotted, as shown in the Figure 4.5. The flow at the exit of the outlet port is selected for the evaluation because it directly influences the actuation property of the actuator. The phase averaged and the low pass filtered signal (cut-off frequency 800 Hz) is plotted along with the raw signal. The figure shows little fluctuation at the peak. It however shows a good switching characteristics. The switching in a bistable amplifier is characterized by two stable states: flow through the outlet (ON) and no flow through it (OFF).

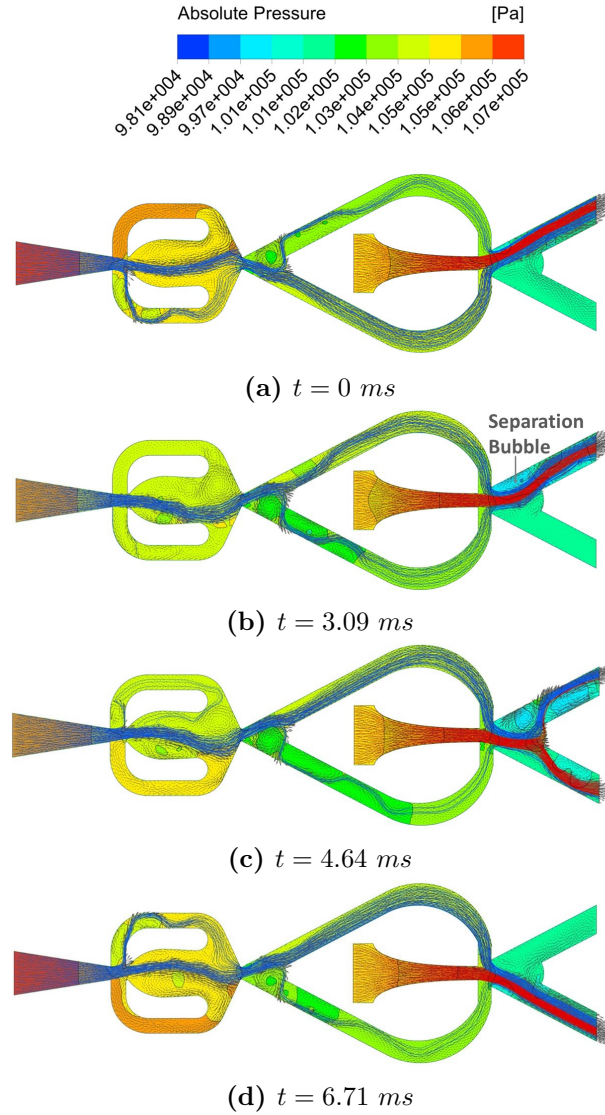


Figure 4.4: A single oscillation cycle of the actuator (Z2.V1). The streamlines show the flow field and the colored contours show the absolute pressure distribution.

The initial rise and falling of the velocity at the peak is presumably because of the formation of the separation bubble at the base of the side wall. At the point of switching, the flow enters the output port directly, resulting in the rise of the velocity. Immediately, a separation bubble starts to form and directs the flow towards the side wall resulting in the cross flow. Hence, the x-component of the velocity decreases.

The next concern is to verify, if the frequency of the oscillation could be varied by keeping the total mass flow constant. To keep the total mass flow constant,

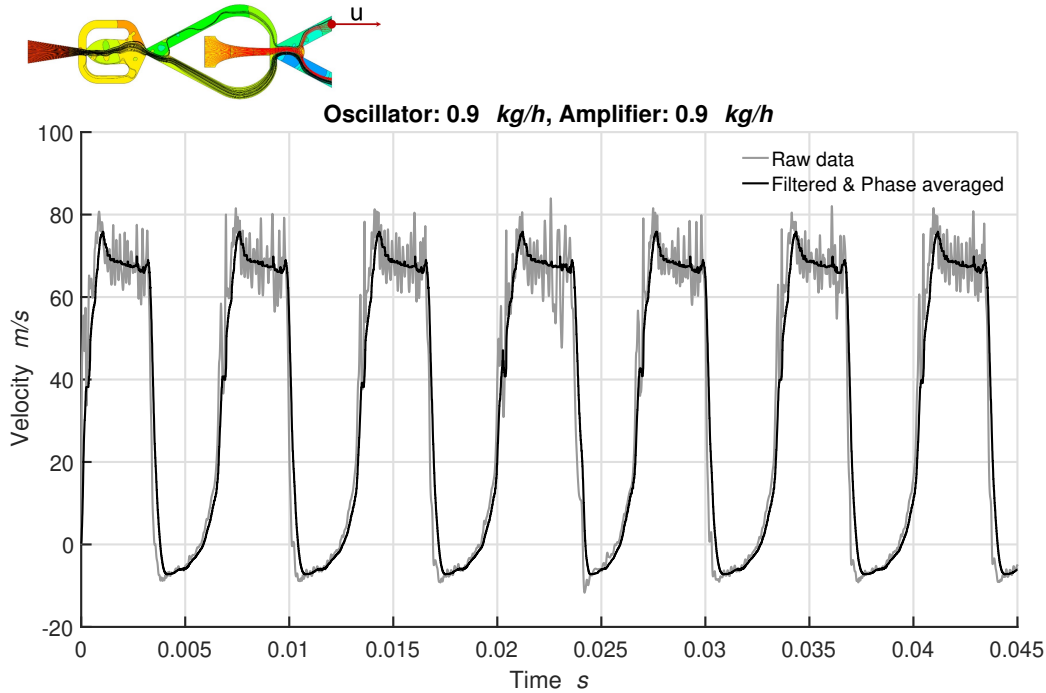


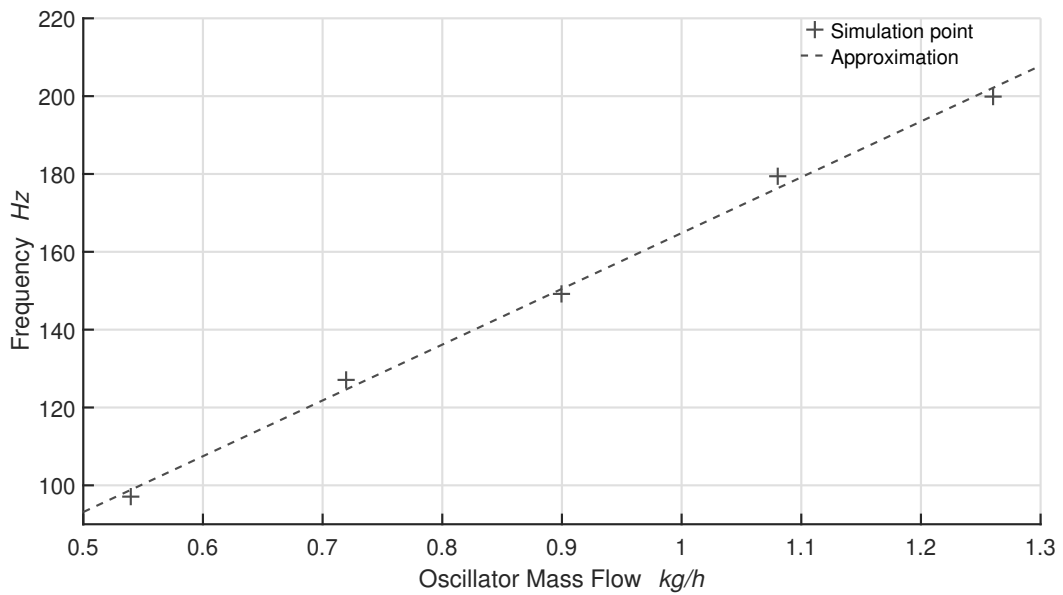
Figure 4.5: Axial velocity component of the flow at the outlet of the fluidic actuator (V1).

the ratio of the flow through the oscillator and the amplifier is varied. It is again noted that the sum of the mass flows through the oscillator and the amplifier is kept constant. A total mass flow of 1.8 kg/h through the actuator is used for the simulation of the flow by using five different combinations of mass flows through the oscillator and the amplifier. The results of the simulations are illustrated in the Table 4.1. It can be vividly seen in the table that the frequency increases with the increase in the oscillator mass flow. On the contrary to the expectation that the RMS value of the velocity should remain constant for the constant total mass flow, it however increases slightly for increasing oscillator mass flow. Nonetheless, the relative difference between the maximum and the minimum RMS values of the mentioned five cases is 14.1 %. Although, the relative difference is slightly higher than the expectation, this is a very promising result as it demonstrates one of the fundamental goals of this study, i.e., the adjustment of different frequencies for a constant amplitude.

Figure 4.6 illustrates further the linearity of the frequency with respect to the oscillator mass flow. Figure 4.7 shows the axial component of the velocity u at the middle of the exit of the outlet port for the above mentioned five cases of the combination of different oscillator and amplifier mass flows. It is noted again that the total mass flow in each of the cases is constant. For the oscillator mass flow of 0.54 kg/h, the oscillation is not quite distinct. It is apparent from the time signal of

Table 4.1: Variation of the oscillator and the amplifier mass flow in the fluidic actuator (V1)

Osci. kg/h	Amp. kg/h	Total Mass kg/h	Freq. Hz	RMS m/s
1.26	0.54	1.8	199	52.2
1.08	0.72	1.8	181	50.7
0.90	0.90	1.8	148	48.1
0.72	1.08	1.8	128	47.4
0.54	1.26	1.8	93	45.3

**Figure 4.6: Linearity of the frequency with respect to the oscillator flow in the actuator (V1).**

the velocity that a certain amount of flow passes across the inactive outlet port of the actuator. This is shown by the fluctuation of the signal between the two relatively stable peaks. Similarly, for the oscillator mass flow of 0.72 kg/h, the oscillation can be categorised as stable, however, the peak velocity is extremely fluctuating. In the rest of the cases of the oscillator mass flow, the oscillations are distinct and the peak velocities lie approximately between 70 and 80 m/s.

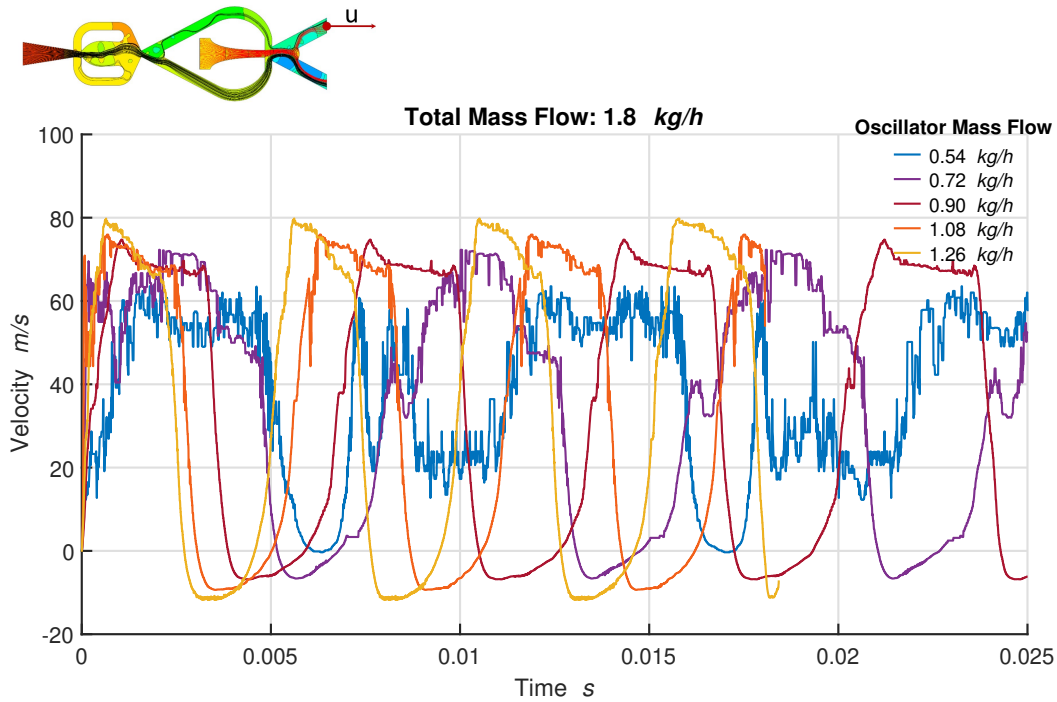


Figure 4.7: Velocity signal for the different oscillator and amplifier mass flow in the fluidic actuator (V1).

4.5 Variation of Fluidic Actuator Designs

For studying the flow characteristics and functionality of the fluidic actuator for the variation in geometry, its geometry is varied and simulated for equal mass flow in the oscillator and the amplifier. Figure 4.8 shows the flow field and the pressure distribution within the actuator obtained from the simulation of the flow performed on different design versions of the actuator. At this point however, the geometrical changes made on the different versions of the actuator is important to observe.

The upper diagram in the Figure 4.8 shows the first version of the actuator with the relevant dimensions that are varied in the other versions of the actuator. The flow simulation of the first version V1 showed an unexpected small amount of flow in the inactive outlet port of the oscillator, as pointed out in the figure with a red arrow. This undesired flow through the inactive outlet port of the oscillator is most probably caused by the curvature of the splitter (cusp shaped structure), whose end is directed perpendicular to the side wall. So, the excess flow to the active port is directed perpendicular to the side wall of the inactive port, instead of circling back to the interaction zone. Hence, the flow passes through the outlet channel of the inactive outlet port of the oscillator.

4 Fluidic Actuator Design

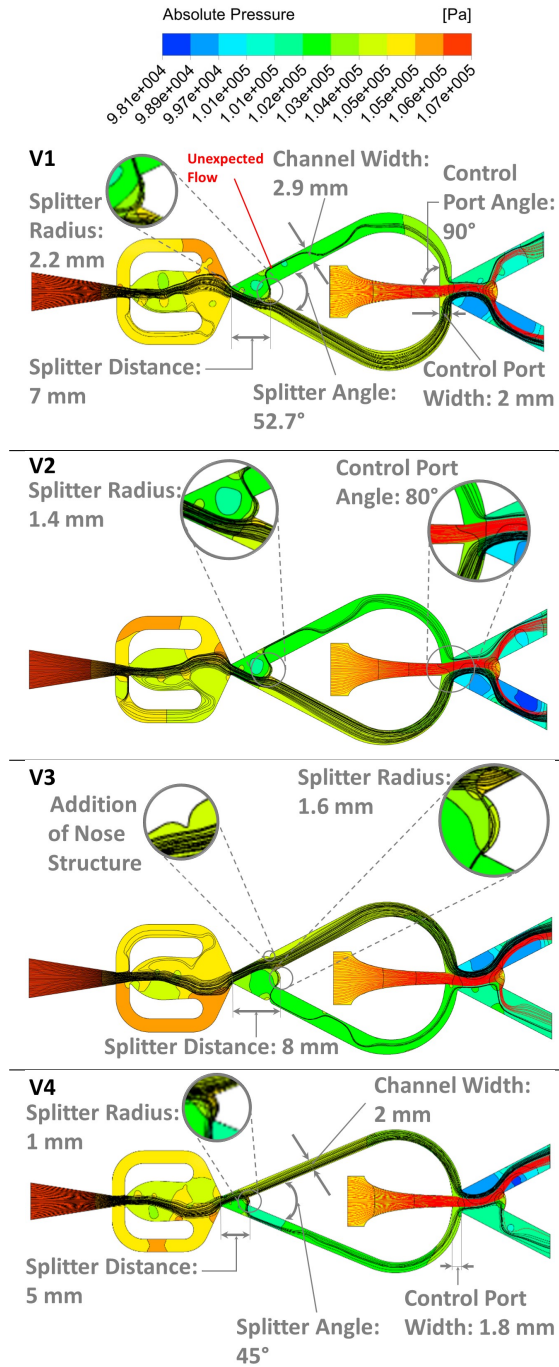


Figure 4.8: Different versions of the fluidic actuator showing the flow field (streak lines) and pressure distribution (colored contours). The top figure shows the relevant dimensions of the first version of the actuator. The rest of the diagrams show the geometric variations carried out in the respective versions of the actuator.

4.5 Variation of Fluidic Actuator Designs

Therefore, in the second version V2, the radius of the splitter is decreased to 1.4 mm to increase the curvature of the splitter to circle down the excess flow towards the interaction zone. This however did not bring significant change in the flow. The outlet flow of the oscillator is deflected at a very high deflection angle of 153.65° before it exits through the control port of the amplifier. This high deflection angle is associated with loss of pressure. Therefore, to minimize the loss of pressure in the control ports, the angle at which the control ports connect to the amplifier is reduced to 80° .

In the third version V3, a small nose is constructed on the side walls near the oscillator-splitter to catch the back flow of the active port. This however lead to a noisy velocity output due to the generation of turbulence in the flow by the nose structure. The splitter radius of the oscillator is increased to $R = 1.6$ mm and the position is moved 1 mm in the direction of the flow.

In the earlier versions V2 and V3 the control ports are arranged at an angle of 80° to the inlet port of the amplifier. This intends to decrease the pressure loss due to the extreme deflection of the flow, as discussed before. Similarly, to further decrease the loss of pressure, the wall angle of the oscillator output ports (splitter angle) is reduced to 45° in the fourth version V4. This allows to decrease the splitter distance still maintaining the stability of the flow, as discussed in the section 2.5.2 (*Fluidic Amplifier*). The splitter distance is reduced to 5 mm. Additionally, the radius of the splitter is reduced to 1 mm to increase the curvature of the cusp-structure. The increased curvature circles back the excess flow to the interaction zone. In addition to that, the outlet receiver width of the oscillator is reduced to 2 mm. The width gradually decreases beginning at the start of the curve and ending at the opening of the control port with the width of 1.8 mm in the interaction zone. The decrease of the width of the receiver and the control port intends to increase the impulse of the control flow.

To compare the functionality of the mentioned versions, the axial component of the velocity at the outlet of the fluidic actuator is plotted in Figure 4.9. All of the versions of the actuator show a stable switching characteristics, i.e., they switch between the two stable states: ON and OFF. The initial rise and fall of the velocity at the peak is however more distinct in the version V1. A uniformly distributed peak velocity is desired for the actuation. The rise and fall of the velocity is most probably the result of the perpendicular control port to the supply port of the amplifier in the version V1. The control port is inclined at an angle of 80° to the supply port of the amplifier in the other versions of the actuator. Apart from that and the negligible difference in the frequency of the oscillation, no significant difference is observed in the time signal of the velocity of the different versions of the actuator.

The versions V2 and V4 are chosen for the 3D printing. The evaluation of the velocity signal of the actuators shows stable peaks for the versions V2, V3 and V4 compared to the version V1. So, the version V1 is eliminated for the 3D printing and further investigations. Similarly, the version V3 has a nose structure constructed on the side walls of the outlet ports of the oscillator. Because of the complications associated with the printing of the nose structure, the version V3 is excluded as well from the

printing and further investigations.

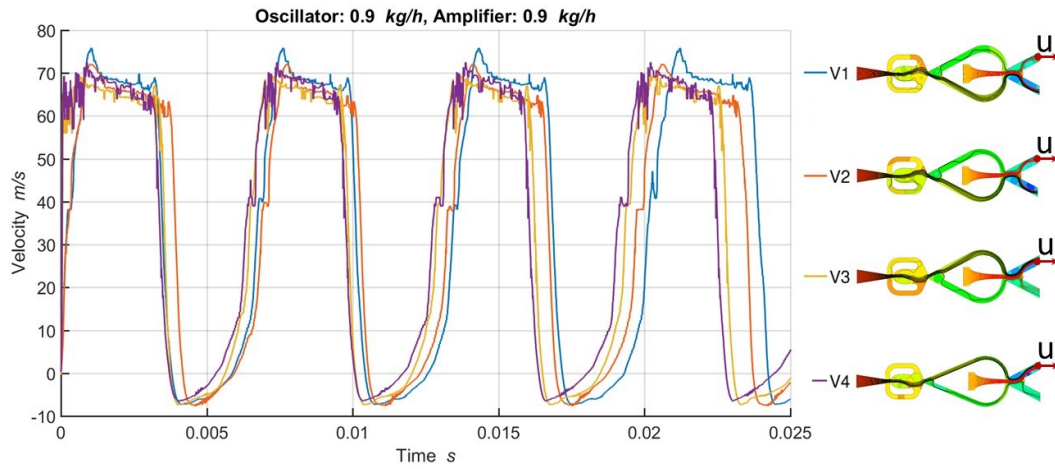


Figure 4.9: Comparison of the flow in the different fluidic actuator designs.

4.6 Design of the Centerbody

After the results from the simulations confirmed the viability of the design, the Z2.V2 and Z2.V4 versions of the fluidic actuator are integrated into the centerbody, which is used in a swirl-stabilized combustion chamber. The centerbody itself is a streamlined shaped cylindrical body with a dome shaped head. The same basic structure is used in this study as in the preceding studies [23, 25]. The study [23] reveals that the dynamics of the PVC are promoted by the parabolic shape of the centerbody's head. The length of the centerbody is 170 mm and the base diameter is 35 mm. The contour of the dome represents a half ellipse with a minor axis length of 35 mm and a major axis length of 43.75 mm. The outlet openings are located 165 mm from the base and has a projected dimensions of 3.9 mm \times 2 mm on the outer surface of the dome.

The required tubings providing the mass flow into the oscillator and the amplifier as well as a fixture to hold the centerbody in the mixing-tube are integrated in the centerbody. Figure 4.10 shows the 2D and 3D images of the centerbody with the relevant dimensions. The centerbody needs to be fixed at the center of the base in the mixing-tube, so a central hole is constructed at the location. At the same time, the actuator (OsciAmp) should be placed in the middle of the centerbody. The inlet channel to the oscillator of the centerbody must therefore be placed off-center of the central hole and then curved around the hole to the inlet port of the oscillator. The opening of the channel is circular in shape and has a diameter of 9 mm, which after the end of the curvatures recedes gradually to the opening of the oscillator inlet. The inlet is rectangular in shape with the dimensions of 6.7 mm \times 2 mm, as can be

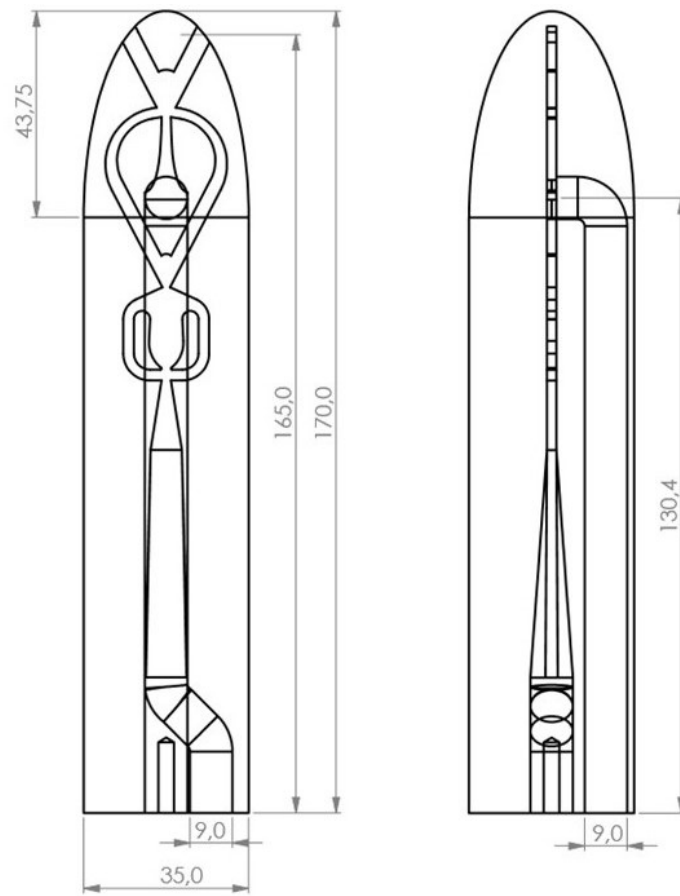
seen in the Figure 4.10a. Similarly, the diagram on the right of the Figure 4.10a shows the duct constructed for the supply flow to the amplifier. The duct extends 130.4 mm from the base of the centerbody to the opening of the inlet port of the amplifier. The channel is also circular in cross-section and has a diameter of 9 mm. A bore hole for the M4 screw is brought at the base of the centerbody for the fixture.

4.7 Manufacturing of the Actuator

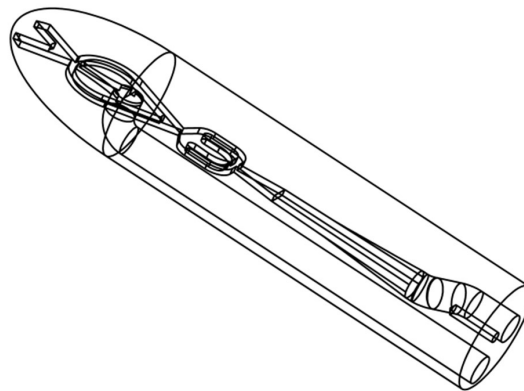
Because of the complications associated with the construction, required high precision along with low cost and easiness, a 3D printing method is selected. The centerbody is printed using a hot-lithography-method. Apart from the required material strength and durability, a material named *Precision* is used for the production of the centerbody, which provides a relatively small surface roughness. For the quality assurance of the 3D printed centerbody, computer tomography (CT) measurements of the centerbody is conducted. It facilitates the nominal-actual comparison of the printed component to the CAD data and control the component of any damages or unwanted cavities with the help of the CT images. After a careful investigation of the pictures of the CT of Z2.V2.1 version of the centerbody, no damage or unwanted cavities are found. Figure 4.11 shows the result of the computer tomography of the centerbody at the origin of the used coordinate system. The images show the cross-section of the center body in the three space direction along with the 3D model of the centerbody. A small amount of chunk of the material is left attached at the inlet and outlet of the amplifier (represented by pink dots in the pictures). The chunk at the inlet has negligible influence on the flow and the chunk at the outlet is removed. The inner geometry is well illustrated with a deviation of $\pm 10\%$, except for the above mentioned chunk attached at the inlet and the outlet of the amplifier. Figure 4.12 shows the construction error on the upper and lower surface of the inner geometry. An effective height of ≈ 1.8 mm can be observed for a 2 mm nominal height. A similar result is observed in other space directions. The computer tomography pictures reveal a sufficient quality of the production. The deviation is still tolerable, however, the functionality of the actuator needs to be verified for the desired flow at the outlet of the centerbody. This is performed by the hot-wire measurement of the velocity.

After carefully polishing the outer surface of the centerbody with a sandpaper, a M4-thread is integrated and linking pipes are glued to it for the coupling of the centerbody with the inlet tubes for the pressured air.

4 Fluidic Actuator Design



(a) 2D image



(b) Isometric view

Figure 4.10: Design of the centerbody (Z2.V2) showing the internal geometry and different arrangements for the flow supply in the oscillator and the amplifier.

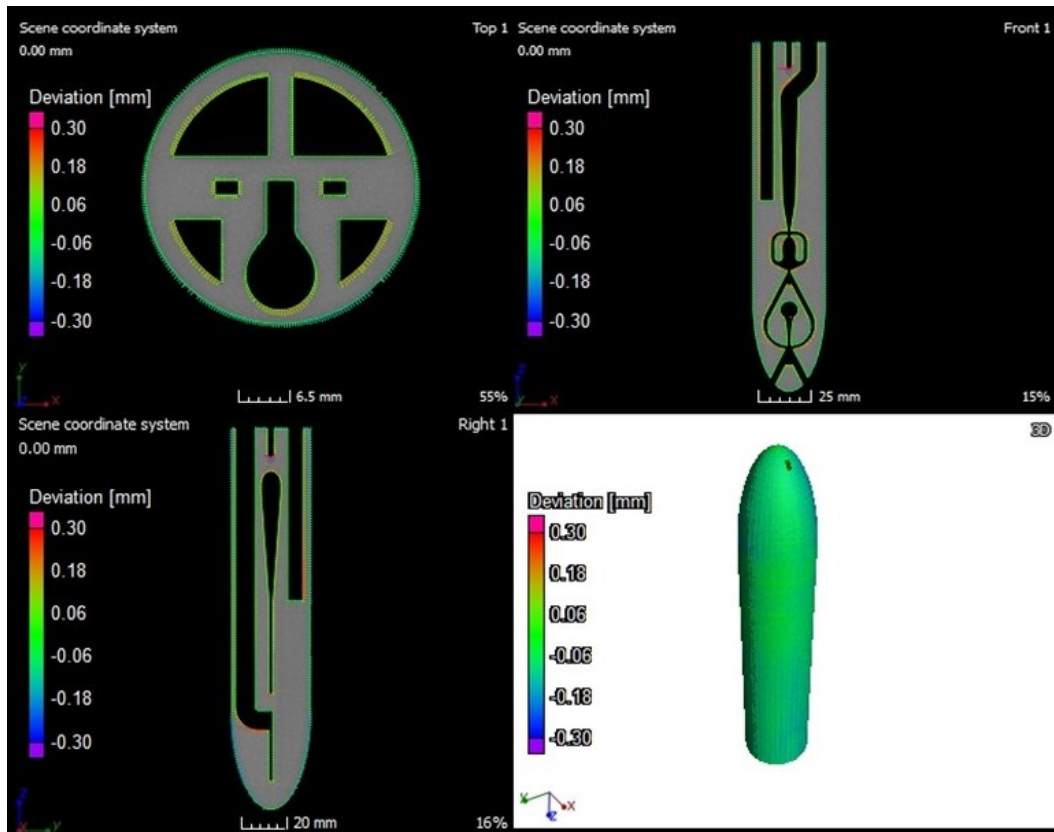


Figure 4.11: Computer tomography of the centerbody (Z2.V2.1) at the origin of the coordinate system (opening of the supply port of the amplifier).

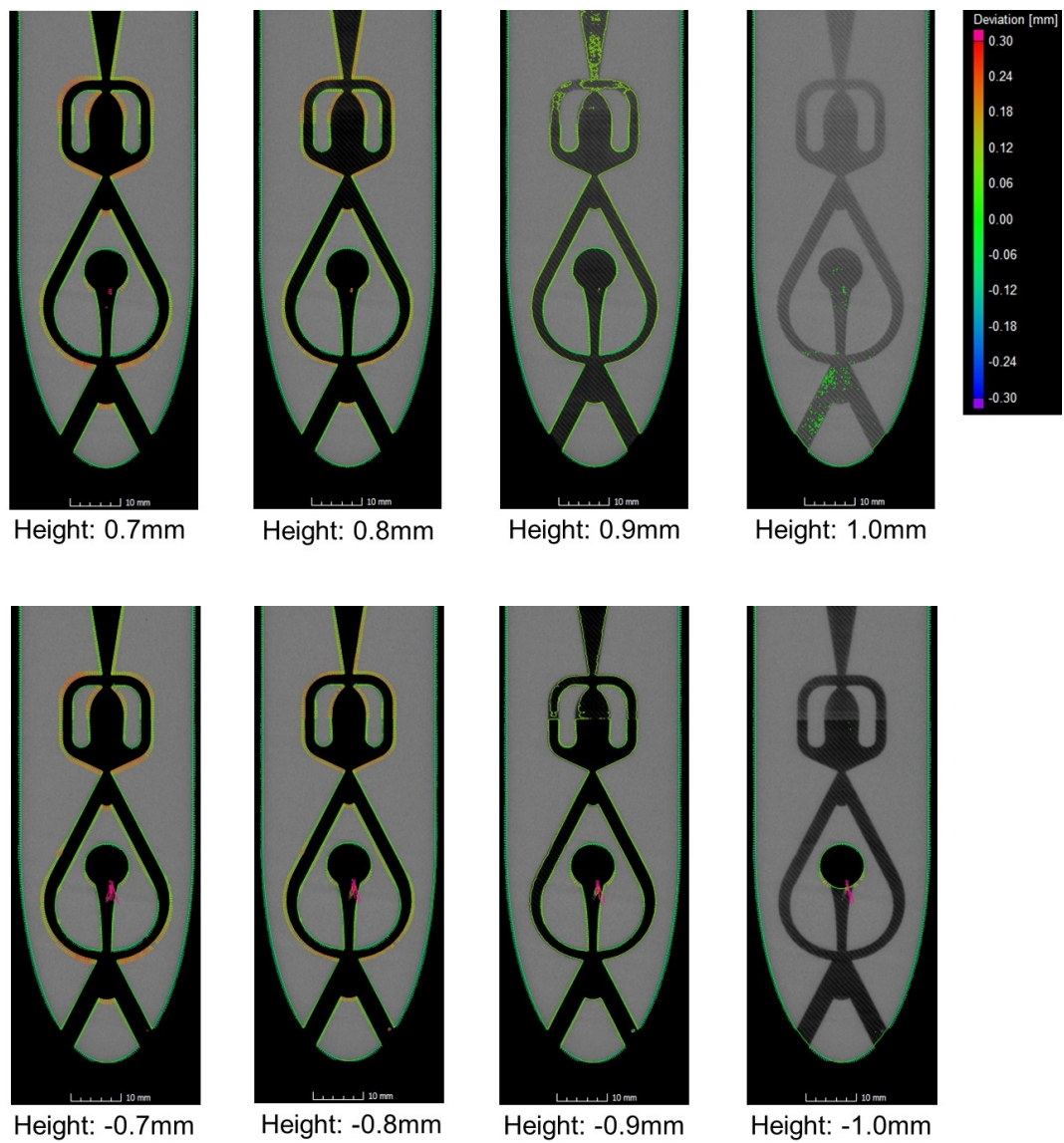


Figure 4.12: CT pictures of the centerbody showing inner geometry at different heights from the origin of the used coordinate system (opening of the supply port of the amplifier).

5 Experiment

This chapter discusses the experimental investigation of the actuator to evaluate the validity of the used actuation concept. The actuation concept is validated by means of three different experiments. The first experiment aims to verify the functionality of the actuator. In addition to that, a parameter study is performed to obtain different frequencies for the corresponding total mass flow through the fluidic oscillator and the amplifier. A hot-wire measurement technique is used to measure the velocity of the flow ejected from the outlet port of the actuator. The second experiment deals with the visualization of the outlet flow of the actuator using Schlieren imaging technique. In the final experiment, the influence of the actuator on the PVC dynamics is investigated. Differential pressure sensors are used for the measurement. The experiments are further detailed in the following sections.

5.1 Hot Wire Measurement

The frequency of a classical fluidic oscillator depends linearly on the mass flow. Similar results are obtained from the simulation of the flow inside the actuator, as shown in the Figure 4.6. This experiment intends to check the desired functionality of the fluidic actuator, verify the linearity of the frequency to the changes in the mass flow through the oscillator and perform a parametric study to obtain a frequency spectrum for different mass flow through the oscillator and the amplifier. This is performed by measuring the velocity of the flow at the outlet of the used actuator by means of hot-wire velocity measurement technique.

5.1.1 Calibration

In this work, a single-wire probe is used. It consists of a thin wolfram wire stretched between two steel supports. Since, the electric resistance of a wire depends on its temperature and the heat dissipation due to convection depends on the flow velocity around the wire, change in the velocity of the flow can be determined by measuring the corresponding change in the electrical resistance of the wire. This concept is used in constant temperature anemometry (CTA) method, where control loops are used to keep the wire temperature constant by simultaneously adjusting the voltage in the loop. The voltage required for the adjustment of the temperature is used as a measure for the change in velocity of the flow around the hot wire.

Since, the resistance of the hot wire depends on various parameters like temperature, pressure and humidity and does not change linearly to the mentioned parameters, it has to be calibrated. A Prandtl tube is used to calibrate the hot-wire probe. Both

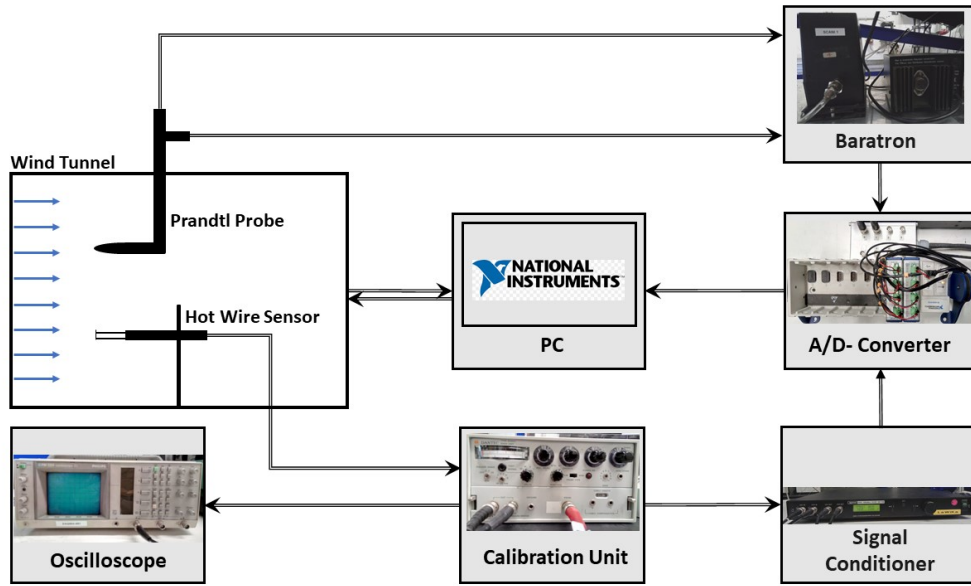


Figure 5.1: Measurement setup for the calibration of the hot-wire sensor.

of the probes are placed in an open wind tunnel aligned facing directly to the flow, as shown in the Figure 5.1. The Prandtl tube measures the total pressure in an opening facing the flow and the static pressure through an opening laterally placed to the direction of the flow. From the two pressure sources, the pressure difference is determined by using a capacitive differential pressure sensor (Baratron) installed downstream of the Prandtl tube. From the differential pressure signal, the velocity of the flow can be determined using the equation:

$$V_e = \sqrt{\frac{2}{\rho}(P_0 - P_e)} \quad (5.1)$$

,where

V_e : velocity of flow at the stagnation point

ρ : density of the medium

P_0 : total pressure at the stagnation point

P_e : static pressure

The Baratron has a measuring range of ± 1000 Pa. The hot-wire probe is connected to a calibration unit, Dantec of type 55M01. The calibration unit is used to calibrate the cold and the hot resistance of the control loop to compensate the influence of the probe and the cable resistance. It is also used to adjust the overheating factor. An oscilloscope is connected to the calibration unit to monitor the signal. The signal

of the hot-wire probe is filtered and amplified with a signal conditioner (type Kemo Dual Variable Filter VBF 10M). To digitally process the analog signal obtained from the hot-wire and the Prandtl tube, the Baratron and the signal conditioner are connected to a 16-bit A/D converter (NI 9239) and digitized with a sampling frequency of 20,000 Hz. The digital signals are then recorded and processed by a measuring computer.

Before the calibration could be started, the ambient conditions are recorded, which are listed in the following table.

Room Temperature	24.6°C
Air Pressure	10100 Pa
Relative Humidity	50 %

The second step is to determine the cold resistance and the overheating factor of the used bridge circuit. With the constant temperature method, the hot-wire probe is used as a partial resistance in a Wheatstone bridge circuit. The cold resistance includes the resistance of the probe cables and the resistance of the hot-wire probe. To determine the resistance of the probe cable, a short-circuit probe is connected to the probe cable and then the bridge voltage is adjusted using the calibration unit. In the next step, the resistance of the hot-wire probe is determined. For this, the hot-wire probe is connected and the bridge voltage is calibrated again. From the two steps, a cold resistance of $R_0 = 5.64 \Omega$ is obtained. In this state, the circuit would heat the hot-wire so that it always has the ambient temperature.

In order to achieve a higher sensitivity of the probe during the cooling of the hot-wire by the flow in the wind tunnel, the wire is overheated. This overheating is achieved by calibrating the bridge voltage of the calibration unit again. Whereby, the cold resistance is increased by the overheating factor α . The overheating factor is defined as an empirical value at $\alpha = 1.6$. The resistance thus obtained is called warm resistance and a value of $R_1 = 9.024 \Omega$ is used for the calibration and the measurement.

After determining the cold and the warm resistance, a suitable amplification factor is determined for the signal conditioner. For this purpose, the wind tunnel is operated and set to a maximum flow velocity of ≈ 24 m/s. This corresponds to a voltage of 8.8 V. A buffer of 1.7 V is left at the upper margin, because higher velocities than 24 m/s are expected during the investigation of the actuator. The signal conditioner is also used to filter the hot-wire signal with a low pass filter. Since frequencies over 250 Hz are not expected, a low pass filter of 500 Hz is selected. This conforms the Nyquist-Schannon criteria to avoid aliasing effects. After these settings, the calibration curve is recorded. For this purpose, sixteen different incident flow velocities are set in the wind tunnel. For each velocity, the voltage of the hot-wire signal and the pressure difference of the Prandtl probe are measured with a sampling frequency of 2,000 Hz for 30 s. The high sampling frequency and the duration of the measurement is beneficial to obtain a quasi-stationary statistical moment of the fluctuating velocities. The velocity is determined from the pressure difference of the Prandtl tube using the internal evaluation software. The velocity and the voltage of

5 Experiment

the hot-wire probe are plotted against each other and approximated with a 4th order polynomial. Equation 5.2 represents the used polynomial for the calculation of the velocity from the measured voltage.

$$f(x) = -0.02855x^4 + 0.91207x^3 - 9.06361x^2 + 37.79590x - 57.55244 \quad (5.2)$$

Figure 5.2 shows the measured values and the polynomial approximation curve.

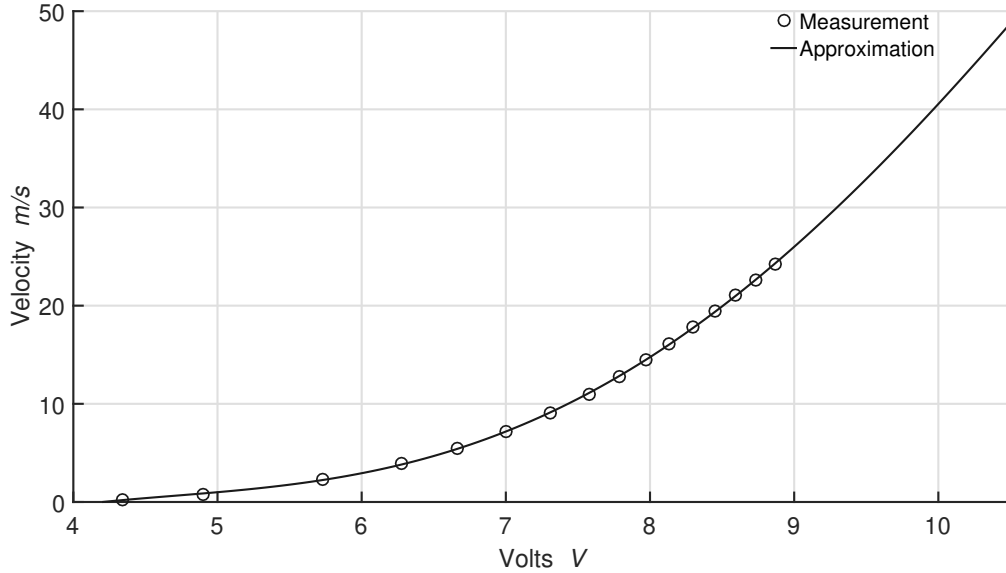


Figure 5.2: Calibration curve showing the locations of the measurement and the approximation.

Because of the limitation of the used wind tunnel, the calibration points measured does not cover the whole range (up to ≈ 50 m/s) of the expected velocity. Therefore, it is approximated in those range using the Equation 5.2.

5.1.2 Measurement

After the successful calibration of the hot-wire probe, the velocities of the air ejected from the outlet of the centerbodies are measured. Figure 5.3 shows the experimental setup for the measurement of velocity using a hot-wire probe. The measurement setup is similar to the calibration process except for the pressure measurement in the Prandtl tube. The hot-wire sensor is connected to the calibration unit, which retains the same settings, that were set during the calibration. To monitor the signal, an oscilloscope is connected to the calibration unit. The signal of the hot-wire probe is filtered and amplified with a signal conditioner. To digitally process the analog signal from the hot wire, the signal conditioner is connected to an A/D converter and digitized with a sample frequency of 20,000 Hz. The digital signals are then recorded and processed by a measuring computer.

The used centerbody is fixed on a table. The velocity is measured at the location at which high amplitude of the effective velocity is registered. So, the hot-wire is fixed on a linear bench allowing its movement in all of the space direction. The mass flow is connected to the actuator through the two openings on the base of the centerbody, each for the oscillator and the amplifier supply. It is important to reach small control flows and control the amount precisely. Therefore, the oscillator mass flow is controlled by a coriolis mass flow controller (type mini Cori-Flow M13V14I). The flow controller is connected to the measuring computer via a COM connection with which the mass flow can be adjusted. Air mass flows up to 1 kg/h with an accuracy of $\pm 0.2\%$ of the mass flow rate could be achieved. Similarly, the mass flow in the amplifier is controlled manually using a rotameter scaled in l/min for every 1 l/min in the range of [4, 50] l/min. This scaling in the rotameter allows the setting of minimum mass flow up to 0.5 l/min (0.04 kg/h) with an accuracy of ± 0.25 l/min (0.02 kg/h) for the minimum setting.

The location of the probe is adjusted such that the amplitude of the effective velocity is maximum and the probe is aligned directly at the opening of the outlet with a sufficient distance as not to damage the hot-wire. A distance of ≈ 15 mm is thought to be appropriate for the measurement. It is important to observe the instantaneous effective value of the velocity signal, so an oscilloscope is connected to the calibration unit to display it. After the alignment, the velocity is measured for different mass flows on both the oscillator and the amplifier inlets. A longer measurement time of 30 s is taken with the sampling frequency of 20,000 Hz to obtain a quasi-stationary statistical moment of the fluctuating velocities.

Two sets of measurements are carried out. In the first set, iterations are performed

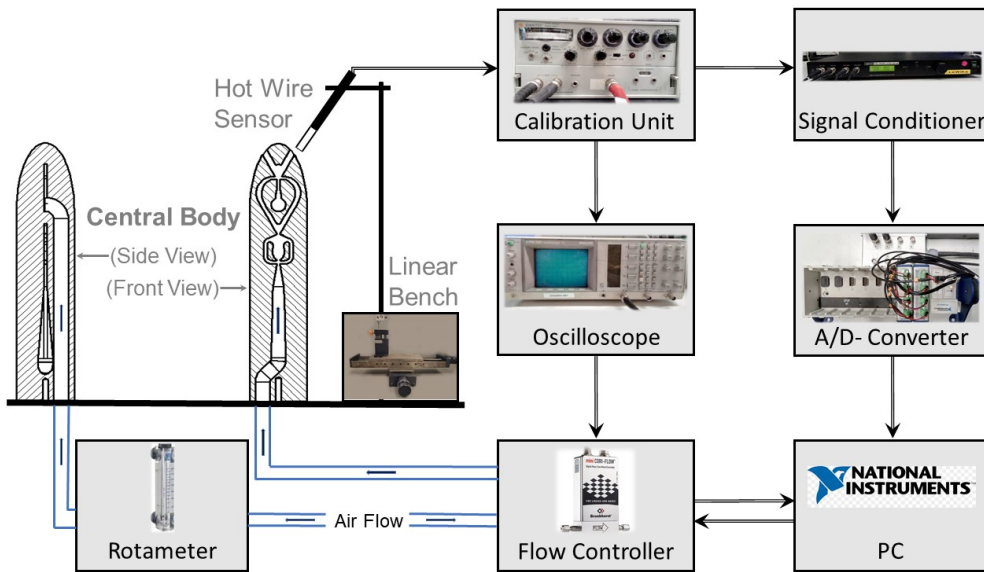


Figure 5.3: Hot wire measurement setup.

by changing the amplifier and the oscillator mass flow at the beginning, to find out the

5 Experiment

minimum flow required for a stable time signal and distinct peak in the corresponding spectrum. It is based on the observation of the instantaneous FFT calculated in the evaluation program used during the hot-wire measurement. It is further detailed in Section 5.1.3 (*Overall Operational Range*). After that, the amplifier flow is kept constant at that point and the oscillator flow is varied until maximum possible flow with a stable signal is achieved. The velocity measurement is taken for each 10 Hz increase of the frequency until maximum possible frequency with a stable signal is achieved. The previous steps are repeated for each 0.387 kg/h increase of the amplifier mass flow. After the measurement, an approximate operation range of the actuator is known. Moreover, the approximate mass flow required to increase the frequency for each 10 Hz increase is known. The carried steps are further summarized as follows:

Test 1

1. Iterations are performed for changing the amplifier and the oscillator mass flows.
Goals: To find the minimum flow required for a stable time signal and distinct peak in the corresponding spectrum.
2. The amplifier flow is kept constant at the minimum point and the oscillator flow is gradually increased for each increase of 10 Hz frequency until maximum possible frequency with a stable signal is achieved.
Goals: To find the operation range of the actuator for a constant amplifier mass flow and to approximate the mass flow required in the oscillator to increase 10 Hz frequency
3. The amplifier flow is increased by 0.387 kg/h and step 2. is repeated.
Goals: To find the operation range of the actuator for a new constant amplifier mass flow and to approximate the mass flow required in the oscillator to increase 10 Hz frequency at the new constant amplifier flow.
4. Step 3. is repeated until stable signal is achieved for maximum possible amplifier mass flow.
Goals: To find the overall operation range of the actuator.

With the information from the Test 1, a second set of measurements is taken: this time, however, the total mass flow is kept constant. The total mass flow of 1.37 kg/h is selected as a starting point. The oscillator mass flow is varied for each 10 Hz increase of the frequency, starting at a minimum flow. The amplifier mass flow is then adjusted accordingly to obtain a constant total mass flow and the measurements are taken. The same process is repeated for each increase of 0.387 kg/h total mass flow. This measurement aims to demonstrate the possibility of varying frequency at a constant total mass flow as well as the possibility of increasing the amplitude for the same frequency in the estimated operation range of the actuator. This is further summarized as follows:

Test 2

1. The total mass flow is kept constant at 1.37 kg/h. The oscillator flow is set to minimum and the amplifier flow is adjusted accordingly to maintain the constant total mass flow.
2. For the same total mass flow, the oscillator flow is gradually increased for each increase of 10 Hz and the amplifier flow is adjusted accordingly to maintain the constant total mass flow.
Goals: To demonstrate the possibility of changing frequency for the same amplitude.
3. The total mass flow is increased by 0.387 kg/h and step 2. is repeated.
Goals: To demonstrate the possibility of changing frequency for the same amplitude at a higher total mass flow.
4. Step 3. is repeated until maximum total mass flow in the estimated range is achieved.
Goals: To demonstrate the possibility of changing frequency for the same constant amplitude within the operation range of the actuator as well as to demonstrate the possibility of varying the amplitude of the actuation for the same frequency.

The measurements were carried out on all the four mentioned versions of the centerbodies. Unfortunately, the versions Z2.V4.1 and Z2.V4.2 did not offer stable signal for iterations of mass flow through the oscillator and the amplifier. The most probable reason could be the shortcoming of the manufacturing of the centerbody, as discussed in 4.7 (*Manufacturing of Actuator*). No measurements were taken for those versions of the centerbodies. The versions Z2.V2.1 and Z2.V2.2 demonstrated stable functioning, whose measurements were taken and assessed. The results of the assessment are discussed in detail in the following sections.

5.1.3 Results

Since, the actuator version Z2.V2.1 and its prototype Z2.V2.2 showed a stable functionality, velocity measurements are taken for those versions. For the version Z2.V2.1, both of the above mentioned sets of measurements are taken and for the version Z2.V2.2, measurements with only constant total mass flow are taken. The measurement of the velocity of the prototype Z2.V2.2 is intended to study the reproducibility of the functionality of the actuator Z2.V2. Similar measurements as carried out for the actuator Z2.V2.1 is repeated for the prototype Z2.V2.2. The results show discrepancy in the operating range compared to that of the actuator Z2.V2.1. However, within that operating range the desired functionality required for the control of the PVC is demonstrated. This discrepancy for the same geometry raised genuine concern, so CT images are made available. The images showed fault

5 Experiment

in the manufacturing of the centerbody exactly at the critical points of the internal geometry. Because of the manufacturing fault of this actuator, no reproducibility analysis could be performed. Due to the lack of scientific outcome, the results of the velocity measurement are not included in this work and the actuator is excluded from further investigation. The results of the measurement of the actuator Z2.V2.1 are presented in the following sections.

Overall Operational Range

The first goal of the measurement is to find the operational range of the used actuator (Z2.V2.1). For that, the oscillator and the amplifier mass flow are varied. Below 0.42 kg/h oscillator flow and 0.775 kg/h amplifier mass flow, neither a distinct peak in the spectrum nor a clear oscillation in the time signal can be observed. This operating conditions marks the lower end of the operational range of the actuator. The mentioned mass flows resulted in a frequency of around 100 Hz. The oscillator flow is gradually increased to increase the frequency and measured for each 10 Hz increase. At around 190 Hz the instantaneous calculation of the FFT as observed in the evaluation program, is found to be unstable. It is characterized by the rapid fluctuation of the peak frequency. Hence, no distinct peak frequency could be determined as the frequency of the oscillation. Moreover, the time signal does not show a clear oscillation. The previous steps are repeated for each 0.387 kg/h increase of the amplifier mass flow until the maximum limit of the flow for a stable signal is achieved. This delivers the operational range of the actuator, listed in the Table 5.1. Figure 5.4 helps to distinguish between a stable and an unstable signal. The top-left diagram shows the time signal for a relatively small flow in the oscillator and the amplifier. The signal reveals a nonuniform oscillation with a fluctuating peak velocity. This marginal stable oscillation is categorized as unstable in the study. The bottom-left diagram, where the oscillator flow is the same compared to the previous diagram but with twice the amplifier flow, shows a stable oscillation. Further decrease of the oscillator mass flow resulted in an unstable signal, as can be observed in the top-right diagram. The bottom-right diagram shows a very stable signal. Unfortunately, no measurements at the unstable regions for higher mass flow than that listed in the Table 5.1 is taken. Nevertheless, the time signal and the FFT as observed in the evaluation program in those regions demonstrated unstable signals.

Dependency of the Frequency to the Oscillator Flow

To observe the dependency of the frequency with respect to the oscillator mass flow, the estimated frequency and the supplied oscillator mass flow is plotted for different constant amplifier mass flows in Figure 5.5. The figure demonstrates linearity of the frequency to the oscillator mass flow. It can also be observed that a change of oscillator mass flow from ≈ 0.4 kg/h to ≈ 0.8 kg/h is required to increase the frequency from ≈ 100 Hz to ≈ 190 Hz. An important fact to be noticed is that the

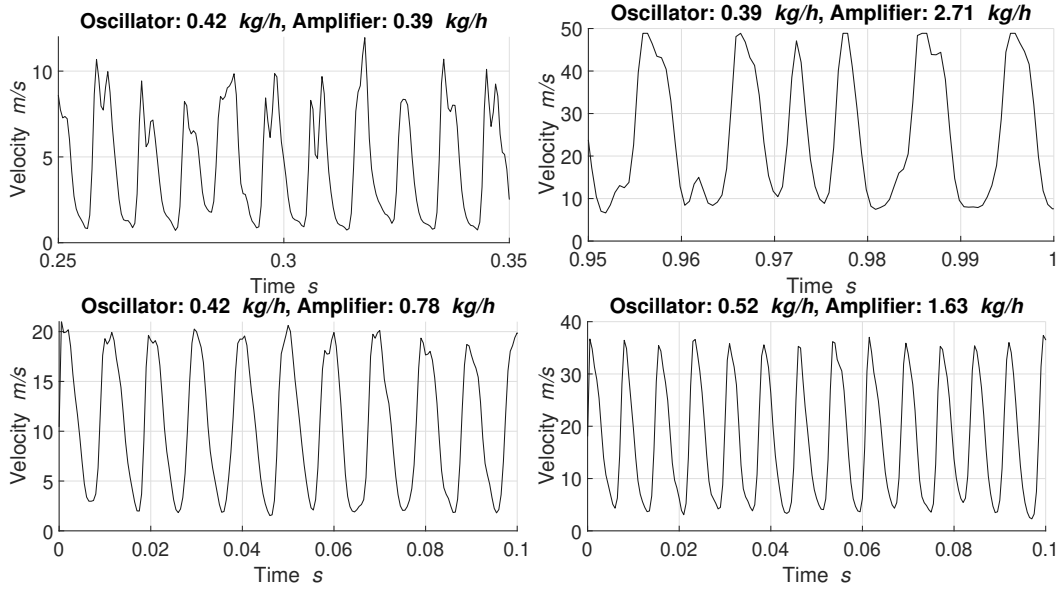


Figure 5.4: Characterization of the measured signal as stable or unstable. The upper diagrams show an unstable velocity signal and the lower diagrams show a stable velocity signal.

Table 5.1: Operational range of the actuator Z2.V2.1

Amplifier Mass Flow Range: $\approx 0.775 - 2.327 \text{ kg/h}$	
Oscillator Mass Flow Range: $\approx 0.4 - 0.8 \text{ kg/h}$	
Frequency Range:	
Amplifier Mass Flow kg/h	Frequency Hz
0.775	100 – 180
1.163	100 – 190
1.551	100 – 190
1.939	105 – 180
2.327	100 – 180
2.715	100 – 180

oscillator mass flow required to change the frequency is relatively smaller than the amplifier mass flow. Hence, while increasing the amplitude (almost proportional to the amplifier mass flow) for the same frequency, small tuning in the oscillator mass flow is required.

5 Experiment

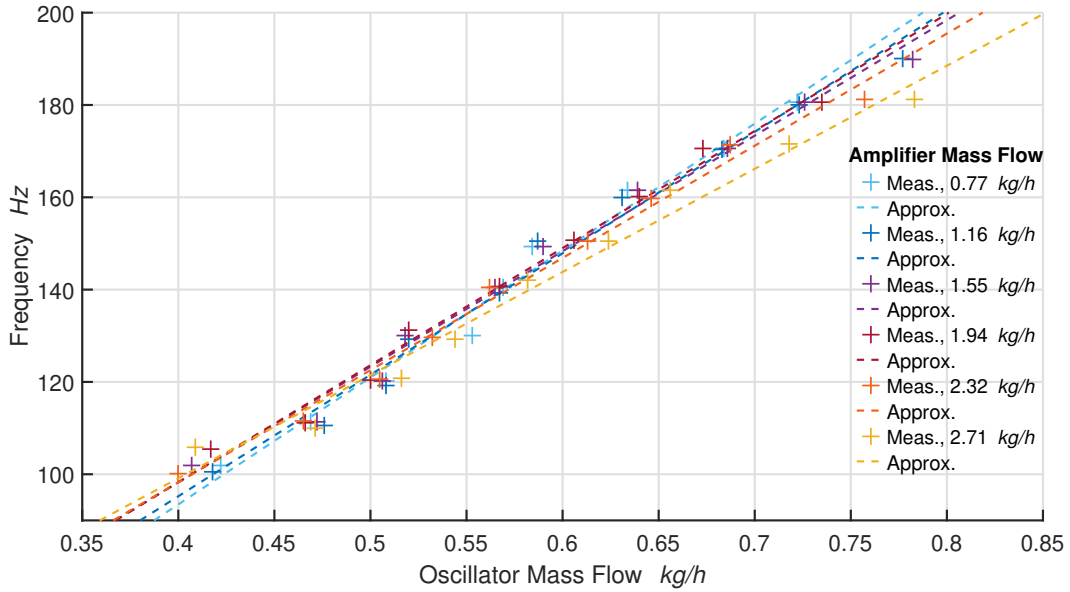


Figure 5.5: Change of frequency with respect to the variation of the oscillator mass flow for different constant amplifier mass flows in the actuator (Z2.V2.1).

Constant Total Mass Flow

Now that the approximate operational range of the actuator (Z2.V2.1) is known, in the subsequent experiment, the total mass flow in the oscillator and amplifier is kept constant. However, because of the limitation of the used rotameter, the total mass flow could only be kept constant in its first decimal place in the unit of kg/h with a small deviation in the second decimal place. The diagram 5.6 shows a constant frequency of ≈ 150 Hz for different total mass flows. The dotted lines represent effective velocity (RMS value). Both the effective velocity and the velocity itself show a continuous increase in the amplitude for an increasing total mass flow. The diagram also shows a desired switching property of the actuator. However, the minimum velocities of the individual velocity signals were expected to be zero or even negative, as a discrete outlet, when it is completely switched off, i.e., during the phases without any outflow. The pressure in the interaction region towards the inactive port decreases due to the entrainment of the surrounding fluid into the flow of the active outlet. This induced pressure gradient causes a counter flow in the inactive outlet. It can be argued that a simple hot-wire used for the measurement is not sensitive to the direction of the flow. So, it measures all the velocities perpendicular to the wire. Hence, the counter flow would be detected as a positive stream-wise component. However, the hot-wire is placed at a distance of 15 mm from the aperture of the outlet. It remains questionable if the counter flow is still detected at such a large distance. The other possibility is that the outflow bursts trigger an entrainment wake, which is still active during the phases without

active outflow. This induces an additional velocity in the direction of the flow. The registered velocity in the signal during the inactive phases is most probably the relative velocity of the flow between the counter flow (if any) and the stream-wise flow as a result of the entrainment triggered by the outflow bursts.

Although, the frequency of the oscillation could be varied for a constant total mass

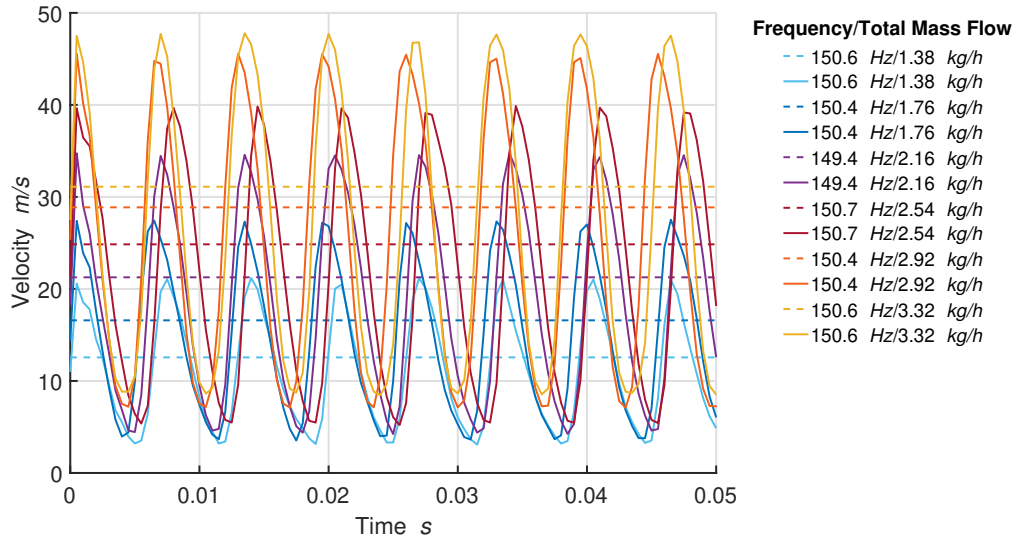


Figure 5.6: Approximately constant frequency for varying total mass flow in the actuator (Z2.V2.1). The dotted lines represent the RMS value of the time signal.

flow within the operational range of the actuator, it is essential to confirm that the amplitude of the signal also remains constant. In the Figure 5.7 the total mass flow is kept constant at ≈ 2.54 kg/h and the frequency is varied. The individual time signal is low-pass filtered at 400 Hz. The error in the setting of the total mass flow in this case is ± 0.025 kg/h. The key point to notice is that, the peak velocities of the velocity signals with different frequencies of oscillation are almost constant. The relative difference in the peak velocity is only 1.2 m/s. The RMS values of each of the velocity signals, shown by the dotted lines, are very close to each other. Similar results are observed in case of the other constant total mass flows. Table 5.2 summarizes the relative peak velocity difference for different constant total mass flows and the associated frequency range.

Figure 5.8 provides an overview of the operational range of the actuator (Z2.V2.1). The diagram on the left shows the variation of the frequency for the constant total mass flows. It demonstrates the possibility of keeping the total mass flow constant and yet changing the frequency of the switching within a certain frequency and total mass flow range. For the same total mass flow and frequency range, the diagram on the right shows the RMS values of the velocities. It quantifies the amplitude of the velocity signal. The diagram shows an increase of the amplitude with respect to the increase in the total mass flow. It can be observed in the diagram that for higher

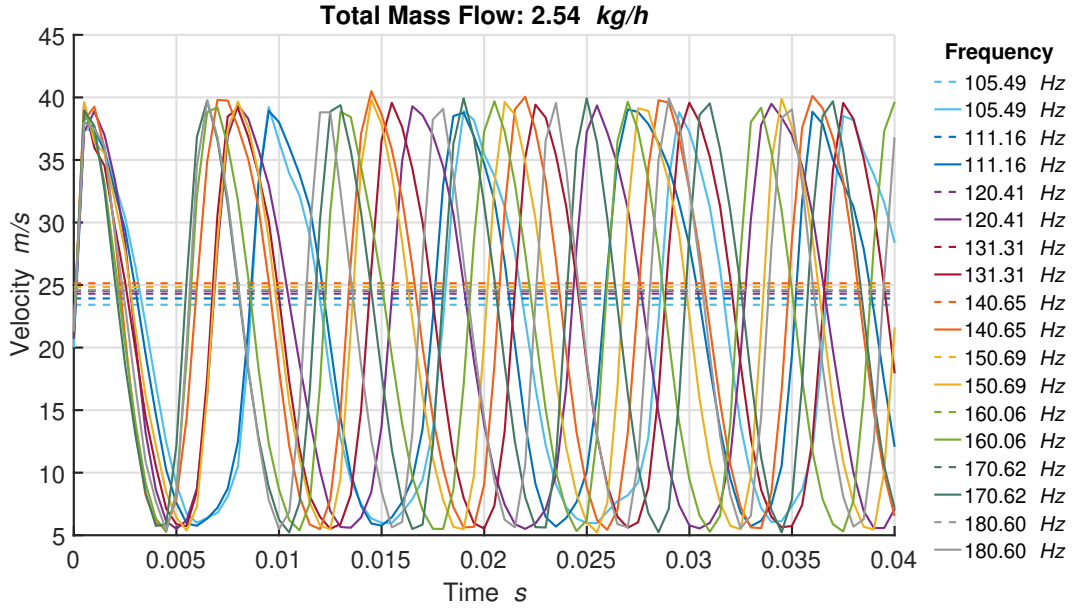


Figure 5.7: Variation of the frequency for a constant total mass flow of 2.54 kg/h. The dotted lines represent the RMS value of the time signal.

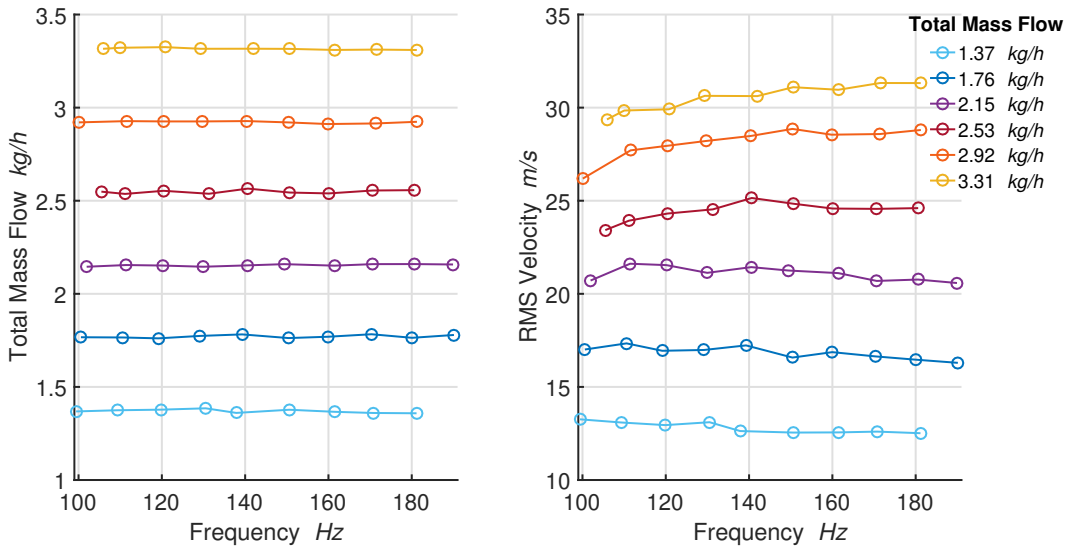
frequencies, the RMS velocity is slightly lower, except in case of 3.31 & 2.92 kg/h of the total mass flow. It is most probably associated with the higher loss due to the increased flow through the feedback channel of the oscillator. Since the frequency of the oscillation of the fluidic oscillator is directly proportional to the mass flow, the mass flow through the feedback channel is also higher for the increased oscillator mass flow. Nevertheless, the flow mechanism in the actuator is very complex. So, further investigations are essential to allow for further conclusions. However, this effect seems to diminish for higher amplifier mass flow. Another important aspect to notice is that, the RMS velocity is almost proportional to the total mass flow, except in case of 3.31 kg/h. Thorough analysis of the signal of 3.31 kg/h total mass flow shows that the measurement limit of the data acquisition, i.e., 10.5 V is reached, which forced the RMS value of the corresponding velocity signal to sink. This is directly mirrored in the low relative difference of the peak velocity for different frequencies (0.6 m/s) for the constant total mass flow of 3.31 kg/h, as seen in the Table 5.2. Nonetheless, the signal is still stable and it can be used in this range for the actuation of the PVC.

5.2 Comparison to the Simulation Results

Five different combinations of mass flow in the oscillator and the amplifier (Table 4.1) are used for the simulation for the total mass flow of 1.8 kg/h. The oscillator mass flow is varied between 0.54 & 1.26 kg/h resulting in frequencies between 93 & 199 Hz

Table 5.2: Relative difference in the peak velocity for different constant total mass flow in the actuator (Z2.V2.1) including the frequency range.

Total Mass Flow kg/h	Frequency Hz	rel. Peak Velocity Difference m/s
1.375	100 – 180	1.2
1.763	100 – 190	1.2
2.151	100 – 190	1.5
2.539	105 – 180	1.2
2.927	100 – 180	1.7
3.315	105 – 180	0.6

**Figure 5.8: Operational range of the used fluidic actuator (Z2.V2.1). The diagram shows the distribution of frequencies for different total mass flow (left) and the calculated RMS velocity (right).**

for a total mass flow of 1.8 kg/h. However, in the velocity measurement using hot-wire measurement technique the oscillator mass flow between 0.4 & 0.8 kg/h resulted in frequencies between 100 & 190 Hz for almost the same total mass flow. Table 5.3 shows the comparison of the simulation and the velocity measurement at three oscillator mass flows for the same total mass flow in each case. The frequencies in the velocity measurements are clearly higher than the simulation results, although the mass flow is almost the same in each case. One of the reasons for this discrepancy in the results must be due to the reduced effective geometry of the actuator, as discussed in section 4.6. Furthermore, the simulation is only performed in 2D for an incompressible air and does not represent the overall flow phenomena, which include 3D effects like wall effects and secondary flows within the rectangular and curved channels of the actuator. Nonetheless, the functionality aspect of the actuator is

5 Experiment

crucial. In both of the cases, an excellent switching characteristic is shown, the frequency changes almost linearly to the oscillator mass flow and an independent adjustment of the frequency and the amplitude is demonstrated by adjusting the amount of the flow through the oscillator and the amplifier.

Table 5.3: Comparison of the results obtained from the velocity measurements using a hot-wire to the results of the estimated velocity obtained from the simulation of the flow.

Simulation			Velocity Measurement		
Osci. <i>kg/h</i>	Total <i>kg/h</i>	Freq. <i>Hz</i>	Osci. <i>kg/h</i>	Total <i>kg/h</i>	Freq. <i>Hz</i>
0.5	1.8	93	0.5	1.8	120
0.7	1.8	128	0.7	1.8	170
0.9	1.8	148	0.8	1.8	190

5.3 Visualization of the Flow

To verify the digital switching characteristics and complement the results of the hot-wire velocity measurement of the actuator, Schlieren imaging of the outlet flow is performed. Schlieren imaging is a method to visualize density variations utilizing the refraction of the light to produce focused optical images of a transparent media. A mirror co-limits the light coming from a point source and passes through the test area consisting of the transparent media with density variations. This causes a density based refraction of the light, causing it to curve. This follows a refocusing of the light rays using an another mirror. A knife-edge partially obscures the light to the camera which bends the most and allows to pass those which do not bend as much, thereby producing regions of varying light intensity. The darker regions correspond to a higher refraction associated to the higher density. Settles [55] has presented a detailed information about the Schlieren technique.

For this work, the Schlieren images are acquired using a Toepler Z-Type Schlieren system. The images of the flow motion illuminated with a pulsed LED light with an exposure time of $1 \mu\text{s}$ are captured using a Photron FASTCAM SA-Z2100K. The images are taken at 20,000 frames per second with a camera shutter time of $1/630000$ s. The mirrors used for the Schlieren imaging have a focal length of 1219 mm. A horizontal knife blade cut-off is used to obtain images of the vertical density gradient ($\partial\rho/\partial y$). To increase the density gradient, helium is mixed with air. The amplifier of the actuator is supplied with air, whereas the oscillator is supplied with helium.

The Schlieren images for the present work are taken with a pre-installed setup at the HFI of the TU Berlin with assistance of a Schlieren method expert. Figure 5.9 illustrates the imaging setup used here.

The obtained Schlieren images validate the switching characteristics of the actuator.

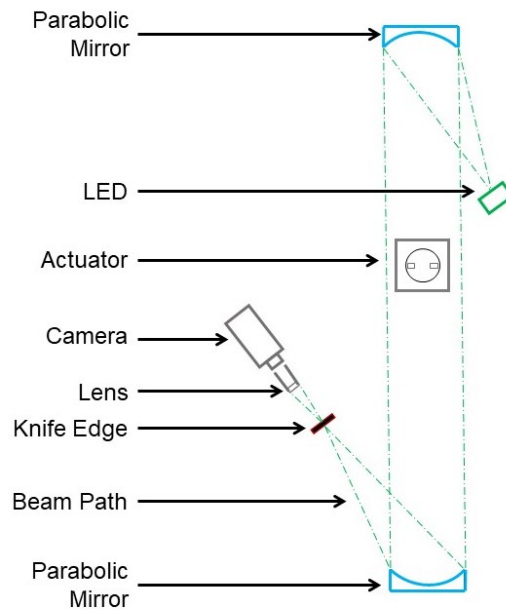


Figure 5.9: Measurement setup of the Schlieren imaging.

Figure 5.10 illustrates the results of the Schlieren imaging. The development of the pulse on the left and the right side of the actuator is demonstrated with vertically arranged images. The red guide arrows intend to distinguish the instantaneous pulse from the diffused air. The top images show the beginning of the pulse at the point of switching on the left and the right side respectively. The bottom images show the pulse at the point just switched to the other side. The middle images show the development of the pulse halfway.

5.4 Differential Pressure Measurement

This experiment intends to test the actuation concept used with the aid of differential pressure sensors in a model combustion chamber. The spectral frequency and amplitude at which the PVC and the actuator oscillate can be assessed from the spectrum of the signals calculated from the time signals obtained from the pressure sensors. The spectrum shows whether the influence of the actuator leads to a change in the PVC frequency and amplitude and if lock-in is achieved.

5.4.1 Experimental Setup

The experimental setup for the differential pressure measurement is sketched in Figure 5.11. A section through the generic swirl-stabilized combustor test-rig is presented on the left side of the diagram. It consists of a pipe as a flow channel with a

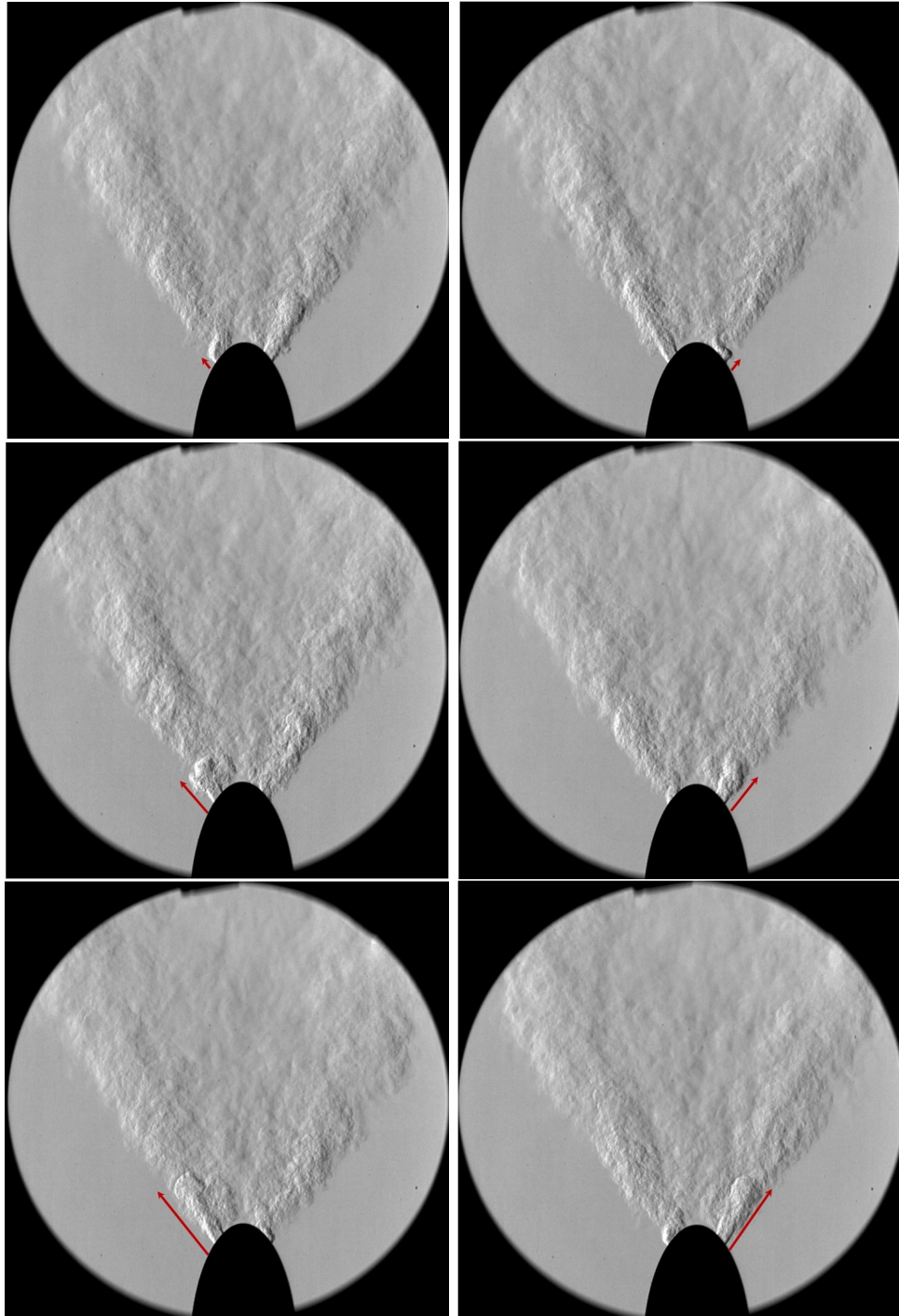


Figure 5.10: Schlieren images of the flow out of the actuator. The red guide arrows help distinguish the pulse from the diffused air.

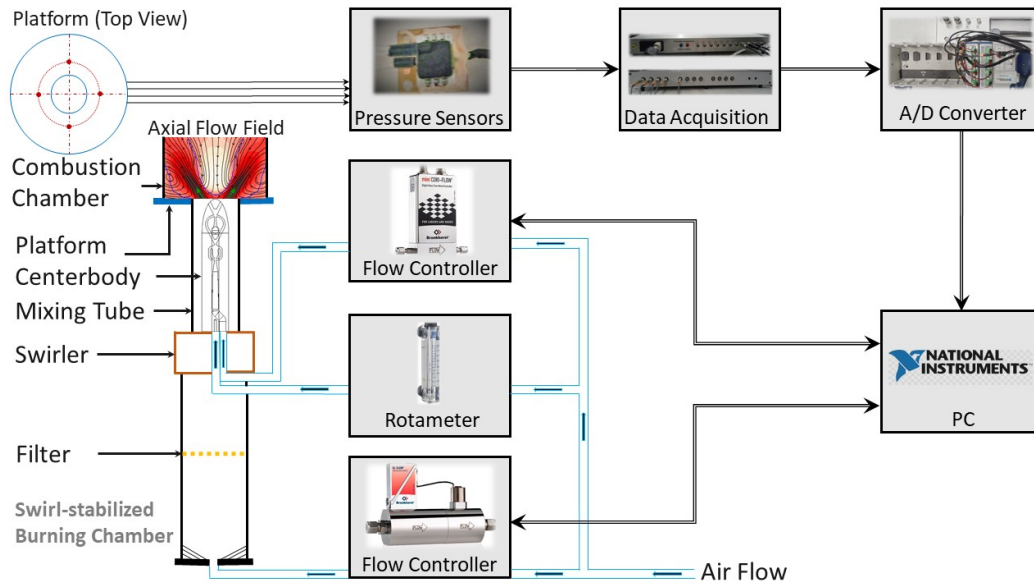


Figure 5.11: Measurement setup for the differential pressure measurements.

circular cross-section, a honeycomb filter to stabilize the inlet flow, a swirl generator, a circular mixing zone with a centerbody and a confined combustion chamber, which is open to the atmosphere.

The main flow to the main pipe of the generic swirl-stabilized combustor test-rig is supplied through a pipe line from the pressurized air reservoir. The reservoir is connected to a digital mass flow controller, which can be directly controlled using the lab computer. A air mass flow up to 100 kg/h can be adjusted with the controller. The oscillation frequency of the PVC is regulated by the amount of the mass flow. In the main pipe, the flow is expanded in a diffuser and homogenized with a honeycomb filter and transferred to a swirl generator. It generates a radial swirl on the flow. The swirl generator consists of movable blocks, with which swirl numbers between 0 and 1.5 can be set. In this work, a swirl number of $S = 0.7$ is used.

After passing the swirl generator, the flow passes through the mixing tube into the combustion chamber. In the mixing tube a centerbody is fixed on the upper surface of the swirl generator, such that the air flows with a rotating motion around the centerbody. The combustion chamber consists of a circular plastic platform on which rows of miniature holes for the pressure measurement are arranged. A cylindrical glass cover is placed on the platform, which protects the main flow from external disturbances.

The centerbody in the mixing zone is supplied with air via a separate pressurized air line. The incoming air is divided into two lines and connected to a rotameter and a mini flow controller, respectively. The outlets from the rotameter and the flow controller are passed through holes placed on the wall of the main pipe and then

5 Experiment

through the base of the swirl generator to the inlets of the centerbody. The rotameter with a measurement range of 4 – 50 l/min of air is used to manually control the mass flow of the amplifier of the actuator. The amplifier is supplied with air flow at 2.5 bar. The flow controller of type *mini Cori-Flow M14* is used to control the flow through the oscillator of the actuator. It has a measurement range of 0.03 – 1 kg/h with a precision of ± 0.5 % of the measurement value. The flow controller is supplied with 3.5 bar air.

The experimental setup is constructed to measure the differential pressure at the platform and in the mixing tube of the combustion chamber. For that, rows of miniature holes are integrated on the platform and the walls of the mixing tube. The red marks in the top view of the platform, as shown in the Figure 5.11, represent the locations at which the pressure is measured for this study. The four pressure hoses arranged concentrically lead to four miniature differential pressure sensors of type *First Sensor HDOM010*. The sensors have a measuring range of 1000 Pa and can be used to measure pressure fluctuations up to 0.1 Pa. A differential pressure sensor has two ports: one for the total pressure and another for the static pressure. The sensors are connected to a static pressure source by means of an ambient pressure plenum. The measured pressure difference corresponds to the dynamic pressure. The analog signals of the sensors are amplified and converted to digital signals with a 16-bit A/D converter of type NI 9188. The sample frequency of 8192 Hz is used. The digital signal is finally recorded and processed using a measuring computer.

5.4.2 Measurement

With the new concept of oscillator-amplifier combination, the frequency and the amplitude of the used actuation unit can be adjusted independently. As already validated, the amplitude of the oscillation can be increased by increasing the total mass flow through the oscillator and the amplifier. At the same time, the frequency of the oscillation can be altered primarily by means of the flow through the oscillator. This art of control technique makes it easy to study the lock-in behavior of a coupled system. The procedure is to set the actuation frequency close to the natural frequency of the PVC and gradually increase the amplitude of the actuation. At a certain amplitude, the lock-in state occurs and is referred to as the lock-in amplitude. In this manner, for different frequencies close to the natural frequency of the PVC, corresponding lock-in amplitudes can be determined and is used to obtain information about the coupled system.

Before the measurement is started, the ambient conditions are recorded, which are listed in the following table.

Room Temperature	22°C
Air Pressure	9950 Pa
Relative Humidity	50 %

The used swirl-stabilized combustion chamber is operated at a swirl number of $S = 0.7$ and the mass flow can be varied up to 100 kg/h. Figure 5.12a shows the

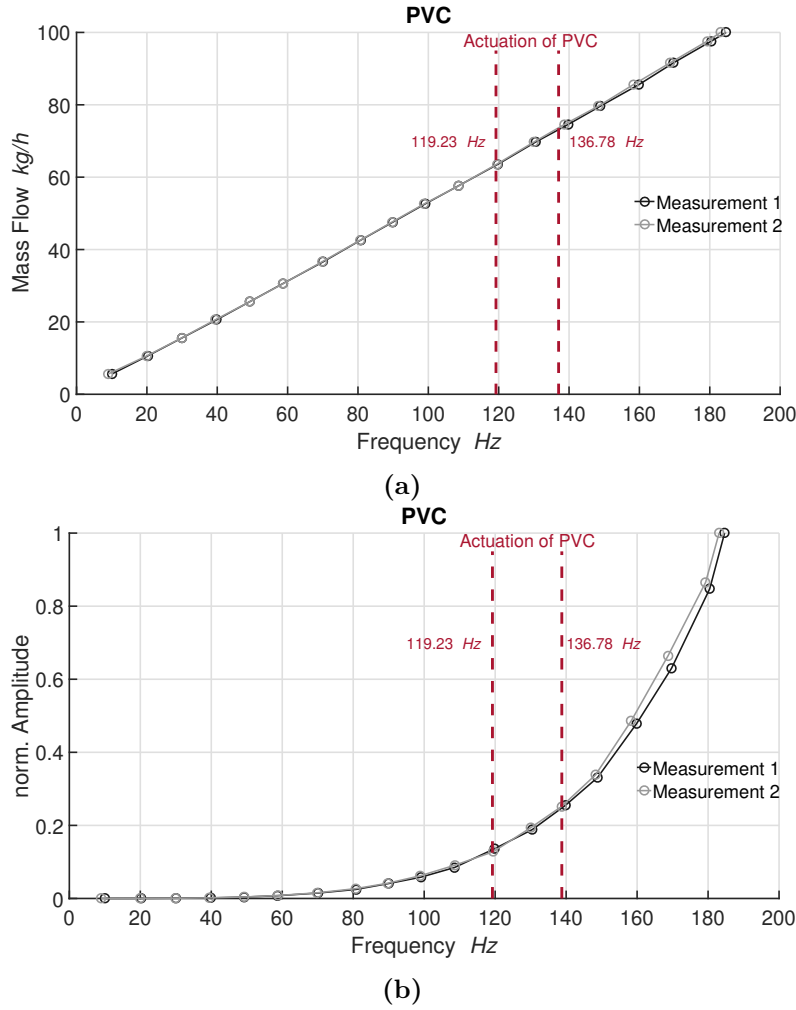


Figure 5.12: Frequency range of the PVC in the used swirl-stabilized combustion chamber at a swirl number $S = 0.7$ up to a mass flow of 100 kg/h. The dotted red lines represent the location at which the PVC is actuated. (a) Shows the variation of the frequency of the PVC with respect to the mass flow through the combustion chamber and (b) shows the normed amplitude of the spectrum of the PVC at different frequencies.

linear relationship between the frequency and the mass flow through the combustion chamber. Two sets of differential pressure measurements are carried out for the evaluation. The measurements show reproducibility of the evaluation with a very negligible difference in the frequencies, especially at higher frequencies. Similarly, Figure 5.12b shows parabolic distribution of the amplitude of the PVC at different frequencies. The dotted lines in both of the diagrams represent the location of the frequencies at which the PVC is actuated in the study.

In this study, the PVC is actuated at two different frequencies: $f_{PVC} = 136.78$

5 Experiment

and 119.23 Hz with different actuation frequencies ranging at $\pm 10\%$ of the PVC frequency. The first step is to turn on the main mass flow and regulate it such that the desired PVC frequency is obtained. Then the measurement is taken. After that, the main flow is shut down and the control flow in the oscillator and the amplifier are turned on. By manually controlling the mass flow in the amplifier port by means of a rotameter and in the oscillator by means of a flow controller, the desired actuation frequency and amplitude is specified. A measurement is then taken. After that, both the predefined main flow and actuation flow are simultaneously opened and a measurement is taken. These steps are repeated for step-wise increase of the total mass flow through the actuator and for the corresponding mass flow required for the mentioned PVC frequencies.

The aim of the above measurements is to determine the behaviour of the PVC for different actuation frequencies and amplitudes. To estimate it, the PSD of the first azimuthal mode $m = 1$ of the Fourier decomposed differential pressure signal is calculated. In this manner, the independent frequency and amplitude of the PVC, the actuator and at the state of the actuation of the PVC could be determined. At the state of the actuation, if the actuation amplitude is high enough, the PSD shows a peak only at around the actuation frequency. In that case, frequency lock-in has been established. Figure 5.13 shows small sections of the time signals, which are Fourier decomposed and their PSDs for the above mentioned three states of the measurement. The top diagrams show the time signal (left) and the corresponding spectrum of the PVC signal (right) without the actuation. Similarly, the middle diagrams show that of the actuation signal and the bottom diagrams show that of the actuated PVC.

An important aspect to note from the time signal and the spectrum is that the magnitude of the actuation is smaller by a factor of 100 than that of the main flow including the PVC. In the corresponding spectra to the respective time signals, the gray lines represent the PSD without averaging and the red lines represent the PSD after Welch-averaging. The differential pressure signal measured for 40 s with a sampling rate of 8192 samples/s is averaged using a Welch-averaging with a total of 23 Hanning windows. The averaging is necessary for a reliable comparison of the spectrum for lock-in behaviour.

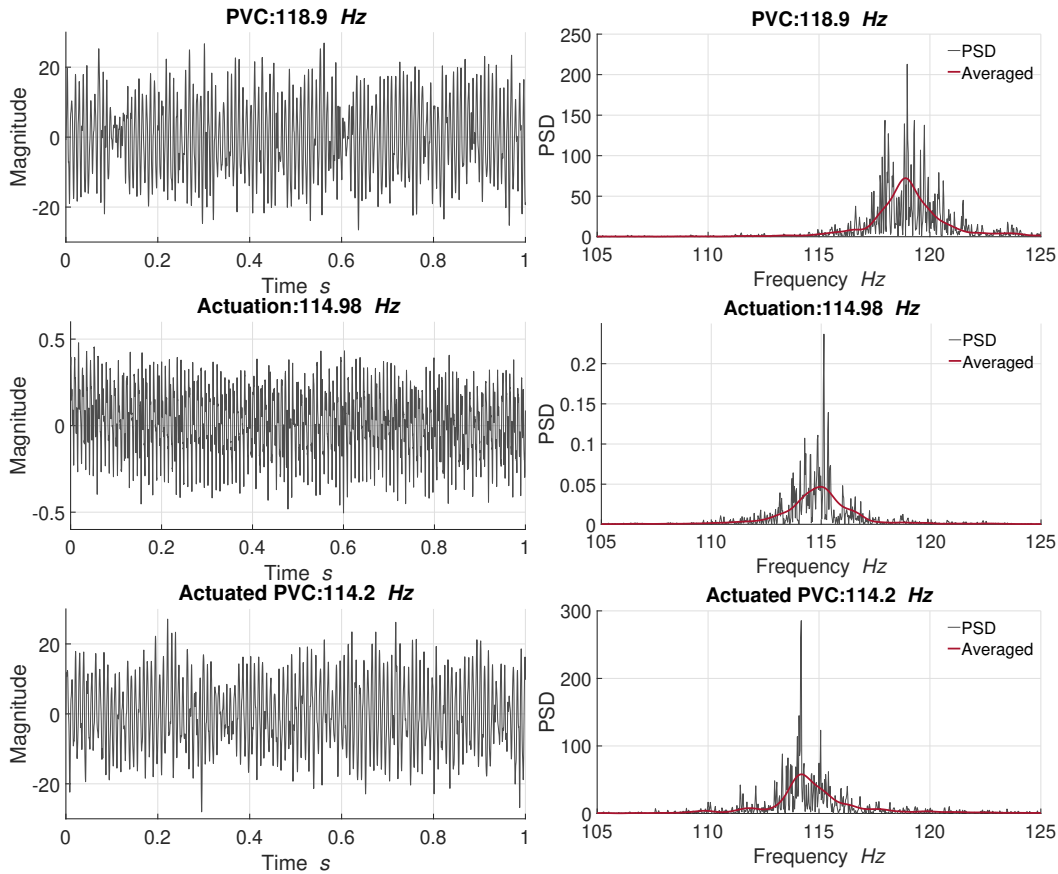


Figure 5.13: Time signals and spectra. The top diagrams show the time signal (left) and spectrum of the PVC signal (right) without the actuation. Similarly, the middle diagrams show that of the actuation signal and the bottom diagrams show that of the actuated PVC. The time signals show relatively lower magnitude of the actuation compared to the other signals. The red lines in the spectrum show the averaged spectrum of the respective PSD.

5.4.3 Results

The assessment of the behaviour of the PVC for the actuation with different frequencies and magnitudes demonstrated three different types of reactions. The first type of reaction is the lock-in of the frequency as well as the phase and the amplitude. It means that the PVC meanders with the same frequency and phase as that of the actuation and the magnitude is almost equal to the amplitude of the PVC without actuation. The second type of reaction is that the PVC endures the actuation frequency, however the magnitude is considerably reduced. The final type of reaction is the shifting of the frequency. The shifting, however, can be towards the actuation frequency or away from the actuation frequency. Since, the actuated signal does

5 Experiment

not have the exact frequency as that of the actuation and it also does not have the exact PVC amplitude without actuation at the lock-in state, it is necessary to draw a clear margin of the frequency and the magnitude for the assessment of all the measurements. For the same reason, the behaviour of the PVC is classified into three groups:

- **Lock-In:** $\frac{|f_A - f_{PVC\&A}|}{|f_{PVC}|} \leq 0.01 |f_{PVC}|$ & $A_{PVC\&A} \geq 0.5 A_{PVC}$
- **Damping:** $\frac{|f_A - f_{PVC\&A}|}{|f_{PVC}|} \leq 0.01 |f_{PVC}|$ & $A_{PVC\&A} < 0.5 A_{PVC}$
- **Shifting:** $\frac{|f_A - f_{PVC\&A}|}{|f_{PVC}|} > 0.01 |f_{PVC}|$.

Where, f and A represents the frequency and the amplitude, respectively. The indices PVC , A and $PVC\&A$ represent the PVC signal without actuation, the actuation signal and the PVC signal with actuation, respectively. The mentioned margins are reasonable taking into account the associated systematic errors and the averaging errors. The assumption, that the magnitude of the spectrum for a constant actuator total mass flow should be nearly constant, is used to determine the number of windows to be used for the averaging. For that, the measurement data for the constant total mass flow at different frequencies are averaged with a certain number of windowing, which results in an almost equal magnitude. The window number of 50 using a Hanning window is found to be suitable by maintaining still the accuracy of the frequency. Figure 5.14 shows the spectra of actuator signals obtained from the constant total mass of 2.15 kg/h with and without averaging. The upper spectra without averaging show a discrepancy in the magnitude, although a constant magnitude is expected, as the total mass flow in the actuator is constant. After the averaging, as can be seen in the lower diagram, the magnitude of the individual spectrum is almost constant. The frequency yet shows only a small disparity to those spectrum without averaging. The mentioned window number is used for the study of the behaviour of the PVC at all the operating conditions.

After setting the criteria for the assessment of the reaction of the PVC to different actuation and fixing a suitable window size for the averaging, all of the measured signals are evaluated. Figure 5.15 illustrates the reaction of the PVC for different actuation. In the Figure 5.15a, the actuated PVC takes the frequency of the actuation and the magnitude is relatively high. It is therefore classified as lock-in. Similarly, in the Figure 5.15b the actuated PVC takes the frequency of the actuation, however, the magnitude is relatively small. Hence, it is classified as damping. The rest of the Figures 5.15c and 5.15d illustrate the shifting of the PVC after the actuation, whereby, the Figure 5.15c shows the pulling effect towards the actuation and the Figure 5.15d shows the pushing effect away from the actuation.

For the lock-in not only the synchronization of the frequency of the actuated signal to the actuation signal is necessary, but also the actuated signal should retain the phase of the PVC without the actuation [14]. To analyse the phase characteristics, phase angles of the respective signals are calculated and the absolute difference in the phase angles are compared. The phase angle is calculated by unwrapping the phase

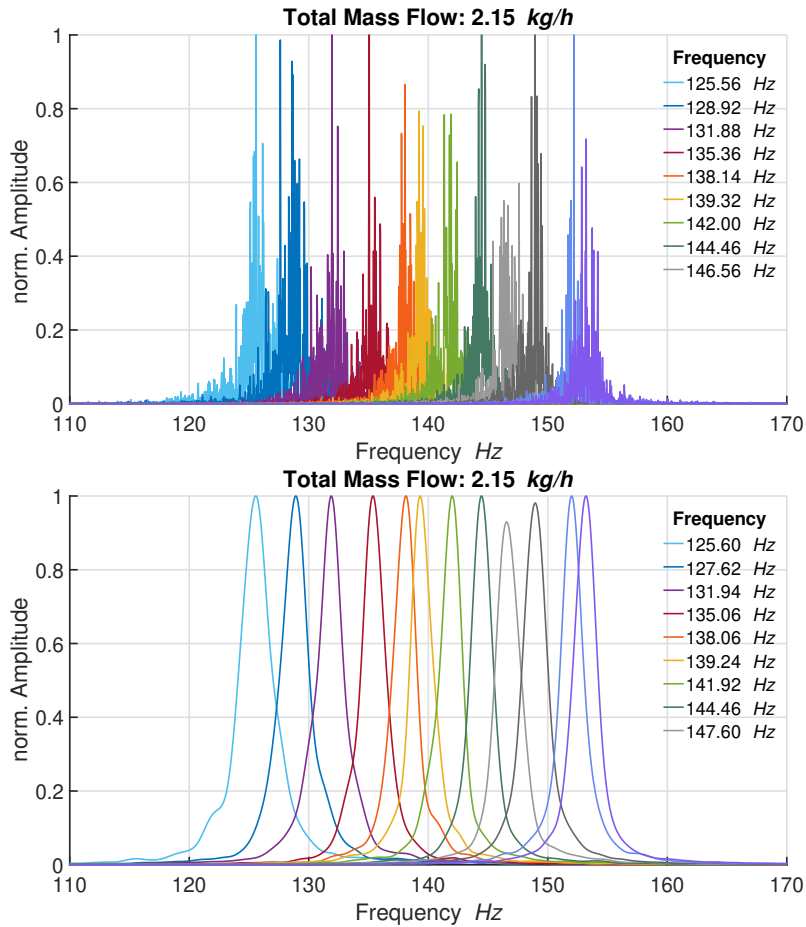


Figure 5.14: Spectra with and without averaging. The averaged spectra demonstrate fast equal amplitude yet sustaining the frequency compared to the unaveraged spectra.

angles at the jump between the consecutive angles that is greater than or equal to π radians. The angles are shifted by adding multiples of $\pm 2\pi$ until the leap is less than π . The MATLAB function *unwrap()* is used to unwrap the phase angle. Figure 5.16 shows the phase difference of the PVC with and without the actuation for two cases: the lock-in and the shifting. In case of the lock-in, the phase difference between the two signals of the PVC with and without the actuation is very small, as shown in the Figure 5.16a. In the case of shifting, however, the phase difference increases steadily.

Overall Analysis of the Reaction of the PVC

In this manner, the reaction of the PVC for above mentioned range of different actuation is assessed. Figure 5.18 summarizes the reaction of the PVC at a frequency

5 Experiment

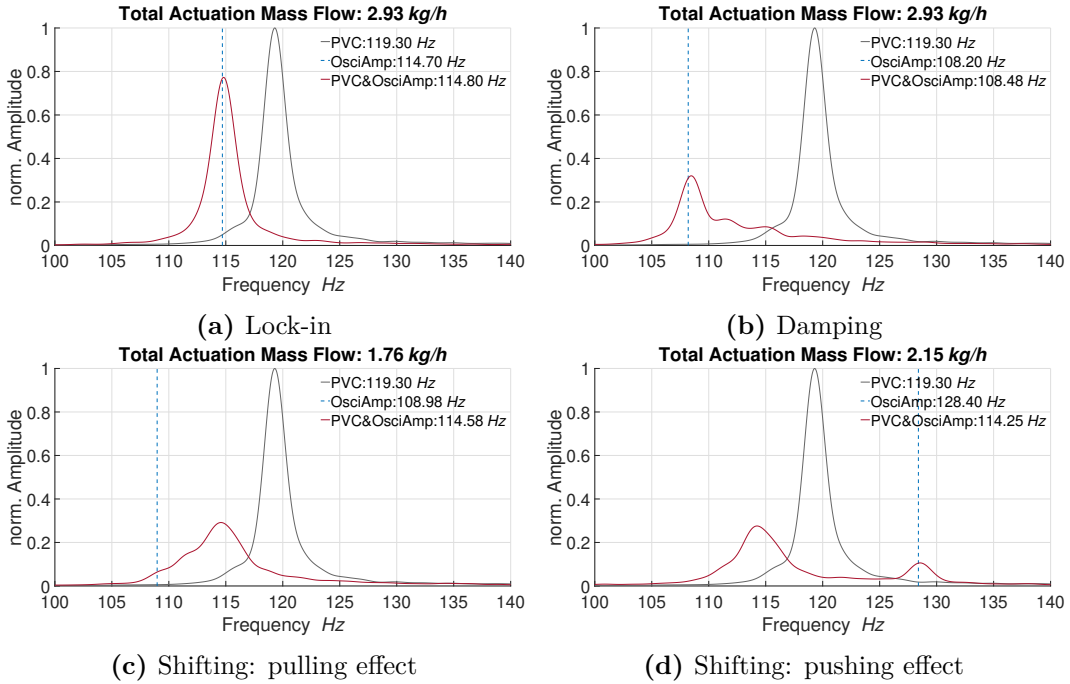


Figure 5.15: Different reactions of the PVC to the actuation. The dotted blue lines represent the frequency of the actuation.

of 136.78 Hz for different actuation frequencies and amplitudes. The ordinate shows the total actuation mass flow, representing the magnitude of the actuation and the abscissa shows the normed actuation frequency relative to the PVC frequency. The green full circles represent the lock-in at the point of actuation and the hollow green circles represent the damping reaction of the PVC to the actuation. A V-form distribution of the lock-in and damping combined with few exceptions can be seen in the figure. This region is demarcated by dotted green lines. The hollow yellow circles represent the shifting of the frequency. The diagram demonstrates that, by increasing sufficient actuation magnitude (actuation mass flow) lock-in can be achieved. For increasing relative difference of the actuation frequency from the PVC frequency, a higher actuation magnitude is required.

This V-form distribution confirms with the study of Li & Juniper [14]. In the study of Li & Juniper, experimental investigation is performed for a range of phase dynamics of a periodically self-excited low-density jet. Figure 5.17 shows the synchronization diagram obtained from the analysis in the study. The diagram (a) shows the synchronization diagram demarcating regions of drifting (shifting) (A), lock-in (B) and phase trapping (C, gray regions). The diagrams (b) & (c) show the phase difference for two different forcing frequencies: close to the natural frequency ($f_f/f_n \approx 1.04$) and far from it ($f_f/f_n \approx 1.12$). The phase trapping is characterized by a partially synchronous state of frequency locking, however, without phase locking. This is especially found for a forcing frequency far from the natural frequency and for higher

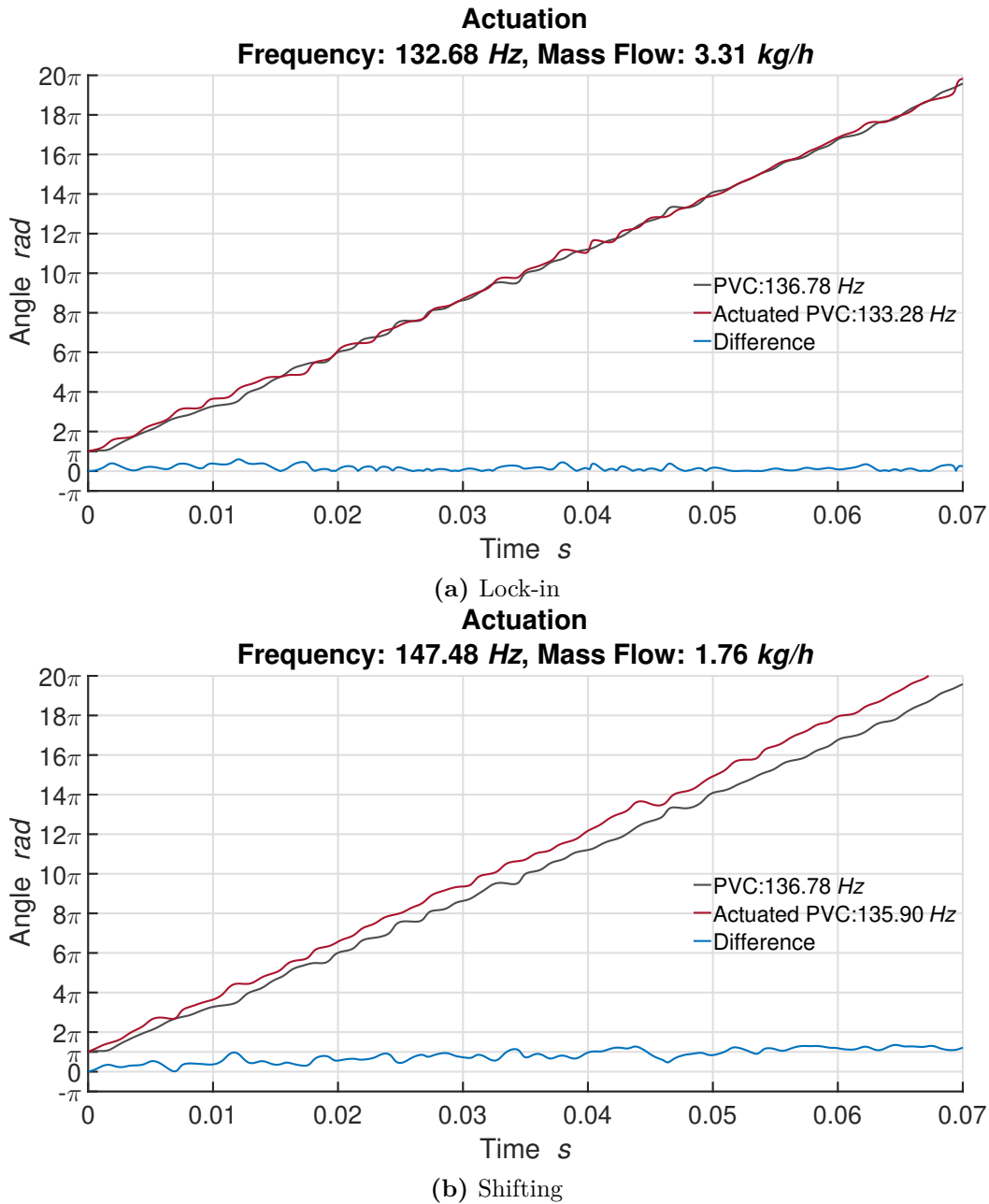


Figure 5.16: Phase difference of the PVC with and without the actuation. The upper diagram shows a constant phase difference at lock-in. The lower diagram shows the steady increase of the phase difference in case of the shifting.

forcing amplitude.

Similarly from the observation of both of the studies, it is found that lock-in seems

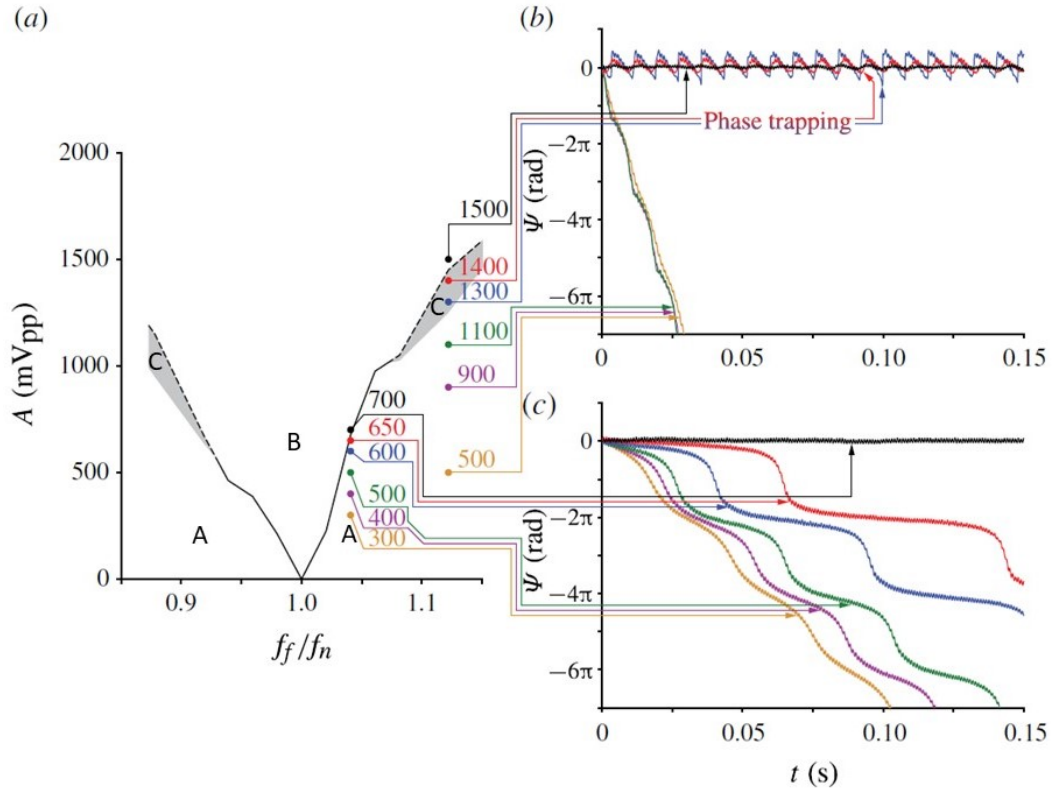


Figure 5.17: Amplitude and phase response of the forced low-density jet. (a) Synchronization diagram demarcating regions of drifting (A), lock-in (B) and phase trapping (C, gray region). (b) & (c) show the phase difference for two different forcing frequencies: close to the natural frequency ($f_f/f_n \approx 1.04$) and far from it ($f_f/f_n \approx 1.12$). [14]

to be difficult to achieve for higher actuation frequencies than the PVC frequency. Important aspect to notice from the overall analysis is that, lock-in region extends up to $\approx \pm 8\%$ of the PVC frequency with the used actuator in its operational range.

Similarly, the reaction of the PVC at 119.23 Hz for different actuation frequencies and amplitudes are assessed and presented in Figure 5.19. There is still a V-form recognizable, however, it is shifted towards lower frequencies than the natural PVC frequency. This shift can be associated with lower amplitudes of the PVC for smaller frequencies (see Figure 5.12b). It is known that the critical forcing amplitude for lock-in increases with the strength of the self-excited instability and the deviation of the forcing frequency from the natural frequency [56]. It is valid that for the corresponding low PVC amplitude, the critical lock-in amplitude is also smaller. However, further investigation is necessary for such a conclusion. For the natural frequency of the PVC at 119.23 Hz the lock-in is limited below the PVC frequency.

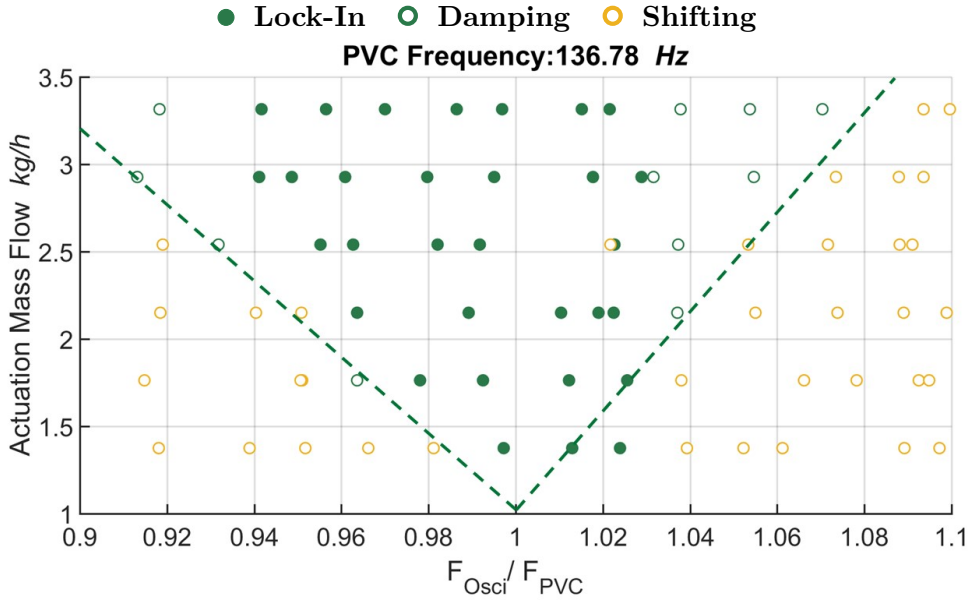


Figure 5.18: Summary of the reaction of the PVC at 136.78 Hz to different actuations. The dotted green lines demarcate the lock-in region from the shifting region.

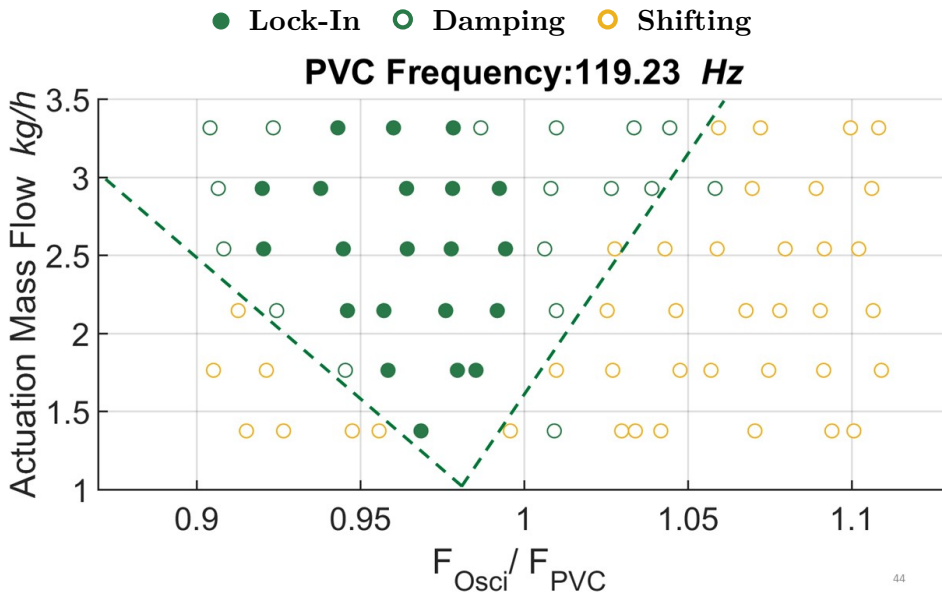


Figure 5.19: Summary of the reaction of the PVC at 119.23 Hz to different actuations. The dotted green lines demarcate the lock-in region from the shifting region.

Conclusion

From the experimental investigation of the PVC dynamics to the actuation using the designed actuator it can be concluded that the PVC reacts with three distinct responses: lock-in, damping and shifting. The actuation in the vicinity of the PVC frequency demonstrate the lock-in when excited with enough amplitude. The actuation further away require increased amplitude for the lock-in. At insufficient amplitude, the PVC is shifted such that, for the actuation frequencies smaller than that of the PVC, a frequency pulling effect is observed and for higher frequency, a frequency pushing effect is observed. In the transition between the shifting and the lock-in, damping is noticed. Furthermore, the lock-in region is wider for the actuation frequencies smaller than the PVC frequency. In addition to that, an assymetrical V-form distribution of the response of a hydrodynamic instability, as seen in the study of Li & Juniper [14] is further confirmed by this study. The designed actuator demonstrated the possibility of the lock-in up to $\approx \pm 8\%$ of the PVC frequency.

6 Summary

The present work aimed on combining the technology of fluidics with elegantly solving the current complex problem of controlling the global hydrodynamic instability, the precessing vortex core, usually found in the modern swirl-stabilized combustor. Due to the robustness to harsh environment found in the combustion chamber, no moving parts and yet the possibility to oscillate the fluid at desired frequency, make fluidics ideal to be used for actuation. The preceding study employed feedback type of fluidic oscillator for the actuation. Although, the actuation concept served its purpose, lack of independent control of the frequency and the amplitude limited the full potentiality of the actuation. The independent control of the frequency and the amplitude is not possible using a simple fluidic oscillator because of the linear dependency on the supply mass flow. To solve this issue, the objective of this work was to design a fluidic oscillator that can regulate the frequency and the amplitude of the actuation independently.

During the course of this work, a fluidic actuator combining a feedback type of fluidic oscillator and a bistable fluidic amplifier was designed, simulated, optimised and finally integrated in the centerbody of a swirl-stabilized combustor. The combination of the oscillator and the amplifier was designed based on the master-slave concept, such that the frequency generator, the oscillator, provides frequency information and the amplifier takes this information and passes it to an increased mass flow. This should not only boost the total actuator outlet mass flow, but also maintain the frequency range of the oscillator. The frequency and the amplitude of the actuation should be able to be regulated by the combination of the oscillator and the amplifier mass flow. This potential of the actuator is validated through simulations of the flow within the actuator, velocity measurement of the outlet flow through the actuator using hot-wire measurement technique and the flow visualization of the outlet flow by means of Schlieren imaging technique.

The oscillator, that successfully demonstrated the control of the PVC in the preceding study, was taken for the design of the actuator. It was, however, scaled down to remain in the same mass flow range and also to incorporate it in the limited space of the centerbody, which required to include the amplifier as well. The amplifier was designed as a compromise between the two extreme designs: a low gain but stable system and a high gain system that tends to oscillate. The individual designs were then connected together with the two output arms of the oscillator connected to the two control ports of the amplifier. The flow within the resulting design of the actuator was then simulated. The 2D simulations of the flow was performed solving Reynolds-averaged Navier-Stokes equation (RANS) for incompressible air at 1 atm. The assessment of the simulation of the flow demonstrated positive results. The flow

6 Summary

animation showed excellent switching characteristics, except for some undesired excess flow of air into the inactive output port of the oscillator. The pressure gradients were negligible and the assessment of the velocity at the output port of the actuator showed excellent switching, desired for the actuation. The simulation for different oscillator and amplifier mass flows, however, for total mass flow kept constant, demonstrated the possibility of changing the frequency by simply adjusting the amount of the flow through the oscillator and the amplifier. However, the switching characteristics in the velocity signal was only satisfactory for smaller oscillator mass flows. The frequency showed linear dependency to the oscillator mass flow.

The design of the actuator was further optimised by varying different geometrical aspects. Four different designs were simulated and the two best designs (Z2.V2 and Z2.V4) were integrated in the 3D centerbody. Each design is printed two times for reproducibility evaluation. The Computer tomography (CT) images of the model Z2.V2.1 and Z2.V2.2 were made available. The CT images of the model Z2.V2.1 showed sufficient geometric representation of the CAD model. Unfortunately, the model Z2.V2.2 had fault in the manufacturing.

To validate the results of the simulation, the two centerbody designs (Z2.V2 and Z2.V4) were subjected to the velocity measurements at the outlet using hot-wire measurement. For the model Z2.V4 the velocity measurement showed undesired functionality. The most plausible explanation is a defective manufacturing of the internal structures. No further investigation was performed on the centerbody Z2.V4. The velocity measurement of the model Z2.V2.1 however demonstrated all the properties desired for the actuation. It was possible to change the frequency, yet keeping the total mass flow in the actuator constant. The difference in the amplitude of the velocity signal, in that case, for different frequencies was very negligible. At the same time, it was also possible to vary the total mass flow in the actuator and yet keep the frequency constant. Thus, individual modulation of the frequency and the amplitude was possible. From the analysis, the operational range of the actuator is mapped as well. Moreover, the frequency of the actuator could be modulated just by tuning a very small mass flow in the oscillator, even for a very high mass flow through the amplifier. This provides a huge freedom of adjusting the frequency from the oscillator mass flow and the amplitude from the amplifier mass flow.

The model Z2.V2.2, a prototype of model Z2.V2.1, also demonstrated full functionality required for the actuation purpose. However, it had a different restricted operational range than the first model. So, CT images of the centerbody was made available, which showed blockage at the critical regions in the internal geometry. This model was also excluded for further investigation. Although, no reproducibility study could be performed on the model, an important aspect to acknowledge is that for a correct construction of the internal structure, the actuator works effectively. For future investigation, it is advised to use a precise method of manufacturing.

To further validate the results of the velocity measurement, visualization of the outlet flow was performed using a Schlieren imaging technique. To increase the density gradient, helium was used for the flow in the oscillator and the amplifier was supplied with air flow. The images distinctly showed switching between the

two outlets with clear pulses. The extraction of the frequency of the switching from the analysis of the images, showed ≈ 7 times the frequency for exclusively air flow through the actuator. The result is in the expected value considering the density of the helium, which is approximately seven times lighter than the air. Except for it, all other parameters remained constant. Although, the visualization of the actuator flow showed the desired switching characteristics, the visualization of the influence of the actuator on the PVC dynamics, especially at high mass flow through the actuator, would have been interesting. The whereabouts of the disruption of the flow field due to the high actuation mass flow could be validated. However, it was not possible to visualize the whole flow field of the combustion chamber employing the used Schlieren technique. It is therefore recommended for future investigations to use other measurement techniques like Particle Image Velocimetry (PIV).

With a very promising result, the model Z2.V2.1, was subjected to the actual actuation of the PVC in a generic swirl-stabilized combustor. The differential pressure measurement for three different cases were used for the evaluation, namely, one with only the PVC generated and without the actuation, the other with only the actuation and without the PVC generation and the final with the actuated PVC. Two PVC frequencies were taken for the actuation and were actuated with different frequencies $\approx \pm 10\%$ of the selected PVC frequency. The first azimuthal mode of the Fourier decomposition of the measured pressure signals from the four circumferentially arranged sensor positions were analysed for the reaction of the respective PVC. The analysis showed three distinct reactions: lock-in, damping and frequency shifting. The lock-in is characterized as the condition in which the PVC after actuation oscillates at the actuation frequency and with almost the same amplitude and phase. However, if the frequency is coupled but not the amplitude, then damping exists. Similarly, frequency shifting exists when the difference in the frequency of the actuation and that of the actuated PVC is higher. The actuation in the vicinity of the PVC frequency demonstrated the lock-in when excited with a sufficient amplitude. The actuation further away required increased amplitude for the lock-in. At insufficient amplitude, the PVC is shifted such that, for actuation frequency smaller than that of the PVC, a pulling effect towards the actuation frequency is observed and for higher frequency, a pushing effect away from the actuation is observed. In the transition between the shifting and the lock-in, damping is noticed. The lock-in region is wider for the actuation frequencies smaller than the PVC frequency. Nevertheless, a distinct V-form could be observed in the reaction diagram. The actuation demonstrated wider lock-in regions for the PVC frequency of 136.78 Hz than that of 119.23 Hz. The designed actuator demonstrated the possibility of the lock-in up to $\approx \pm 8\%$ of the PVC frequency.

The overall analysis of the actuator confirms the proof-of-concept and can be efficiently used for the actuation of the PVC in a swirl-stabilized combustor.

7 Conclusion

This work concentrated on the development of an actuator, which can effectively control a global hydrodynamic oscillation found in the swirl-stabilized combustor, the PVC. The requirement of the actuator included the generation of an external oscillation with a desired frequency and amplitude with the possibility of an independent modulation in a certain desired range. The flow through the actuator should be negligible compared to the main flow of the swirl-stabilized combustor. Furthermore, the actuator should be integrated into the centerbody with limited dimensions.

Accordingly, an actuator was designed and 2D simulations of the flow were performed and analysed, which demonstrated positive results. Following that, the actuator was integrated in the 3D centerbody and the working performance was validated by means of velocity measurement using a hot-wire measurement technique. The analysis of the velocity measurement demonstrated good switching characteristics. Thus, generating a desired oscillation for the actuation. The oscillation frequency could be kept constant for varying total mass flow. At the same time, the frequency could be varied for the constant total mass flow, thus independently adjusting the frequency and the amplitude of the oscillation. Moreover, the frequency could be adjusted just by tuning a small mass flow in the oscillator and the amplitude could be varied mainly through the amplifier mass flow. The actuator had a working region between ≈ 100 Hz and ≈ 190 Hz and the total mass flow range between ≈ 1.37 kg/h and ≈ 3.31 kg/h for a stable functioning. The mass flow in the actuator was ≈ 100 times lesser than the main flow in the combustor. To further validate the assuring results of the velocity measurement, visualization of the outlet flow was performed using Schlieren imaging technique. The images distinctly showed switching between the two outlets with clear pulses.

The actuator was finally subjected to the actual actuation of the PVC in a generic swirl-stabilized combustor. From the experimental investigation of the PVC dynamics to the actuation using the designed actuator it can be concluded that the PVC reacts with three distinct responses: lock-in, damping and frequency shifting. The actuation in the vicinity of the PVC frequency demonstrates the lock-in when excited with enough amplitude. The actuation further away requires increased amplitude for the lock-in. At insufficient amplitude, the PVC is shifted such that, for the actuation frequencies smaller than that of the PVC, a frequency pulling effect is observed and for higher frequency, a pushing effect is observed. In the transition between the shifting and the lock-in, damping is noticed. The lock-in region is wider for the actuation frequencies smaller than the PVC frequency. Nonetheless, a distinct V-form is observed in the reaction diagram, which summarizes the reaction of the PVC to different actuation with different frequency and amplitude. In addition to that,

7 Conclusion

an asymmetrical V-form distribution of the response of a hydrodynamic instability, as seen in the study of Li & Juniper [14] is further confirmed by this study. The actuation demonstrated wider lock-in regions for the PVC frequency of 136.78 Hz than that of 119.23 Hz. The designed actuator demonstrated the possibility of the lock-in up to $\approx \pm 8\%$ of the PVC frequency.

The overall design and analysis of the actuator confirms the proof-of-concept. The actuator was integrated into the centerbody. It was possible to generate external oscillation with a desired frequency and amplitude with the possibility of an independent modulation in a certain desired range. The flow through the actuator was still negligible compared to the main flow of the swirl-stabilized combustor. To conclude, the results of the flow simulations and experiments demonstrate the achievement of the design goals and using the actuator, designed in this work, the PVC can be efficiently actuated in a swirl-stabilized combustor.

Bibliography

- [1] A. K. Gupta, D. Lilley, and N. Syred, *Swirl flows*. Abacus Press, 1984.
- [2] N. Syred, “A review of oscillation mechanisms and the role of the precessing vortex core (pvc) in swirl combustion systems,” *Progress in Energy and Combustion Science*, vol. 32, pp. 93–161, 2006.
- [3] M. G. el Hak, A. Pollard, and J.-P. Bonnet, *Flow Control: Fundamentals and Practices*. Springer-Verlag Berlin Heidelberg, 1998.
- [4] K. Oberleithner, M. Stöhr, S. H. Im, C. M. Arndt, and A. M. Steinberg, “Formation and flame-induced suppression of the precessing vortex core in a swirl combustor: Experiments and linear stability analysis,” *Combustion and Flame*, vol. 162, pp. 3100–3114, 2015.
- [5] F. Gallaire, M. Ruith, E. Meiburg, J.-M. Chomaz, and P. Huerre, “Spiral vortex breakdown as a global mode,” *Journal of Fluid Mechanics*, vol. 549, p. 71, 2006.
- [6] K. Oberleithner, M. Sieber, C. N. Nayeri, C. O. Paschereit, C. Petz, H. Hege, B. R. Noack, and I. Wygnangsky, “Three-dimensional coherent structures in a swirling jet undergoing vortex breakdown: stability analysis and empirical mode construction,” *Journal of Fluid Mechanics*, vol. 679, pp. 383–414, 2011.
- [7] U. A. Qadri, D. Mistry, and M. P. Juniper, “Structural sensitivity of spiral vortex breakdown,” *Journal of Fluid Mechanics*, vol. 720, pp. 558–581, 2013.
- [8] L. Rukes, C. O. Paschereit, and K. Oberleithner, “An assessment of turbulence models for linear hydrodynamic stability analysis of strongly swirling jets,” *European Journal of Mechanics - B/Fluids*, 2016.
- [9] M. Stöhr, C. Arndt, and W. Meier, “Transient effects of fuel air mixing in a partially premixed turbulent swirl flame,” *Proceedings of the Combustion Institute*, vol. 35, pp. 3327–3335, 2015.
- [10] J. P. Moeck, J.-F. c. Bourgoquin, D. Durox, T. Schuller, and S. Candel, “Nonlinear interaction between a precessing vortex core and acoustic oscillations in a turbulent swirling flame,” *Combustion and Flame*, vol. 159, 2012.
- [11] S. Terhaar, B. Ćosić, C. Paschereit, and K. Oberleithner, “Suppression and excitation of the precessing vortex core by acoustic velocity fluctuations: An experimental and analytical study,” *Combustion and Flame*, vol. 172, pp. 234–251, 2016.

Bibliography

- [12] A. Ghani, T. Poinso, L. Gicquel, and J.-D. Müller, “Les study of transverse acoustic instabilities in a swirled kerosene/air combustion chamber,” *Flow, Turbulence and Combustion*, vol. 96, pp. 207–226, 2016.
- [13] C. Huygens, *The pendulum clock*. In *Horologium Oscillatorium*, Iowa State University Press, (translated in 1986), 1673.
- [14] L. K. B. Li and M. P. Juniper, “Phase trapping and slipping in a forced hydrodynamically self-excited jet,” *Journal of Fluid Mechanics*, vol. 735, p. R5, 2013.
- [15] G. H. Koopmann, “The vortex wakes of vibrating cylinders at low reynolds numbers,” *Journal of Fluid Mechanics*, vol. 28, p. 501, 1967.
- [16] P. K. Stansby, “The locking-on of vortex shedding due to the cross-stream vibration of circular cylinders in uniform and shear flows,” *Journal of Fluid Mechanics*, vol. 74, p. 641, 1976.
- [17] M. Provansal, C. Mathis, and L. Boyer, “Bénard-von kármán instability: transient and forced regimes,” *Journal of Fluid Mechanics*, vol. 182, p. 1, 1987.
- [18] D. J. Olinger, “Lock-in states in the dripping mode of the capillary jet,” *Experiments in Fluids*, vol. 15, pp. 155–158, 1993.
- [19] K. R. Sreenivasan, S. Raghu, and D. Kyle, “Absolute instability in variable density round jets,” *Experiments in Fluids*, vol. 7, pp. 309–317, 1989.
- [20] M. P. Hallberg and P. J. Strykowski, “Open-loop control of fully nonlinear self-excited oscillations,” *Physics of Fluids*, vol. 20, pp. 041–703, 2008.
- [21] D. R. Getsinger, C. Hendrickson, and A. R. Karagozian, “Shear layer instabilities in low-density transverse jets,” *Experiments in Fluids*, vol. 53, pp. 783–801, 2012.
- [22] L. K. B. Li and M. P. Juniper, “Lock-in and quasiperiodicity in a forced hydrodynamically self-excited jet,” *Journal of Fluid Mechanics*, vol. 726, pp. 624–655, 2013.
- [23] F. Lückoff, M. Sieber, C. Paschereit, and K. Oberleithner, “Characterization of different actuator designs for the control of the precessing vortex core in a swirl-stabilized combustor,” *ASME Turbo Expo 2017: Turbomachinery Technical Conference and Exposition, Band 4A: Combustion, Fuels and Emissions*, pp. 1–13, 2017.
- [24] F. Lückoff, M. Sieber, and K. Oberleithner, “Open-loop control of the precessing vortex core in a swirl-stabilized combustor: Impact on flame shape and flame stability,” in *Volume 4A: Combustion, Fuels, and Emissions*, American Society of Mechanical Engineers, June 2018.

- [25] D. Barkwoski, “Open-loop kontrolle des präzidierenden wirbelkerns (*pvc*) einer isothermen drallströmung in einer modellbrennkammer mit einem fluidischen oszillator,” Master’s thesis, Technische Universität Berlin, 2019.
- [26] Y. Huang and V. Yang, “Dynamics and stability of lean-premixed swirl-stabilized combustion,” *Progress in Energy and Combustion Science*, vol. 35, pp. 293–364, 2009.
- [27] Y. Huang and V. Yang, “Effect of swirl on combustion dynamics in a lean-premixed swirl-stabilized combustor,” *Proceedings of the Combustion Institute*, vol. 30, pp. 1775–1782, 2005.
- [28] V. Tangirala, R. H. Chen, and J. F. Driscoll, “Effect of heat release and swirl on the recirculation within swirl-stabilized flames,” *Combustion Science and Technology*, vol. 51, pp. 75–95, 1987.
- [29] P. Billant, J.-M. Chomaz, and P. Huerre, “Experimental study of vortex breakdown in swirling jets,” *Journal of Fluid Mechanics*, vol. 376, pp. 183–219, 1998.
- [30] D. Peckham and S. A. Atkinson, *Preliminary results of low speed wind tunnel tests on a gothic wing of aspect ratio 1.0*. Royal Aircraft Establishment, 1957.
- [31] N. Lambourne and D. Bryer, *The Bursting of Leading-edge Vortices: Some Observations and Discussion of the Phenomenon*. ARC-22775, H.M. Stationery Office and Aeronautical Research Council: Fluid Motion Sub-Committee, 1961.
- [32] T. Sarpkaya, “On stationary and travelling vortex breakdowns,” *Journal of Fluid Mechanics*, vol. 45, p. 545, 1971.
- [33] J. H. Faler and S. Leibovich, “Disrupted states of vortex flow and vortex breakdown,” *Physics of Fluids*, vol. 20, p. 1385, 1977.
- [34] K. Oberleithner, S. Terhaar, L. Rukes, and C. O. Paschereit, “Why nonuniform density suppresses the precessing vortex core,” *Journal of Engineering for Gas Turbines and Power*, vol. 135, p. 121506, 2013.
- [35] S. Terhaar, K. Oberleithner, and C. O. Paschereit, “Key parameters governing the precessing vortex core in reacting flows: An experimental and analytical study,” *Proceedings of the Combustion Institute*, vol. 35, pp. 3347–3354, 2015.
- [36] C. Petz, H.-C. Hege, K. Oberleithner, M. Sieber, C. N. Nayeri, C. O. Paschereit, I. Wygnanski, and B. R. Noack, “Global modes in a swirling jet undergoing vortex breakdown,” *Physics of Fluids*, vol. 23, pp. 091–102, 2011.
- [37] M. Freitag, M. Klein, M. Gregor, D. Geyer, C. Schneider, A. Dreizler, and J. Janicka, “Mixing analysis of a swirling recirculating flow using dns and experimental data,” *International Journal of Heat and Fluid Flow*, vol. 27, pp. 636–643, 2006.

Bibliography

- [38] J. Fröhlich, M. García-Villalba, and W. Rodi, “Scalar mixing and large-scale coherent structures in a turbulent swirling jet,” *Flow, Turbulence and Combustion*, vol. 80, pp. 47–59, 2008.
- [39] M. Stöhr, C. Arndt, and W. Meier, “Effects of damköhler number on vortex-flame interaction in a gas turbine model combustor,” *Proceedings of the Combustion Institute*, vol. 34, pp. 3107–3115, 2013.
- [40] A. Steinberg, I. Boxx, M. Stöhr, C. Carter, and W. Meier, “Flow-flame interactions causing acoustically coupled heat release fluctuations in a thermo-acoustically unstable gas turbine model combustor,” *Combustion and Flame*, vol. 157, pp. 2250–2266, 2010.
- [41] J. W. Joyce, *FLUIDICS - Basic Components and Applications*. U.S. Army Electronics Research and Development Command, Harry Diamond Laboratories, 1983.
- [42] C. J. Campagnuolo, C. Chase, and S. O. Rutstein, *Fluidic Oscillatory System Insensitive to Pressure and Temperature*. No. US1970-350, United States Patent, 1970.
- [43] S. Raghu, *Feedback-free fluidic oscillator and method*. No. US6,253,782, United States Patent, 2001.
- [44] V. Tesař, “"master and slave" fluidic amplifier cascade,” *EPJ Web of Conferences*, vol. 25, pp. 01093–, 04 2012.
- [45] R. Woszidlo, F. Ostermann, C. N. Nayeri, and C. O. Paschereit, “The time-resolved natural flow field of a fluidic oscillator,” *Experiments in Fluids*, vol. 56, p. 125, 2015.
- [46] M. Sieber, F. Ostermann, R. Woszidlo, K. Oberleithner, and C. O. Paschereit, “Lagrangian coherent structures in the flow field of a fluidic oscillator,” *Physical Review Fluids*, vol. 1, 2016.
- [47] J. Kirshner and S. Katz, *Design Theory of Fluidic Components*. Academic Press, 1975.
- [48] R. W. Warren, “Some parameters affecting the design of bistable fluid amplifiers,” *ASME*, pp. 75–82, 1962.
- [49] J. Kirshner, *Fluid amplifiers*. McGraw-Hill, 1966.
- [50] B. C. Bobusch, “Fluidic devices for realizing the shockless explosion combustion process,” Master’s thesis, Technische Universität Berlin, 2015.
- [51] R. Reilly and R. Moynihan, “Deflection and relative flow of three interacting jets,” in *Proceedings of the Fluid Amplification Symposium*, vol. 1, pp. 123–146, 1964.

- [52] K. Foster and G. Parker, *Fluidics: components and circuits*. Wiley-Interscience, 1970.
- [53] E. Chu, *Discrete and continuous fourier transforms analysis, applications and fast algorithms*. Chapman and Hall/CRC, 2008.
- [54] V. Tesař, C.-H. Hung, and W. B. Zimmerman, “No-moving-part hybrid-synthetic jet actuator,” *Sensors and Actuators A: Physical*, vol. 125, pp. 159–169, 2006.
- [55] G. S. Settles, *Schlieren and shadowgraph techniques: visualizing phenomena in transparent media*. Springer-Verlag Berlin Heidelberg NewYork, 1949.
- [56] L. K. Li and M. P. Juniper, “Lock-in and quasiperiodicity in hydrodynamically self-excited flames: Experiments and modelling,” *Proceedings of the Combustion Institute*, vol. 34, pp. 947–954, 2012.